

UC San Diego

UC San Diego Electronic Theses and Dissertations

Title

Develop high energy high power Li-ion battery cathode materials : a first principles computational study

Permalink

<https://escholarship.org/uc/item/04f5c2dr>

Authors

Xu, Bo

Xu, Bo

Publication Date

2012

Peer reviewed|Thesis/dissertation

UNIVERSITY OF CALIFORNIA, SAN DIEGO

Develop High Energy High Power Li-ion Battery Cathode Materials
A first principles computational study

A dissertation submitted in partial satisfaction of the requirements for the degree
Doctor of Philosophy

in

Materials Science and Engineering

By

Bo Xu

Committee in charge:

Professor Ying Shirley Meng, Chair
Professor Eric E. Fullerton
Professor Sungho Jin
Professor Katja Lindenberg
Professor John Weare

2012

©

Bo Xu, 2012

All rights reserved.

The Dissertation of Bo Xu is approved, and it is acceptable in quality and form for publication on microfilm and electronically:

Chair

University of California, San Diego

2012

TABLE OF CONTENTS

SIGNATURE PAGE.....	iii
TABLE OF CONTENTS	iv
LIST OF FIGURES	vi
LIST OF TABLES	ix
ACKNOWLEDGEMENTS	x
VITA.....	xiii
ABSTRACT.....	xiv
1 INTRODUCTION	1
1.1 Lithium Ion Batteries	1
1.2 Cathode materials of Li-ion batteries.....	3
1.3 Application of first-principles calculations on Li-ion batteries	5
1.4 Objectives and overview	6
2 FIRST PRINCIPLES METHOD AND ITS APPLICATION ON	
THERMODYNAMIC PROPERTIES OF INTERCALATION MATERIALS.....	11
2.1 Thermodynamics of intercalation materials.....	11
2.2 First principles energy calculations	12
2.2.1 <i>General energy approximation</i>	12
2.2.2 <i>Density-functional theory</i>	13
2.2.3 <i>Pseudopotential approximation</i>	14
2.2.4 <i>Periodic simplify</i>	15
3 CHARGE DISTRIBUTION AND FACTORS AFFECTING LI MOBILITY IN	
LiMn₂O₄ SPINEL.....	18
3.1 Introduction	18
3.2 Computational Methodology	20
3.3 Results and Discussion.....	22
3.3.1 <i>Ground state of Mn charge distribution in LiMn₂O₄ spinel</i>	22
3.3.2 <i>Simulated voltage and lattice parameters by GGA and GGA+U method</i>	23
3.3.3 <i>Electronic structure of Mn³⁺ and Mn⁴⁺</i>	26
3.3.4 <i>The effect of Mn charge distribution on Li diffusion activation barrier</i>	27
3.4 Conclusion.....	31

4 FIRST PRINCIPLES STUDY ON DOPED SPINEL $\text{LiM}_{0.5}\text{Mn}_{1.5}\text{O}_4$ (M =Ti, V, Cr, Fe, Co, Ni, Cu)	36
4.1 Introduction	36
4.2 Computational Methodology	38
4.3 Results and discussion.....	39
4.3.1 <i>The redox mechanism of $\text{LiM}_{0.5}\text{Mn}_{1.5}\text{O}_4$</i>	39
4.3.2 <i>Li diffusion barriers in $\text{Li}_x\text{M}_{1/2}\text{Mn}_{3/2}\text{O}_4$ (M= Ti, V, Cr, Fe, Co, Ni and Cu)</i> .	41
4.3.3 <i>The redox mechanism of $\text{LiCu}_{0.5}\text{Mn}_{1.5}\text{O}_4$</i>	42
4.4 Conclusion.....	44
5 IDENTIFYING SURFACE STRUCTURAL CHANGES IN LAYERED LI-EXCESS LAYERED NICKEL MANGANESE OXIDES IN HIGH VOLTAGE LITHIUM ION BATTERIES	51
5.1 Introduction	52
5.2 Methodologies.....	55
5.2.1 <i>Synthesis</i>	55
5.2.2 <i>Electrochemistry</i>	55
5.2.3 <i>X-ray diffraction</i>	57
5.2.4 <i>α-STEM/EELS</i>	57
5.3 Results	58
5.3.1 <i>Electrochemical properties</i>	58
5.3.2 <i>XRD</i>	60
5.3.3 <i>STEM</i>	61
5.3.4 <i>EELS</i>	63
5.3.5 <i>First-principles calculations</i>	64
5.4 General discussion	67
5.5 Conclusion.....	72
6 FIRST PRINCIPLES STUDY OF THE ROLES OF OXYGEN VACANCY ON CATION MIGRATION IN LITHIUM EXCESS NICKEL MANGANESE OXIDES	84
6.1 Formation energy of oxygen vacancy in $\text{Li}_x\text{Ni}_{1/4}\text{Mn}_{7/12}\text{O}_2$ bulk	84
6.2 Ni diffusion in $\text{Li}_x\text{Ni}_{1/4}\text{Mn}_{7/12}\text{O}_2$ bulk.....	86
6.3 Conclusion.....	89
7 SUMMARY AND FUTURE WORK.....	94
7.1 Summary	94
7.2 Future work	96
7.2.1 <i>Computational designing of Li-rich doped spinel $\text{Li}_2\text{M}_2\text{O}_4$</i>	96
7.2.2 <i>Surface coating of Li-excess layered compound $\text{Li}[\text{Ni}_x\text{Li}_{1/3-2x/3}\text{Mn}_{2/3-x/3}]\text{O}_2$</i> ..	96
REFERENCE.....	98

LIST OF FIGURES

Figure 1.1 Working principles of LIB (charging).....	9
Figure 1.2 Theoretical and practical gravimetric energy densities of different cathode materials	9
Figure 1.3 Crystal structure of layered LiMO_2 (Blue: transition metal ions; Red: Li ions)	10
Figure 1.4 Crystal structure of spinel LiM_2O_4 (Blue: transition metal ions; Red: Li ions)	10
Figure 3.1 Calculated total energy and ewald energy of LiMn_2O_4 with different Mn charge distribution.....	32
Figure 3.2 Local Mn charge arrangements in LiMn_2O_4 ground state (green: Mn^{4+} ; orange: Mn^{3+}).....	32
Figure 3.3 (a) Voltage calculated by GGA and GGA+U methods; (b) Calculated and experimentally measured lattice parameters of the $\text{Li}_x\text{Mn}_2\text{O}_4$ cubic unit cell as a function of Li concentration.....	33
Figure 3.4 Mn 3d electron Density of State (DOS) plots using GGA+U and GGA (insert) methods	34
Figure 3.5 Three-dimensional lithium diffusion paths in LiMn_2O_4	34
Figure 3.6 (a) Local environment dependent Li diffusion activation barriers in $\text{Li}_7\text{Mn}_{16}\text{O}_{32}$; (b) Active Li $16c$ site octahedral volumes; (c) Distances between the mobile Li ion and surrounding Mn ions; (d) Mn-O bondlengths of $\text{Mn}^{3+}/\text{Mn}^{4+}$ in configuration e.	35
Figure 4.1 Calculated and experimental two-step voltages of $\text{LiM}_{0.5}\text{Mn}_{1.5}\text{O}_4$	46
Figure 4.2 Calculated electronic density of states (DOS) of M ions in $\text{LiM}_{0.5}\text{Mn}_{1.5}\text{O}_4$ (M=Ti, V, Cr, Fe, Co, Ni).....	47
Figure 4.3 Local environments of transition metal ion rings (a) Three M ions in the ring (b) One M ion in the ring	48
Figure 4.4 Li diffusion barriers in $\text{LiM}_{0.5}\text{Mn}_{1.5}\text{O}_4$ (M= Cr, Fe, Co, Ni, Cu, Mn) calculated	48
Figure 4.5 Calculated DOS of Cu in $\text{Li}_x\text{Cu}_{1/2}\text{Mn}_{3/2}\text{O}_4$ ((a) $x=1$ (b) $x=1/2$ (c) $x=0$).....	49

Figure 4.6 Electrochemical performances of $\text{LiNi}_{0.25}\text{Cu}_{0.25}\text{Mn}_{1.5}\text{O}_4$	50
Figure 5.1 (a) Electrochemical profile of $\text{Li}[\text{Ni}_x\text{Li}_{1/3-2x/3}\text{Mn}_{2/3-x/3}]\text{O}_2$ ($x=1/5$) with a C/50 rate. A voltage window of 4.8 – 2.0 V was used (b) Capacity versus electrochemical cycle of $\text{Li}[\text{Ni}_{1/5}\text{Li}_{1/5}\text{Mn}_{3/5}]\text{O}_2$. The first 5 cycles correspond to a C/50 rate and cycles 6-1 correspond to a C/20 rate.....	73
Figure 5.2 Experimental observations (marked by X) of electrochemical impedance spectroscopy (EIS) of $\text{Li}[\text{Ni}_{1/5}\text{Li}_{1/5}\text{Mn}_{3/5}]\text{O}_2$ during the first electrochemical charging cycle at different states of charge(SOC) The equivalent circuit model in the inset was used to fit the experimental model and plotted as a line at different SOC.	74
Figure 5.3 High resolution synchrotron X-ray diffraction pattern of discharged $\text{Li}[\text{Ni}_{1/5}\text{Li}_{1/5}\text{Mn}_{3/5}]\text{O}_2$ following 10 electrochemical cycles. Rietveld Refinement of 3a) one $R\bar{3}m$ phase and 3b) two $R\bar{3}m$ phases. The black crosses represent the observed pattern, the red line corresponds to the calculated diffraction pattern and the blue is the difference pattern. The teal lines correspond to peak positions from the $R\bar{3}m$ space group. In this and subsequent figures, the 2θ values are converted to those corresponding to a Cu $K\alpha$ wavelength ($\lambda=1.54 \text{ \AA}$)	75
Figure 5.4 High resolution S/TEM images of the bulk and surface of pristine $\text{Li}[\text{Ni}_{1/5}\text{Li}_{1/5}\text{Mn}_{3/5}]\text{O}_2$ at low magnification (a) and high magnification (b) taken along $[100]$. The insert in (b) is a schematic representation of the Li ions (red) and transition metal ions (yellow) showing the cation ordering and stacking along the c_{hex} axis.....	76
Figure 5.5 High resolution S/TEM image (a) and corresponding HAADF image (b) of the bulk and surface regions of electrochemically cycled $\text{Li}[\text{Ni}_{1/5}\text{Li}_{1/5}\text{Mn}_{3/5}]\text{O}_2$ taken along the $[110]$ $[1010]$ zone axis.....	76
Figure 5.6 Representative EELS spectra of the (a) O K-edge and (a & b) Mn L-edge from the surface and bulk of the pristine and electrochemically cycled $\text{Li}[\text{Ni}_{1/5}\text{Li}_{1/5}\text{Mn}_{3/5}]\text{O}_2$ material.....	77
Figure 5.7 Comparison of Li-K edges from the surface and bulk in the cycled material. Obvious Li signal drop was observed on the spectrum from the surface area compared to that from bulk, although Li-K edge overlaps TM-M edges. Dotted lines mark the main peak position of Li-K and TM-M edges.	77
Figure 5.8 a and b The cation in-plane ordering of different models of $\text{Li}[\text{Ni}_{1/4}\text{Li}_{1/6}\text{Mn}_{7/12}]\text{O}_2$ (Red: Li; Green: Mn; Blue: Ni) Figure 5.8c Calculated voltage and formation enthalpy of $\text{Li}_{x/14}\text{Ni}_{1/4}\text{Mn}_{7/12}\text{O}_2$ ($8 < x < 14$) versus lithium concentration.....	78
Figure 5.9 The defect-spinel model of $\text{Li}[\text{Ni}_{1/4}\text{Li}_{1/6}\text{Mn}_{7/12}]\text{O}_2$ and $\text{Li}[\text{Li}_{1/3}\text{Ni}_{1/2}\text{Mn}_{7/6}]\text{O}_4$	79

Figure 5.10 Calculated magnetization of Ni and Mn ions versus lithium concentration .	79
Figure 5.11 The calculated spin density (difference between spin-up and spin-down) of part of the TM layer at $\text{Li}_{x/14}\text{Ni}_{1/4}\text{Mn}_{7/12}\text{O}_2$ (b) $x=14$ (c) $x=8$ (d) $x=0$	80
Figure 5.12 Sketch of Li-Li dumbbell formation (Red:Li; Green:Mn; Blue:Ni; Yellow: Vacancy)	81
Figure 6.1 Atom configurations of $\text{Li}[\text{Li}_{1/6}\text{Ni}_{1/4}\text{Mn}_{7/12}]\text{O}_2$ (Red: Li; Green: Mn; Blue: Ni; Orange: O).....	90
Figure 6.2 Oxygen vacancy formation energy vs. Li concentration.....	90
Figure 6.3 Demonstration of transition state theory and Ni diffusion mechanism.....	91
Figure 6.4 Oxygen vacancy formation energy of initial states for Ni migration	91
Figure 6.5 Ni diffusion barriers at Li concentration 25/28	92
Figure 6.6 Ni diffusion barriers at Li concentration 20/28	92
Figure 6.7 Ni diffusion barriers at Li concentration 15/28	93

LIST OF TABLES

Table 3.1 Atomic positions of new Mn charge distribution ground state in LiMn_2O_4	22
Table 3.2 Mn valence configurations in Mn-rings surrounding the diffusing Li^+ in the activated site.....	28
Table 4.1 Effective U values used for the first row transition metal ions in $\text{LiM}_{0.5}\text{Mn}_{1.5}\text{O}_4$	38
Table 4.2 Calculated 3d electron configurations, valence states and of M ions, and the percentage of amount of Mn^{3+} ions in $\text{LiM}_{0.5}\text{Mn}_{1.4}\text{O}_4$	39
Table 4.3 Lattice parameters and corresponding c/a , c/b ratio of $\text{LiM}_{0.5}\text{Mn}_{1.5}\text{O}_4$	40
Table 5.1 Fitting parameters for the equivalent circuit model represented in Fig. 2 applied to the electrochemical impedance (EIS) curves recorded between 3.80 V and 4.60 V	82
Table 5.2 Two phase Rietveld refinement results for discharged $\text{Li}[\text{Ni}_{1/5}\text{Li}_{1/5}\text{Mn}_{3/5}]\text{O}_2$ following 10 electrochemical cycles using two $R\bar{3}m$ R3m phases.....	82
Table 5.3 Two phase Rietveld refinement results for discharged $\text{Li}[\text{Ni}_{1/5}\text{Li}_{1/5}\text{Mn}_{3/5}]\text{O}_2$ following 10 electrochemical cycles including one phase with Li on the $(1/3, 2/3, z)$ tetrahedral site	83

ACKNOWLEDGEMENTS

First of all, I would like to thank my thesis advisor Dr. Ying Shirley Meng for providing me all the opportunities for completing this work. Her knowledge, care, and inspiration for this work pushed me to expand my knowledge and research potential. I would like to express the deepest gratitude to my other committee members: Dr. Eric Fullerton, Dr. John H. Weare, Dr. Katja Lindenberg, Dr. Sungho Jin and former committee member Dr. Andrew Kummel for their time and guidance.

I would like to thank my experimental collaborators and co-authors, Dr. Christopher R. Fell and Dr. Ming-Che Yang, with whom I had many useful and stimulating discussions. I would like to thank my co-authors Danna Qian, Ziyang Wang, Hyung-Man Cho, and collaborators Dr. Kyler Carroll, Michael Verde in LESC group as well for all the collaboration works. I'm also grateful to all my groupmates in LESC group who have helped and inspired me in many ways.

I would like to express special thanks to Dr. Stefano Curtarolo and Dr. Anton Van der Ven for sharing helpful codes aconvasp and CASM and the valuable suggestions they provide to my work. I would also like to thank Dr. Elena M. Arroyo, Dr. Jishnu Bhattacharya and Dr. Yoyo Hinuma for everything I learnt from them when we were working together.

Chapter 1, in part, is a reprint of the material "Recent Progress in Cathode Materials Research for Advanced Lithium Ion Batteries", as it appears in Materials Science and Engineering R, 73(5-6), 51-65, 2012. Bo Xu, Danna Qian, Ziyang Wang, Ying Shirley Meng, 2012. The dissertation author was the primary investigator and

author of this paper.

Chapter 3, in part, is a reprint of the material "Factors affecting Li mobility in spinel LiMn_2O_4 - A first-principles study by GGA and GGA+U methods", as it appears in Journal of Power Sources, 195 (15), 2010. Bo Xu, Ying S. Meng, 2010. The dissertation author was the primary investigator and author of this paper.

Chapter 4, in part, is a reprint of the material "Electronic, Structural and Electrochemical Properties of $\text{LiNi}_x\text{Cu}_y\text{Mn}_{2-x-y}\text{O}_4$ ($0 < x < 0.5$, $0 < y < 0.5$) High-Voltage Spinel Materials", as it appears in Chemistry of Materials, 23 (11), 2011. Ming-Che Yang, B. Xu, J. Cheng, C. Pan, B. Hwang and Ying S. Meng, 2011. The dissertation author was the primary investigator and author of this paper.

Chapter 5, in full, is a reprint of the material "Identifying Surface Structural Changes in Layered Li-excess Nickel Manganese Oxides in High Voltage Lithium Ion Batteries: A Joint Experimental and Theoretical Study", as it appears in Energy & Environmental Science, 4(6), 2011. Bo Xu, C. R. Fell, M. Chi, Ying S. Meng, 2011. The dissertation author was the primary investigator and author of this paper.

Chapter 6, in full, is currently being prepared for submission for publication of the material. Bo Xu, Ying S. Meng, 2012. The dissertation author was the primary investigator and author of this paper.

I would like to acknowledge the financial support from University of California, San Diego startup funding, and from the Northeastern Center for Chemical Energy Storage (NECCES), an Energy Frontier Research Center funded by the U.S. Department of Energy. I would like to acknowledge Extreme Science and Engineering Discovery Environment, San Deigo Supercomputer Center and Texas advanced Computer Center

for providing computation resources.

For the last but not least, my deepest gratitude goes to my parents Yuming Xu and Xiang Zheng. Their love, patience and unselfish support make everything possible.

VITA

2007	B. S.	Fudan University, People's Republic of China
2009	M. S.	University of Florida, USA
2012	Ph.D	University of California, San Diego, USA

PUBLICATIONS

1. **Bo Xu**, Ying S. Meng, "Factors affecting Li mobility in spinel LiMn_2O_4 - A first-principles study by GGA and GGA+U methods", *Journal of Power Sources*, 195 (15), 2010.
2. **Bo Xu**, C. R. Fell, M. Chi, Ying S. Meng, "Identifying Surface Structural Changes in Layered Li-excess Nickel Manganese Oxides in High Voltage Lithium Ion Batteries: A Joint Experimental and Theoretical Study", *Energy & Environmental Science*, 4(6), 2011
3. **Bo Xu**, D. Qian, Z. Wang, Y. S. Meng, "Recent Progress in Cathode Materials Research for Advanced Lithium Ion Batteries", *Materials Science and Engineering R*, 2012
4. Ming-Che Yang, **B. Xu**, J. Cheng, C. Pan, B. Hwang and Ying S. Meng, "Electronic, Structural and Electrochemical Properties of $\text{LiNi}_x\text{Cu}_y\text{Mn}_{2-x-y}\text{O}_4$ ($0 < x < 0.5$, $0 < y < 0.5$) High-Voltage Spinel Materials", *Chemistry of Materials*, 23 (11), 2011
5. Ming-Che Yang, Y. Lee, **B. Xu**, K. Powers, Ying S. Meng, "TiO₂ flakes as anode materials for Li-ion-batteries", *Journal of Power Source*, 2012, 207, 166-172
6. Danna Qian, **B. Xu**, H.-M. Cho, T. Hatsukade, K. J. Carroll, Ying S. Meng, "Lithium Lanthanum Titanium Oxides: A Fast Ionic Conductive Coating for Lithium-Ion Battery Cathodes", *Chemistry of Materials*, 2012

FIELDS OF STUDY

Major Field: Materials Science and Engineering

ABSTRACT OF THE DISSERTATION

Develop High Energy High Power Li-ion Battery Cathode Materials

A first principles computational study

By

Bo Xu

Doctor of Philosophy in Materials Science and Engineering

University of California, San Diego, 2012

Professor Ying Shirley Meng, Chair

Lithium ion batteries (LIB) are regarded as one of the near-term solutions to the gloable energy shortage and have drawn increasing attentions. To be implemented in the large-scale high-power system, performance requirements are raised especially from the aspects of energy/power density, cycling life and safety issues, therefore further LIB material and system developments are necessary. Among Li-intercalation compounds, high voltage spinel compound $\text{LiM}_{0.5}\text{Mn}_{1.5}\text{O}_4$ and high capacity layered lithium-excess oxide compounds $\text{Li}[\text{Ni}_x\text{Li}_{1/3-2x/3}\text{Mn}_{2/3-x/3}]\text{O}_2$ are of great interests. On the other hand, the

poor rate capability and cycling performances are preventing these materials from commercialization.

In this dissertation, systematic studies are performed on these two types of candidate materials using first principles method. The dissertation can be divided into two parts. In the first part, cation charge ordering in LiMn_2O_4 and its effects on Li diffusion in LiMn_2O_4 spinel are investigated. The conclusions are used as the criteria to pre-screen the dopant M in $\text{LiM}_{0.5}\text{Mn}_{1.5}\text{O}_4$ by computation. Cu is found to be able to reduce the Li diffusion barriers and a new type of bi-doped spinel $\text{LiNi}_x\text{Cu}_y\text{Mn}_{2-x-y}\text{O}_4$ ($0 < x < 0.5$, $0 < y < 0.5$) is proposed to have enhanced rate capability, which is confirmed later from experiments.

In the second part, first principles method combined with other advanced characterization techniques is used to understand the intercalation mechanism of the layered lithium-excess transition metal oxide $\text{Li}[\text{Li}_{1/6}\text{Ni}_{1/4}\text{Mn}_{7/12}]\text{O}_2$ and related surface structural change. The phase stabilities of $\text{Li}[\text{Li}_{1/6}\text{Ni}_{1/4}\text{Mn}_{7/12}]\text{O}_2$ at different Li concentrations are investigated and it is shown that a defect spinel phase may generate during the de-intercalation process. The phase transformation is accompanied with the migration of transition metal ions. Computational studies on Ni diffusion mechanism shows that oxygen vacancies are playing an important role in assisting this migration process. These finds lead to an increased understanding of the lithium transport mechanisms in the lithium-excess series of compounds, and provide new insights in optimizing their rate performances.

1 INTRODUCTION

With the worldwide energy shortage being one of the mounting problems in 21st century, efforts have been made to replace the non-renewable fossil fuels by other green energy sources, such as solar, wind, hydroelectric power, etc. Different from the conventional fossil fuels, most of these green energy sources suffer from their uncontrollable and intermittent nature, therefore the difficulty in energy storage and regulation results in larger cost. This brings in enormous amount of research interests in material developments for energy storage. The LIB system is regarded as one of the near-term solutions because of its high energy density and relatively simple reaction mechanism. Current LIB technology is well developed for the portable electronic devices and has been widely used in the past twenty years. However, to be implemented in the large-scale high-power system such as the plug-in hybrid electric vehicle (PHEV) or plug-in electric vehicle (PEV), performance requirements are raised especially from the aspects of energy/power density, cycling life and safety issues, therefore further LIB material and system developments are necessary.

1.1 Lithium Ion Batteries

A lithium ion battery can work as the energy storage device by converting electric energy into electrochemical energy. The basic working principles of LIB are shown in Figure 1. There are three key components in a LIB system: cathode, anode and electrolyte. For today's commercialized LIB system, both cathode and anode materials are intercalation materials. The transition metal oxides in cathode (graphite in anode) consist of a largely unchangeable host with specific sites for Li ions to be intercalated in.

All Li ions are in the cathode sides initially and the battery system is assembled in “discharged” status. While charging, Li ions are extracted from the cathode host, solvate into and move through the non-aqueous electrolyte, and intercalate into the anode host. Meanwhile, electrons also move from cathode to anode through the outside current collectors forming an electric circuit. The chemical potential of Li is much higher in the anode than in the cathode, thus the electric energy is stored in the form of (electro)chemical energy. Such process is reversed when the battery is discharging where the electrochemical energy is released in the form of electric energy. The cathode region and anode region are separated by the separator, a micro-porous membrane that allows the electrolyte to penetrate and prevent shorting between the two electrodes. The electrolyte should be ionically conducting and electronically insulating in principle, however the actual properties of the electrolyte is much more complicated. During the first cycle, a so-called solid-electrolyte-interphase (SEI) layer will be formed on the surface of electrodes due to the decomposition of organic electrolyte at extreme voltage range (typically $<1.2\text{V}$ or $>4.6\text{V}$). In current LIB technology, the cell voltage and capacities are mainly determined by the cathode material that is also the limiting factor for Li transportation rate. The developments of cathode materials therefore become extremely crucial and receive much attention in recent decade.

Since 1980 when the LiCoO_2 was demonstrated firstly as a possible cathode material for rechargeable lithium battery[1], the transition metal intercalation oxides have caught the major research interests as the LIB cathodes[2-8]. Categorized by structure, the conventional cathode materials include layered compounds LiMO_2 ($\text{M} = \text{Co}, \text{Ni}, \text{Mn}$ etc.), spinel compounds LiM_2O_4 ($\text{M} = \text{Mn}$ etc.), and olivine compounds LiMPO_4 ($\text{M} = \text{Fe}$,

Mn, Ni, Co etc.). Most of the researches are performed on these materials and their derivatives. New structure intercalation materials such as silicates, borates and tavorite are also gaining increasing attentions in recent years. During the materials optimization and development, following designing criterions are often considered: 1) Energy density; 2) Rate capability; 3) Cycling performance; 4) Safety; 5) Cost. The energy density is determined by the material's reversible capacity and operating voltage, which are mostly determined by the material intrinsic chemistry such as the effective redox couples and maximum lithium concentration in active materials. For rate capability and cycling performances, electronic and ionic mobilities are key determining factors, though particle morphologies are also important factors due to the anisotropic nature of the structures and are even playing a crucial role in some cases. Figure 2 compared the gravimetric energy densities of different cathode materials that are currently under investigations. While some materials such as LiFeBO_3 and LiFeSO_4F are already approaching their theoretical energy densities, for other materials including conventional layered and spinel compounds, significant gaps are still present between their theoretical and practical energy densities. These materials with promising theoretical properties have high potentials as the candidates of future generation LIB cathode, however, their rate capacity and cycling performances still need much improvement to before they can be commercialized.

1.2 Cathode materials of Li-ion batteries

Conventional cathode materials include layered compounds LiMO_2 , spinel compounds LiM_2O_4 , and olivine compounds LiMPO_4 . The layered and spinel compounds

are generally introduced below, as the main researches of this work are conducted to understand and improve the performances of these two types of materials.

The ideal structure of layered compound LiMO_2 is demonstrated in Figure 3. The oxygen anions (omitted for clarity in the figures) form a close-packed *fcc* lattice with cations located in the 6-coordinated octahedral crystal site. The MO_2 slabs and Li layers are stacked alternatively. Although the conventional layered oxide LiCoO_2 has been commercialized as the LIB cathode for twenty years, it can only deliver about 140mAh/g capacity which is half of its theoretical capacity. Such limitation can be attributed to the intrinsic structural instability of the material when more than half of the Li ions are extracted. On the other hand, the presence of toxic and expensive Co ions in LiCoO_2 has introduced the environmental problem as well as raised the cost of the LIB.

For improvement, Co ions in LiCoO_2 can be substituted by other transition metal ions such as Ni and Mn. The new substitutions can reduce the cost of the materials and make the materials more environmentally friendly by eliminating the use of Co ions which are expensive and toxic. One of the most promising candidates is so-called Li-excess nickel manganese layer oxides $\text{Li}[\text{Ni}_x\text{Li}_{1/3-2x/3}\text{Mn}_{2/3-x/3}]\text{O}_2$. The compounds were first reported in 2001[9] and can be expressed as a composite of two end members of $\text{Li}[\text{Li}_{1/3}\text{Mn}_{2/3}]\text{O}_2$ and $\text{LiNi}_{1/2}\text{Mn}_{1/2}\text{O}_2$. A reversible capacity as high as 250mAh/g can be obtained routinely[10].

The structure of LiM_2O_4 spinel is shown in Figure 4. The oxygen framework of LiM_2O_4 is the same as that of LiMO_2 layered structure. M cations still occupy the octahedral site but 1/4 of them are located in the Li layer, leaving 1/4 of the sites in transition metal layer vacant. Li ions occupy the tetrahedral sites in Li layer that share

faces with the empty octahedral sites in the transition metal layer. The structure is based on a three-dimensional MO_2 host and the vacancies in transition metal layer ensure the three-dimensional Li diffusion pathways. The spinel LiMn_2O_4 was proposed as the cathode of the lithium ion battery by Thackeray et al. in 1983[11-13], but the material was found to encounter severe capacity fading problem.

Substituting Mn with other metal ions has been used as an important approach to improve cycling performance of spinel materials. Multiple dopants including inactive ions such as Mg, Al, Zn etc. [14-16], first row transition metal ions such as Ti, Cr, Fe, Co, Ni, Cu, etc. [17-21] and rare earth metal ions such as Nd, La, etc. [22-24] have been investigated and $\text{LiNi}_{0.5}\text{Mn}_{1.5}\text{O}_4$ shows the best overall electrochemical performances among the above. The voltage of these materials can be raised to more than 4.7 V therefore the energy densities are highly improved. The rate capability, on the other hand, are not found to be improved significantly.

1.3 Application of first-principles calculations on Li-ion batteries

Due to the complexity and long time periods of experimental synthesis and characterization, computer based simulation has been developed to further optimize and design the cathode materials in a more efficient way. The concept of “virtual laboratory” has been brought into the scientific field. Comparing to laboratory experiments, it is much easier to control different experimental conditions. Since computer-based simulations do not require complex synthesis procedures or long-time characterizations, therefore is much efficient for materials design and development. Quantum mechanics and statistical physics are combined to investigate the thermodynamic properties of

cathode materials. References have been published to prove that with the use of first-principles calculations, the phase diagram of complicated Li-intercalation materials can be determined and the mechanisms of Li diffusion in layered materials have been well studied[25-29]. The details of the first principles methods and its applications to the thermodynamics of intercalation materials will be introduced in chapter 2.

1.4 Objectives and overview

As described in previous sections, as the potential cathodes candidates, doped spinel oxides and Li-excess layered oxides have high theoretical capacities, but also have many problems preventing them from commercialization. For doped spinel oxides, the rate capability of synthesized $\text{LiNi}_{0.5}\text{Mn}_{1.5}\text{O}_4$ particles are relatively slow due to the reduced conductivity comparing to LiMn_2O_4 . Doping multiple cations into the compounds was tried in a lot of previous experimental researches, but no consistent conclusion can be obtained due to the lack of a systematic study. For Li-excess layered compounds, a large amount of irreversible capacity exists after the first charge-discharge cycle, and the rate capability of this material also needs optimization[30-32]. The most promising approaches for improving these properties involve surface coating of the cathode surface with other oxides or fluorides[33, 34], but the exact mechanisms for the surface coating are still under much debate.

The objective of this research project is to improve and develop high energy high power Li-ion battery cathode materials using first principles computational methods. The project can be divided into two parts:

Part 1: Study factors affecting Li diffusion in spinel compounds and develop new spinel materials with high voltage high rate

- 1) Use LiMn_2O_4 as the basic model to establish a reliable computation method to investigate the materials thermal stability, electronic structure and Li diffusion in spinel structure.
- 2) Build up single-doped $\text{LiM}_{0.5}\text{Mn}_{1.5}\text{O}_4$ spinel model and investigate the factors affecting Li mobility. M is chosen from the first row transition metal ions including Ti, V, Cr, Fe, Co, Ni, Cu. For each selected doped materials, the effect of charge configuration of local environments are investigated.
- 3) Based on the results obtained from step 2, new bi-doping spinel $\text{LiM}_x\text{M}_y\text{Mn}_{2-x-y}\text{O}_4$ is designed, which should have optimized Li mobility; therefore, may have better rate capability. With the computational guidance, collaborations are done with laboratory experiments to synthesis and characterize these new spinel materials.

Part 2: Study structural change and cation rearrangements during lithium deintercalation in $\text{Li}[\text{Ni}_x\text{Li}_{1/3-2x/3}\text{Mn}_{2/3-x/3}]\text{O}_2$

- 1) Calculate the phase stability of $\text{Li}_{x/12}\text{Ni}_{1/4}\text{Mn}_{7/12}\text{O}_2$ ($x > 8$) and simulate the related voltage profile.
- 2) Investigate the oxygen release and cation rearrangements at $\text{Li}_{x/12}\text{Ni}_{1/4}\text{Mn}_{7/12}\text{O}_2$ ($x \sim 8$).
 - i) Explore possible mechanism of oxygen vacancy formation and calculate related formation energy.
 - ii) Explore the cation (Li, Ni and Mn) migration mechanism with the assistance of oxygen vacancies.

3) Based on the results obtained from step 2, a possible mechanism of the surface structural change of $\text{Li}_{x/12}\text{Ni}_{1/4}\text{Mn}_{7/12}\text{O}_2$ is proposed as the explanation to the phenomenon observed by laboratory experiments.

Chapter 1, in part, is a reprint of the material "Recent Progress in Cathode Materials Research for Advanced Lithium Ion Batteries", as it appears in *Materials Science and Engineering R*, 73(5-6), 51-65, 2012. Bo Xu, Danna Qian, Ziyang Wang, Ying Shirley Meng, 2012. The dissertation author was the primary investigator and author of this paper.

Figures:

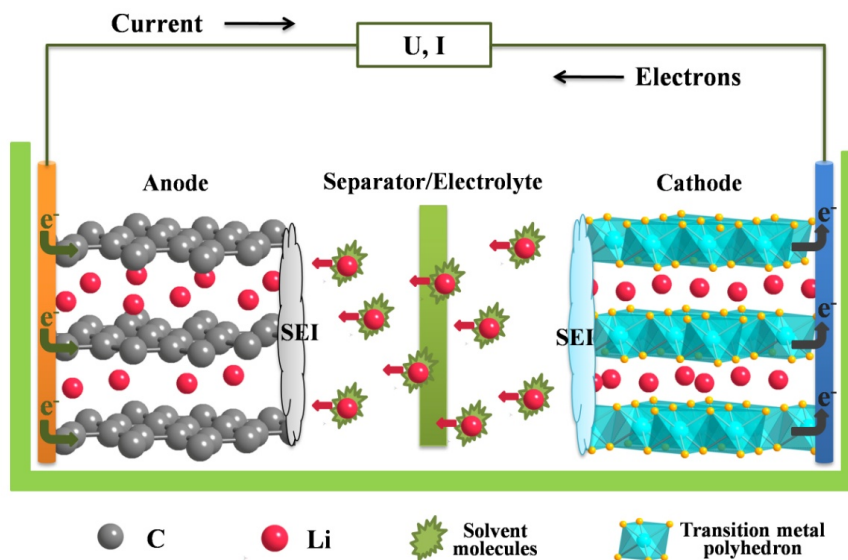


Figure 1.1 Working principles of LIB (charging)

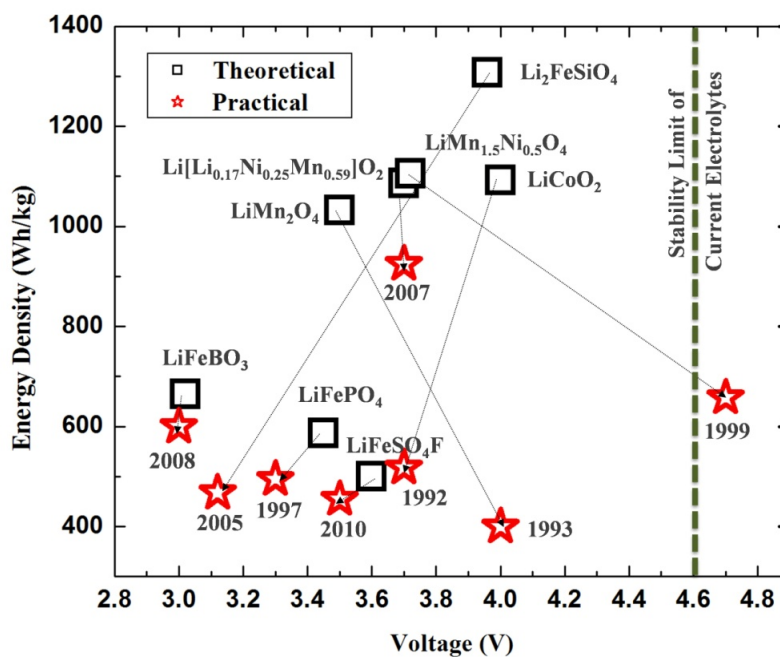


Figure 1.2 Theoretical and practical gravimetric energy densities of different cathode materials

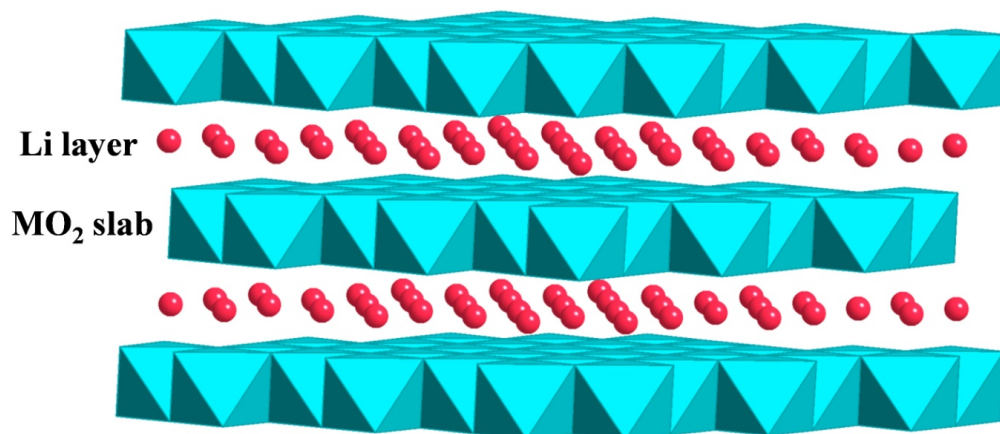


Figure 1.3 Crystal structure of layered LiMO_2 (Blue: transition metal ions; Red: Li ions)

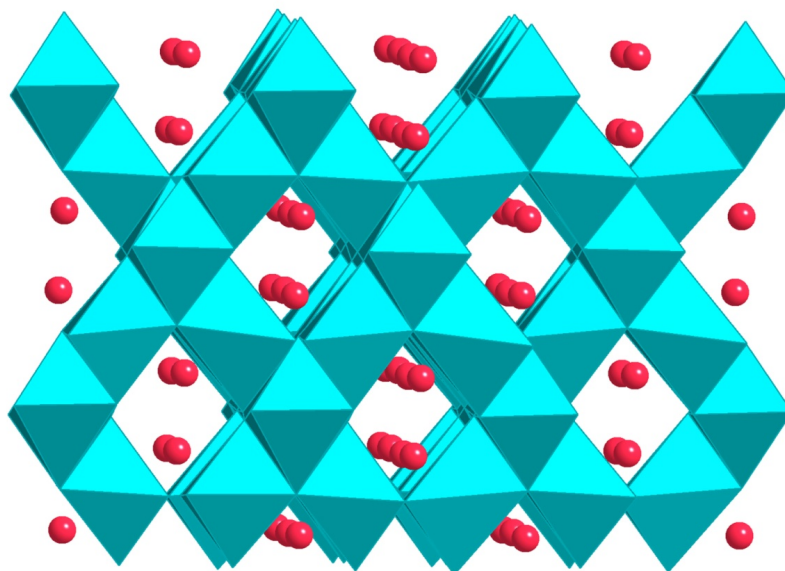


Figure 1.4 Crystal structure of spinel LiM_2O_4 (Blue: transition metal ions; Red: Li ions)

2 FIRST PRINCIPLES METHOD AND ITS APPLICATION ON THERMODYNAMIC PROPERTIES OF INTERCALATION MATERIALS

2.1 Thermodynamics of intercalation materials

The formula of the Lithium intercalation materials could be written as LiM , where M is the host structure and Li is the mobile ions. While in the charging/discharging process, the following reaction happens at the cathode sides:



The average voltage is therefore $V = \frac{\Delta G}{xze}$ where ΔG is the Gibbs free energy for the reaction, z is the valence of Li and e is the charge of the electron.^[35] Usually, the host structure M does not change during the charging/discharging process, therefore its chemical potential does not change. The electrochemical energy comes from the change of chemical potential of Li ions. The voltage therefore could be derived from the Nernst equation^[36]

$$V(x) = -\frac{(\mu_{Li}^{cathode} - \mu_{Li}^{anode})}{ze} \quad 2-2$$

It is common to use metal Li as the anode materials, therefore μ_{Li}^{anode} is usually constant. From the knowledge of classical thermodynamics, the derivative of gibbs free energy can be written as:

$$dG = Vdp - SdT + \sum \mu_i dN_i \quad 2-3$$

Under the condition of constant pressure and temperature, the host structure does not change, therefore the chemical potential of Li could be written as $\mu_{Li} = \left(\frac{\partial G}{\partial N_{Li}} \right)_{T,P,N_{host}}$, where N_{Li} is the number of lithium ions^[36]. As the intercalation materials are usually treated as the open system, from experiments, the open circuit voltage V could be controlled and measured therefore the independent intensive variables of the system should be temperature T , pressure P , and chemical potential μ . To investigate the phase stability at different temperature or pressure, the characteristic potential should be grand canonical free energy rather than the gibbs free energy. A Legendre transform is necessary that the grand canonical free energy

$$\Omega^{host} = G^{host} - N_{Li}\mu_{Li} \quad 2-4$$

Since the host structure does not change, the number of host N_{host} does not change.

Therefore the formal transform can be rewritten as

$$\Omega_f^{host} = \frac{\Omega^{host}}{N_{host}} = \frac{G^{host} - N_{Li}\mu_{Li}}{N_{host}} = G_f^{host} = x\mu_{Li} \quad 2-5$$

where x is regard as the Li concentration.

2.2 First principles energy calculations

2.2.1 General energy approximation

First principles theory is commonly used in the energy calculations. As its literal meaning, the theory starts directly at the level of the most basic physics laws, the atomic numbers and quantum mechanics. The Kohn-Sham energy function^[37] can be given that

$$E[\{\psi_i\}] = 2 \sum_i \psi_i \left[-\frac{\hbar^2}{2m} \nabla^2 \psi_i \right] d^3 r + \int V_{ion}(\mathbf{r}) n(\mathbf{r}) d^3 r + \frac{e^2}{2} \int \frac{n(\mathbf{r})n(\mathbf{r}')}{|\mathbf{r}-\mathbf{r}'|} d^3 r d^3 r' + E_{xc}[n(\mathbf{r})] + E_{ion}(\{\mathbf{R}_I\})$$

2-6

where $n(\mathbf{r}) = 2 \sum_i |\psi_i(\mathbf{r})|^2$ is the electronic density. In the right side of the equations, there are five terms that contribute to the total energy. The first item represents the electron kinetic energy from the original Shordinger equations. The second term represents the electron-ion potential energy. The third term represents the electron-electron repulsion interactions. The forth term represents the exchange and correlations of many-electron system beyond the direct coulomb repulsion. And the final term represents the coulomb interactions between different ions.

2.2.2 Density-functional theory

The density-functional theory (DFT) associates all the interactions to a uniform variable, the electronic charge density. The solution of the energy equation is obtained in a self-consistent way to ensure the accuracy. Since only the minimum of the solutions of the energy equation makes sense when investigate the ground state energy, the final term in above equation could be removed. Kohn-Sham equations therefore can be further simplified to^[37]

$$\left[-\frac{\hbar^2}{2m} \nabla^2 + V_{ion}(\mathbf{r}) + V_H(\mathbf{r}) + V_{xc}(\mathbf{r}) \right] \psi_i(\mathbf{r}) = \epsilon_i \psi_i(\mathbf{r}) \quad 2-7$$

where $\psi_i(\mathbf{r})$ is the wave function of electronic state i. V_H is the Hatree potential of the electrons representing the electron-electron repulsion and V_{xc} is the exchange-correlation potential. All the potentials are equations related to the electronic charge density. Using

self-consistent method, as long as the electronic charge density is obtained the total energy could be calculated.

The more difficult problem is to get the exchange-correlation potential. In DFT theory, there are two major approximations to solve this problem, local-density approximation (LDA) and generalized gradient approximation (GGA). In LDA approximation, it is assumed that the exchange-correlation energy per electron equal to the one in a homogeneous electron gas. While in GGA approximation, the detailed deviation of the exchange-correlation potential curve is taken into consideration and used as the criterion to determine the exchange-correlation energy. However, in transition metal ions, the highly localized d electrons could cause the main error of calculation accuracy because of the lack of cancellation of electron self-interaction. A +U method therefore is developed to circumvent this problem and is proved to be successful in Li-intercalation materials^[38].

2.2.3 Pseudopotential approximation

Besides the electron-electron interaction, the electron-ion interactions are also difficult to deal with because of the huge number of core-electrons of each ions. Since the core-electrons are tightly bonding with the nuclei, a large number of wave functions are needed for the fourier transformation, which will highly raise the cost of computation. It is necessary to do the full electron calculation if dealing with the fine electronic structure of the materials. However, most of the time, the major physical properties of the materials are determined by the valence electrons, which is usually no more than eight. The pseudopotential approximation is developed so that all the core-electrons are

simplified as a core and the ion is divided into two parts, the “core” and the valence electrons. A local pseudopotential is set up that it will be exactly the same with the core-electron potential beyond a critical distance r_c from the nuclei.

On one hand, the consistence between pseudopotential and full-electron potential beyond r_c ensures the correction of the properties that determined only by the valence electrons. On the other hand, the complicated core-electrons are substituted by only one potential function therefore the computation cost is highly reduced. Again, since the pseudopotential of each element is only determined by the atomic number of the element, it could also be determined in a self-consistent way.

2.2.4 Periodic simplify

With the improvement of computer source, the atom numbers that could be dealt with have increased from tens to thousands. However, comparing to the order of atom numbers in actual materials (10^{23}), it is still a small number that the computers could dealing with. However, in most crystals, the cells are periodic and the unit cells or supercells are usually composed with several atoms. Therefore using the boundary condition, it is possible to make simulations using a single cell and combine the result with other method such as Monte Carlo simulation to determine the properties of the whole materials.

Bloch’s theorem therefore is important in the calculations. From Bloch’s theorem, the wave functions of the electrons are written as a sum of plane waves with periodic boundary conditions. The Fourier transform transfer the energy from direct lattice to reciprocal lattice. And now the problem is changed to calculate “a finite number of

electronic wave functions at an infinite number of k points”^[37]. However, since the electronic wave functions do not change much in a certain k-space region, it is possible to use the electronic wave functions at a certain k-point as the representation in the certain k-space region. If the k-point mesh is not fine enough, the calculated energy will be apart far from the actual energy therefore is not reliable. On the other hand, if the k-points mesh is set to be too fine, the energy may be more accurate but will take high cost to convergent. The k-point mesh therefore becomes an important parameter during the calculations.

Another important parameter that will make effect on the energy accuracy is the cutoff energy of the electronic-plane wave. Using Fourier transform, theoretically, an infinite set of plane-wave basis is needed to completely expand the electronic wave functions. Again, it is important to find out a cutoff energy value so that when the kinetic energies of the plan-waves are larger then the cutoff energy, their Fourier coefficient is small enough to be ignored. By doing this truncation, the energy could also be convergent under a reasonable accuracy while the number of plan-waves could be reduced to a finite number that could be handling by the computers.

The computer based simulations starts with the most basic properties of the elements and physical principles, therefore can give the key physical and electronic properties of the materials without the disturbance of the side-effect that could happen during the synthesis or characterization processes. However, since there are a lot of approximations in the theory and algorithm, computer-based computation can only simulate materials with periodic structures and the absolute values of the calculated results are correct only in a certain accuracy range. Therefore it is more important to

compare the trend rather than the absolute value when use the computation results to explain the experimental phenomenon or predict the unknown properties.

3 CHARGE DISTRIBUTION AND FACTORS AFFECTING LI MOBILITY IN LiMn₂O₄ SPINEL

In this chapter, LiMn₂O₄ spinel is used as the sample to establish and verify a reliable first principles computational method that can be used to simulate the thermodynamic properties of Li intercalation materials.

3.1 Introduction

LiMn₂O₄ spinel and its derivatives are presently the center of much interest as the cathodes of high-power lithium batteries for transportation applications. The commercialization of the material has been long delayed by the self-discharge problem when left under fully charged, particularly at elevated temperatures; however, this obstacle may be lifted by chemical stabilization with aluminum doping, as well as modifying the salt in electrolyte [39-42].

In principle, it is believed that the spinel phase, whose cubic structure ensures three-dimensional diffusion paths, can deliver high power even though the theoretical capacity of the LiMn₂O₄ is only approximately 140mAh/g in the voltage range of 3.0V to 4.3V. However, the stoichiometric LiMn₂O₄ is found to have inferior rate capability. The volume change between the fully-delithiated material and the pristine material is about 7% [43, 44]. When the material is charged/discharged at room temperature, two voltage plateaus appear at around 4.1V and 4.0V (vs. Li). The two voltage steps are attributed to the order-disorder transition of the Li⁺-vacancy arrangement when the Li concentration is around 50% [43, 45, 46]. In LiMn₂O₄ spinel, half of the Mn ions are Mn³⁺ ions while the others are Mn⁴⁺ ions. During cycling, Mn³⁺ ions disproportionate to Mn⁴⁺ ions and Mn²⁺

ions which spontaneously dissolve into the electrolyte[47, 48]. On the other hand, Mn^{3+} is six-coordinated in $LiMn_2O_4$ spinel thus the Mn^{3+} octahedron has strong Jahn-Teller effect. Although at room temperature, $LiMn_2O_4$ spinel exhibit the cubic structure, it is reported that (partial) charge ordering have been observed at low temperatures, accompanied by the phase transitions from cubic to tetragonal/orthorhombic structures[49-54]. However, a complete ground state charge ordering of $LiMn_2O_4$ is difficult to be confirmed due to current technique limitations.

A number of theoretical/computational investigations have been performed on this material [28, 55-57]. A phase diagram of the $Li_xMn_2O_4$ has been calculated using Local Density Approximation (LDA) to the Density Functional Theory (DFT) [28]. Though in this former study [28] it can successfully explain the phase transformation when x varies from 1 to 2 (cubic to tetragonal phase transformation), the phase stability, lattice change and voltage are not consistent with the experimental observations when x varies in the range of 0 to 1. The main reason can be attributed to the fact, that neither the LDA nor the GGA approach can give the distinguished electronic structures of Mn^{3+}/Mn^{4+} ions in $LiMn_2O_4$, which is experimentally observed with neutron diffraction (ND) and magnetic studies [58, 59]. When referring to the kinetic properties, Molecular Dynamics (MD) simulations and dynamic Monte Carlo simulations have been used to investigate the Li diffusivities in the material [55, 57]. Most of the studies focus on the temperature dependence and Li concentration dependence on the Li diffusivities without considering the valence changes in transition metal ions. It is well known that the change of Li concentration leads to the valence change of the transition metal (Mn) ions. Such change might have a strong effect on the Li mobility in an ionic crystal since lithium

diffusion occurs through a thermally activated state surrounded by transition metal ions (more details given in section 3). It is also experimentally observed that certain doping elements (e.g. Ni) gives remarkable rate capability compared with undoped LiMn_2O_4 [60-62].

The Hubbard U value in the Hamiltonian, needed to correct for the self-interaction error on transition metal oxides in DFT, is implemented in this work. There have been ample evidences showing that the GGA+ U method can give more accurate voltage predictions in transition metal oxides [38, 63]. In GGA method, charges are spuriously delocalized: for example, in LiMn_2O_4 , *all* Mn ions show an average valence of 3.5^+ . On the other hand, GGA+ U method gives half Mn^{3+} and half Mn^{4+} , which more accurately capture the physics in the actual material.

In this chapter, the ground state of Mn charge distribution in LiMn_2O_4 are investigated by GGA+ U method. By comparing the results obtained from GGA and GGA+ U methods, it is found that the redox potentials of LiMn_2O_4 and the trend of lattice parameter change as a function of lithium content can be more accurately calculated with the GGA+ U method. More importantly, it is clearly demonstrated that different valence states of Mn ions and their arrangements surrounding the lithium ions have a profound effect on the activation barrier of lithium diffusion in the spinel structure.

3.2 Computational Methodology

In this work, a supercell composed of eight formula units of $\text{Li}_x\text{Mn}_2\text{O}_4$ is used. 97 distinct $\text{Mn}^{3+}/\text{Mn}^{4+}$ charge orderings can be identified in this cell and all these orderings are used to initialize the $\text{Mn}^{3+}/\text{Mn}^{4+}$ distribution. Calculations were performed in the

spin-polarized GGA and GGA+U approximations to the DFT. Core electron states were represented by the projector augmented-wave method [64] as implemented in the Vienna ab initio simulation package (VASP) [65-67]. The Perdew-Burke-Ernzerhof exchange correlation [68] and a plane wave representation for the wavefunction with a cutoff energy of 400eV were used. The Brillouin zone was sampled with a mesh by Monkhorst packing. The atomic positions and cell parameters are fully relaxed to obtain total energy and optimized cell structure. To obtain the accurate electronic density of states (DOS), a static self-consistent calculation is run, followed by a non-self-consistent calculation using the calculated charge densities from the first step. The cell volume is fixed with internal relaxation of the ions in the second step calculation. A supercell with one vacancy out of eight Li sites ($\text{Li}_7\text{Mn}_{16}\text{O}_{32}$) is used to calculate the Li diffusion activation barriers in Li-rich phase. The Hubbard U correction is introduced to describe the effect of localized *d* electrons of Mn ions. Previous work has shown that the U values can be calculated in a self-consistently way [69]. In spinel structure, the U value of Mn^{3+} ions is 4.64 while the U value of Mn^{4+} ions is 5.04 [38]. Because in LiMn_2O_4 , Mn^{3+} and Mn^{4+} ions co-exist, a unique effective U value of 4.84 is applied in Rotationally invariant LSDA+U approach[70]. Test calculations have been performed to assign distinguished effective U values to Mn^{3+} and Mn^{4+} ions in the same supercell, and similar Mn valence separation can be observed.

3.3 Results and Discussion

3.3.1 Ground state of Mn charge distribution in LiMn_2O_4 spinel

Among the initialized 97 charge orderings, only 22 distinct orderings can be obtained diminishing the symmetric equivalent duplicates. The one with lowest energy is regarded as the ground state, which is 2.8 meV per atom lower than the one with second lowest energy. The calculated energies of all charge orderings are plotted in Figure 3.1(a) sorted by the obtained orderings. In some cases, two or more energies are obtained per ordering due to the lattice parameter differences. The ewald energies of corresponding configurations are plotted in Figure 3.1(b) for comparison. Considering Mn^{3+} and Mn^{4+} as different types of ions, the space group of the ground state LiMn_2O_4 is *Imma* and the atomic positions are shown in following table:

Table 3.1 Atomic positions of new Mn charge distribution ground state in LiMn_2O_4

Atom	Site	Wyckoff positions		
Li	4e	0.00000	0.25000	0.38816
Mn^{4+}	4d	0.25000	0.25000	0.75000
Mn^{3+}	4a	0.00000	0.00000	0.00000
O1	8i	0.22554	0.25000	-0.02721
O2	8h	0.00000	-0.47088	0.25201

$$a=5.77732 \text{ \AA}$$

$$b=5.81709 \text{ \AA}$$

$$c=8.79174 \text{ \AA}$$

For easy understanding, the structure can be transferred back to the conventional cubic cell (in the case of ground state, a tetragonal cell lattice parameters: $a=b=8.20 \text{ \AA}$, $c=8.794 \text{ \AA}$). When Li diffuse in LiMn_2O_4 spinel, it will migrate through a Mn rings composed of 6 Mn ions. In ground state ordering, only two types of local Mn charge

arrangements can be found in the Mn rings. They are shown in Figure 3.2. Orthorhombic lattice can also be found in other orderings which however have higher energies.

Despite the small fluctuations caused by the lattice difference, the trend of total energy vs. different Mn charge ordering is consistent with that of ewald summation energy in general. It indicates that the electrostatic interactions are the dominant factor that determines the low temperature charge ordering. Therefore for the ground state ordering, Mn^{3+} and Mn^{4+} ions are evenly distributed. However, for local Mn charge arrangement in the Mn rings, Mn^{3+} and Mn^{4+} ions are not preferred to arrange alternatively, so as to minimize the strains caused by the connection of distorted Mn^{3+} polyhedrons and undistorted Mn^{4+} polyhedrons. A collective J-T distortion therefore is generated causing the lattice distortion from conventional cubic structure. Tetragonal phase will be obtained for a complete symmetric ordering. Both tetragonal and orthorhombic phases can be obtained for the partial symmetric orderings. These charge orderings provide a good template for the charge initialization of doped spinel $\text{LiM}_{0.5}\text{Mn}_{1.5}\text{O}_4$ which will be discussed in Chapter 4.

3.3.2 Simulated voltage and lattice parameters by GGA and GGA+U method

Within ground state of Mn charge distribution in LiMn_2O_4 obtained, it is possible to calculate the material voltage and change of lattice parameters versus Li concentration. In manganese spinel, phase separations happen while Li ions are intercalating into and de-intercalating from the cathode materials. Rather than forming a solid solution $\text{Li}_x\text{Mn}_2\text{O}_4$ ($0 < x < 1$), experimental studies [43, 71-73] have shown voltage plateaus around 4.0V and 4.1V appears during the charge/discharge processes. There is a small voltage step at x

= 0.5 as the result of a stable Li-vacancy ordered phase. Voltage plateaus appear when there is two phases coexist at certain Li concentration ranges.

For any intercalation system, the voltage can be calculated as described in Chapter 2. In this study, the total energy G of the eight-formula supercell with different Li concentrations $\text{Li}_X\text{Mn}_6\text{O}_{32}$ are obtained from first-principles calculations performed at zero Kelvin. Their formation enthalpies can be calculated and plotted as a function of Li concentration to obtain the formulas of stable phases (results not shown here). When GGA method is applied, $\text{Li}_X\text{Mn}_6\text{O}_{32}$ is stable for each X from 1 to 7, suggesting a solid solution behavior which is contrary to experimental observations. In this case, the chemical potential of Li ions in cathode at each X can be approximated by:

$$\mu_{\text{Li}}^{\text{Li}_X\text{Mn}_6\text{O}_{32}} = dG / dN_{\text{Li}} \approx G_{\text{Li}_{X+1}\text{Mn}_6\text{O}_{32}} - G_{\text{Li}_X\text{Mn}_6\text{O}_{32}} \quad (0 \leq X \leq 8) \quad 3-1$$

When GGA+U is applied, only one stable intermediate phase is found at $X = 4$, suggesting that phase separations happen in two stages, $0 \leq X \leq 4$ and $4 \leq X \leq 8$. In each stage, the chemical potentials of Li ions in both phases are equal, therefore can be approximated by:

$$\mu_{\text{Li}}^{\text{Li}_X\text{Mn}_6\text{O}_{32}} = (G_{\text{Li}_4\text{Mn}_6\text{O}_{32}} - G_{\text{LiMn}_6\text{O}_{32}}) / (4 - 0) \quad (X = 0,4) \quad 3-2$$

and

$$\mu_{\text{Li}}^{\text{Li}_X\text{Mn}_6\text{O}_{32}} = (G_{\text{Li}_8\text{Mn}_6\text{O}_{32}} - G_{\text{Li}_4\text{Mn}_6\text{O}_{32}}) / (8 - 4) \quad (X = 4,8) \quad 3-3$$

Li metal is used as the reference anode materials, and the calculated Li chemical potential in Li metal is $\mu_{\text{Li}}^{\text{anode}} = -1.9$ eV. The voltage profiles calculated by both GGA and GGA+U approaches are plotted in Figures 3.3 (a). The average voltage over all Li concentrations is 3.4V calculated by GGA, which underestimates the voltage by 17.0% when comparing

to the experimental value. The step-wise calculated voltage profile is due to the fact that only average voltages of lithium concentration intervals are computed. With GGA+U methods, the two voltage plateaus are shown at 4.02V and 4.04V due to the presence of one (and only) intermediate stable phase at $\text{Li}_{0.5}\text{Mn}_2\text{O}_4$. Not only the calculated average voltage is with 1% difference from the experimental value, but also the two-phase separations are accurately captured by GGA+U method. The absolute value of the voltage step (20meV) calculated with GGA+U is smaller than the 100meV observed value. This may be due to the coupling effect of Li/vacancy ordering and $\text{Mn}^{3+}/\text{Mn}^{4+}$ ordering in $\text{Li}_{0.5}\text{Mn}_2\text{O}_4$. More vigorous study is underway to explore this complex phenomenon.

Figures 3.3 (b) shows the lattice parameters of the $\text{Li}_x\text{Mn}_2\text{O}_4$ cubic unit cell as a function of Li concentration. At $x = 1$, GGA+U method overestimates the lattice parameter comparing to the experimental observation by 2%, while the absolute value of GGA calculation is closer to the experimental value. However, the total observed volume change from LiMn_2O_4 to Mn_2O_4 is around 6-7% in experiments. Using GGA+U method, the volume change from LiMn_2O_4 to Mn_2O_4 is calculated as 6.3%, while using GGA method, the volume change from LiMn_2O_4 to Mn_2O_4 is only 0.7%. Two sets of experimental data are used for this comparison [43, 44] and the inconsistency in absolute experimental values is the result of different precursors and synthesis conditions.

The Jahn-Teller distortion of individual Mn^{3+} ions can be observed by the lattice parameter change using GGA+U method. In LiMn_2O_4 materials, each Mn ion is surrounded by an octahedron formed by six oxygen ions. The Mn-O bonds are formed with the hybridization between O $2p$ orbitals and Mn $3d$ orbitals. As described in ligand

field theory [74], the octahedral crystal field splits the Mn $3d$ orbitals to two types of orbitals, t_{2g} orbitals with lower energy level and e_g orbitals with higher energy level. When there is a single un-paired electron in e_g orbitals, as in Mn^{3+} ions, the Mn-O bond pointing towards vertex O will be elongated or contracted due to the asymmetric shape of d electron clouds. The effect is well-known as the Jahn-Teller distortion [75]. In Mn_2O_4 structure, no Mn^{3+} exists and the lattice remains perfect cubic in GGA+U calculations. However, in $LiMn_2O_4$ structure, half of the Mn ions are Mn^{3+} , which leads to the remarkable effect of Jahn-Teller distortion and the Mn^{3+} -O bondlengths split, subsequently the structure changes from cubic to tetragonal when lithium concentration $x = 1$. Such cubic to tetragonal phase transformations have been observed in $LiMn_2O_4$ at temperatures below 100K[51, 52, 76]. In GGA method, both Mn_2O_4 and $LiMn_2O_4$ structure maintains cubic structure at zero Kelvin.

3.3.3 Electronic structure of Mn^{3+} and Mn^{4+}

The electron configuration of Mn^{3+} ion is $t_{2g}^3e_g^1$ and Mn^{4+} ion is t_{2g}^3 . The two ions can be distinguished clearly from the differences in DOS calculated using GGA+U method (Figure 3.4). In the projected Mn^{4+} DOS (black), the energy levels of t_{2g} orbitals with spin-up states are lower than the Fermi energy level, indicating that the spin-up states in t_{2g} orbitals are fully occupied. The energy levels of t_{2g} orbitals with spin-down states and the entire e_g orbitals energy levels are above the Fermi energy. These orbitals are unoccupied. The DOS plot is consistent with the t_{2g}^3 electron configuration of Mn^{4+} ion. In the projected Mn^{3+} DOS (red), the spin-up states of e_g orbitals split to two peaks. The energy level of one peak is lower than Fermi energy indicating that one of the e_g

orbitals is occupied, which is consistent with the $t_{2g}^3 e_g^1$ electron configuration of Mn^{3+} ion.

The DOS plot calculated using GGA method is also given as an insert in Figure 3.4 for comparison. Only one type of DOS (blue) can be obtained for *all* Mn ions in the supercell. The spin-up states and half of the spin-down states of t_{2g} orbitals are occupied, indicating an average valence of +3.5 for each Mn ion.

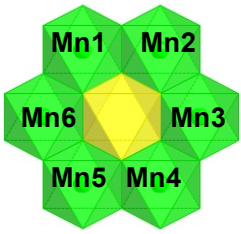
3.3.4 The effect of Mn charge distribution on Li diffusion activation barrier

To understand how the Mn charge distribution will affect the lithium diffusion, we have to look at the atomic arrangement of the spinel $Li_xMn_2O_4$ structure. Figure 3.5(a) illustrates the structure of $LiMn_2O_4$. The spinel $LiMn_2O_4$ belongs to $Fd\bar{3}m$ space group with oxygen ions in $32e$ sites forming a close-packed *fcc* lattice. Mn ions reside on the $16d$ octahedral sites, while the Li ions sit in the $8a$ tetrahedral sites. The $16c$ octahedral sites are left empty. The Li ions diffusion occurs by hopping from one $8a$ site to another $8a$ site through the intermediate $16c$ site (Figure 3.5(b)). Because each face of $8a$ site is shared with a $16c$ site, three-dimensional diffusion paths can be formed inside the structure (Figure 3.5 (c)). Each $16c$ site is surrounded by six Mn ions forming a Mn ring in the plane that is perpendicular to the Li diffusion paths (Figure 3.5 (d)). The total energy of the supercell varies with the migration path of the mobile Li ion and a maximum value is achieved when the Li ions are in the $16c$ sites. The energy difference between Li in the initial state ($8a$) and in metastable state ($16c$) is considered as the Li diffusion activation barrier E_a [55]. In this work, different valence configurations in the

local Mn rings are implemented using GGA+U method, and their effect on Li diffusion activation barriers are investigated.

In each Mn ring, the number of Mn^{4+} ions N_{IV} can vary from 0 to 6. However, when $N_{IV} = 6$ or 0, the structure are energetic unfavorable because they will introduce high charge localization and result in strong columbic interactions inside the structure. In our study, the value of N_{IV} is limited to $1 \leq N_{IV} \leq 5$. For each value of N_{IV} , different Mn^{3+} - Mn^{4+} arrangements can be found and each of them is treated as a distinct configuration. A total number of seven configurations are investigated. They are listed in Table 3.2 and labeled by characters from “a” to “g”. For each configuration, the corresponding Li diffusion activation barriers are calculated.

Table 3.2 Mn valence configurations in Mn-rings surrounding the diffusing Li^+ in the activated site

	# of Mn^{4+}	label	Mn1	Mn2	Mn3	Mn4	Mn5	Mn6
	5	a	+4	+4	+4	+4	+4	+4
4	b	+4	+4	+4	+3	+4	+4	+3
	c	+4	+4	+4	+3	+4	+4	+3
3	d	+4	+3	+4	+3	+4	+3	+3
	e	+4	+4	+3	+4	+3	+4	+3
2	f	+4	+3	+3	+4	+3	+4	+3
1	g	+4	+3	+3	+3	+4	+3	+3

The calculations are performed in a Li-rich phase supercell ($\text{Li}_7\text{Mn}_{16}\text{O}_{32}$). The variations of Li diffusion barriers versus the number of Mn^{4+} ions in the Mn rings are depicted in Figure 3.6(a). When Li ions are in the $16c$ site, the $16c$ site octahedral volumes and distances of the mobile Li to its nearest Mn ions are also analyzed. The results are presented in Figure 3.6(b) and Figure 3.7(c), respectively. The seven

configurations can be sorted to three categories by different ranges of Li diffusion activation barriers: (separated by dash lines in Figure 3.6(a)), (1) Low barrier case ($E_a < 400$ meV); (2) Medium barrier case; (3) High barrier cases ($E_a > 750$ meV).

(1) In low barrier case, there are more Mn^{4+} ions than Mn^{3+} ions in the Mn ring, suggesting that Li ions are more favored to be surrounded by Mn^{4+} ions. The reason can be attributed to the electrostatic effect. As there are three types of cations in LiMn_2O_4 , Li^+ ions, Mn^{3+} ions and Mn^{4+} ions, the combination of Li^+ ions and Mn^{4+} ions can minimize the positive charge localization and further reduce the total energy of the system. Comparing to Mn^{3+} ions, the electron clouds of Mn^{4+} ions are less dense, causing weaker Mn-O interaction and longer Mn-O bondlength. Consequently, the Li-O bondlength is shortened, leading to smaller Li *16c* site octahedral volumes (Figure 3.6(a) a,b,c). On the other hand, the Li^+ - Mn^{4+} distances are longer than Li^+ - Mn^{3+} distances due to the stronger coulombic repulsion between Li^+ and Mn^{4+} than Li^+ and Mn^{3+} , as shown in Figure 3.6(c) for configurations a and b “Li-Mn bondlengths” split. For configuration c, the different trend may be attributed to the asymmetric $\text{Mn}^{3+}/\text{Mn}^{4+}$ distribution in the ring. When Li is closer to some Mn^{3+} ions, it is also closer to another Mn^{4+} ion, therefore when the electrostatic balance is reached, the Li- $\text{Mn}^{3+}/\text{Mn}^{4+}$ distances spread with wide distribution.

(2) In medium barrier case, the number of Mn^{4+} ions is smaller than Mn^{3+} ions. There is one more electron in Mn^{3+} ion than in Mn^{4+} ion and the hybridization between O 2p electrons and Mn 3d electrons are stronger. The Mn-O bondlengths are shortened, leaving more space for the Li *16c* site (Figure 3.6(b) f,g). The total screening effect of the

electron clouds between Li ions and Mn ions are strengthened, as a result, the “Li-Mn bondlength” split disappears (Figure 3.6 (c) f,g).

(3) In high barrier case, the numbers of Mn^{4+} ion and Mn^{3+} ion are equal. In configuration d, Li cannot be stabilized in $16c$ site, indicating that lithium diffusion through this type of activated site is energetically unfavorable. The specific high energy barrier of configuration e might be attributed to the local Jahn-Teller effect of Mn^{3+} . As mentioned in section 3.3.2, the Jahn-Teller effect will elongate or contract the Mn $16d$ octahedron along the axis pointing to the vertex O ions. Figure 3.6 (d) presents the Mn-O bondlength for a Mn^{3+} ion and a Mn^{4+} ion. The two Mn ions are from the Mn rings with configuration e, but the trend is consistent in all configurations. The Mn-O bondlengths of a Mn^{4+} ion are almost the same while there is a bondlength split for the Mn^{3+} ion. Therefore, the Mn^{3+} octahedron is highly distorted and the positions of their O ions are displaced from their ideal positions. In the Mn rings, adjacent Mn octahedrons share two oxygen ions as vertex, therefore, if a Mn^{3+} is adjacent to a Mn^{4+} , the octahedron edge-misfit will be introduced, leading to high internal strains. When the number of Mn^{4+} ion and Mn^{3+} ion is equal, many Mn^{3+} - Mn^{4+} adjacencies are created. These internal strains might cause the diffusing Li ions less stable and elevate the diffusion barriers.

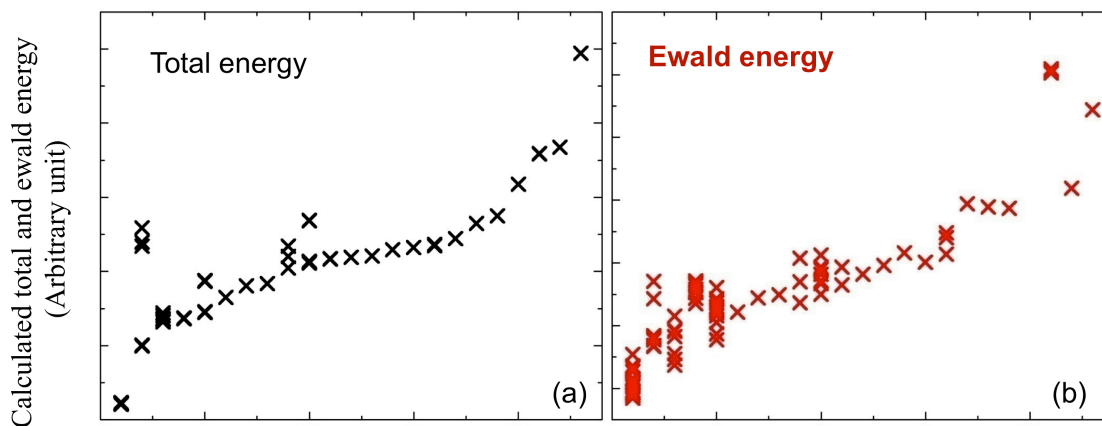
Above results reveal that a larger amount of Mn^{4+} ions may enhance the ionic conductivity by lowering local Li diffusion activation barriers. We speculate this could be one of the main contributing factors for the improved rate capability in Ni, Co or Cu doped manganese spinel materials[60, 77, 78], since these doping elements are in 2+ and push more Mn ions to 4+.

3.4 Conclusion

As a summary of the above, in LiMn_2O_4 spinel material, the electrostatic interaction is the main factor determining the low temperature charge ordering. The collective J-T distortion is the reason causing the cubic to tetragonal/orthorhombic lattice transition. For volume changes and lithium intercalation voltages, the results obtained from GGA+U method are qualitatively more accurate than those obtained by GGA method. The Mn^{3+} and Mn^{4+} ions can be distinguished by introducing the Hubbard U correction in the DFT. Surprisingly, the higher amount of Mn^{4+} ions enhances the ionic conductivity by making local Li diffusion activation barriers lower. Our study clearly shows the necessity in correcting self-interaction in localized electron systems, such as LiMn_2O_4 . More importantly, the results shed some light on understanding the role of local charge distribution on the lithium diffusion activation barrier of the LiMn_2O_4 spinel materials.

Chapter 3, in part, is a reprint of the material "Factors affecting Li mobility in spinel LiMn_2O_4 - A first-principles study by GGA and GGA+U methods", as it appears in *Journal of Power Sources*, 195 (15), 2010. Bo Xu, Ying S. Meng, 2010. The dissertation author was the primary investigator and author of this paper.

Figures:



The labels of obtained Mn charge orderings

Figure 3.1 Calculated total energy and ewald energy of LiMn_2O_4 with different Mn charge distribution

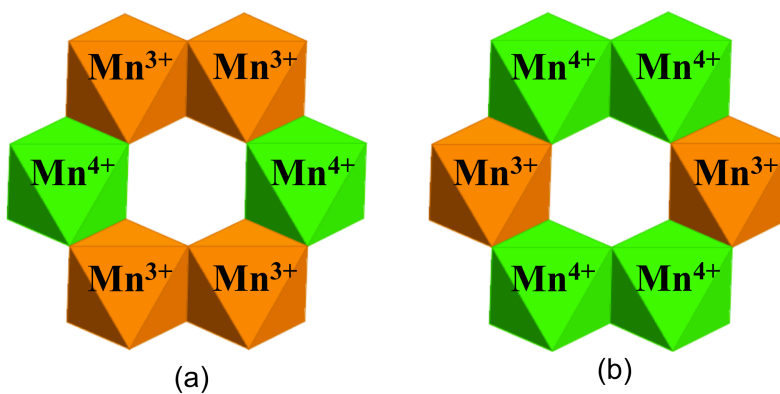


Figure 3.2 Local Mn charge arrangements in LiMn_2O_4 ground state (green: Mn^{4+} ; orange: Mn^{3+})

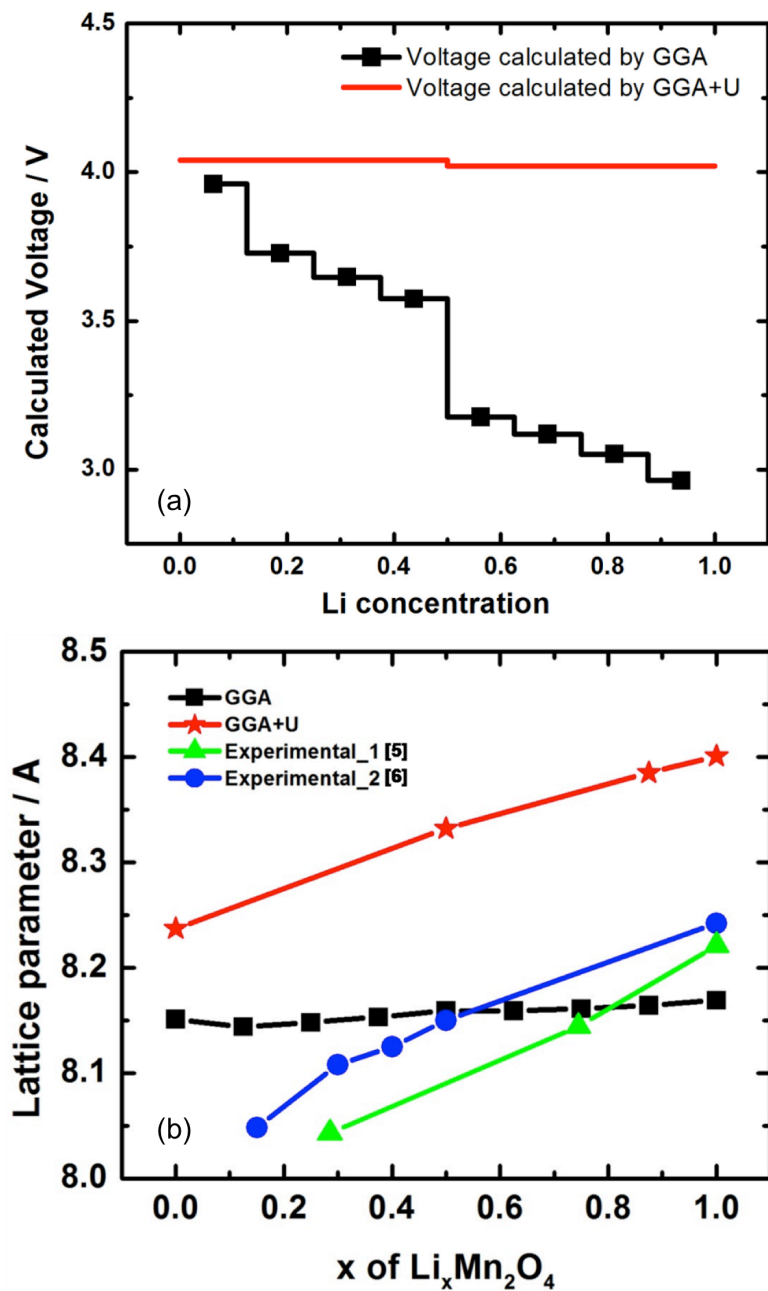


Figure 3.3 (a) Voltage calculated by GGA and GGA+U methods; (b) Calculated and experimentally measured lattice parameters of the $\text{Li}_x\text{Mn}_2\text{O}_4$ cubic unit cell as a function of Li concentration.

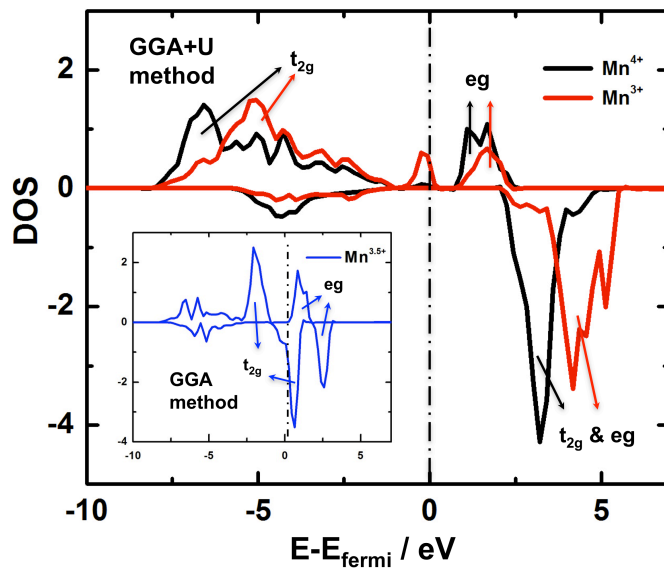


Figure 3.4 Mn 3d electron Density of State (DOS) plots using GGA+U and GGA (insert) methods

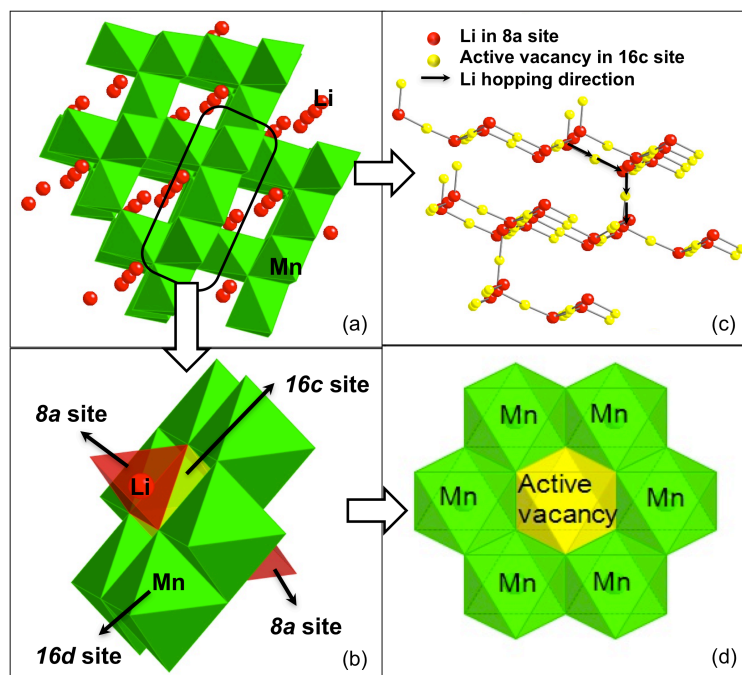


Figure 3.5 Three-dimensional lithium diffusion paths in LiMn_2O_4

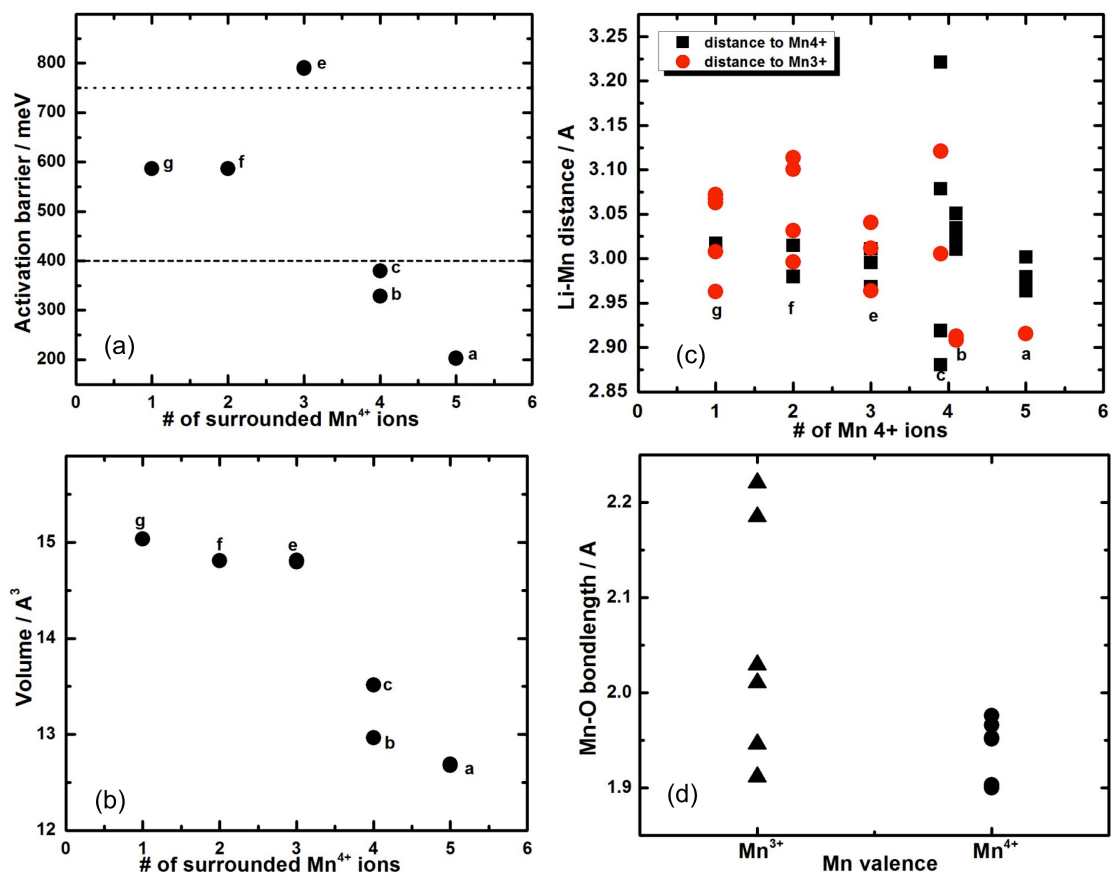


Figure 3.6 (a) Local environment dependent Li diffusion activation barriers in $\text{Li}_7\text{Mn}_{16}\text{O}_{32}$; (b) Active Li $16c$ site octahedral volumes; (c) Distances between the mobile Li ion and surrounding Mn ions; (d) Mn-O bondlengths of $\text{Mn}^{3+}/\text{Mn}^{4+}$ in configuration e.

4 FIRST PRINCIPLES STUDY ON DOPED SPINEL $\text{LiM}_{0.5}\text{Mn}_{1.5}\text{O}_4$ (M =Ti, V, Cr, Fe, Co, Ni, Cu)

Based on the first principles method established in Chapter 3, a systematic computational study on doped spinel $\text{LiM}_{0.5}\text{Mn}_{1.5}\text{O}_4$ (M =Ti, V, Cr, Fe, Co, Ni, Cu) is performed. Ordered M-Mn charge distributions are adopted in the atomic structural models. The valence states of the doped transition metal ions are identified through calculated electronic density of states (DOS). Li diffusion barriers in this series of materials within different local environments are investigated by GGA method. Within obtained conclusions, new types of bi-doped high voltage high rate spinel materials $\text{LiNi}_x\text{Cu}_y\text{Mn}_{2-x-y}\text{O}_4$ is designed.

4.1 Introduction

As mentioned in previous chapters, LiMn_2O_4 tends to exhibit capacity fade in the 4V region, particularly at elevated temperatures. Factors such as Mn dissolution into the electrolyte and the development of micro-strains[21] during cycling have been suggested to be the main sources of capacity fade. The poor cycling performance could be improved by partial substitution of Mn with other metals, an approach of making the $\text{LiM}_x\text{Mn}_{2-x}\text{O}_4$ (M = Co, Mg, Cr, Ni, Fe, Al, Ti, Cu, Zn etc.) electrode material [21]. It has been found that a higher voltage plateau (>4V) accompanies some transition metal doping [21]. Among all $\text{LiM}_x\text{Mn}_{2-x}\text{O}_4$ materials, $\text{LiNi}_{0.5}\text{Mn}_{1.5}\text{O}_4$ is an attractive high voltage cathode material since it offers a flat voltage plateau at 4.7 V and demonstrates a reversible capacity >135mAh/g[21]. Several strategies were developed to improve the rate capability of $\text{LiNi}_{0.5}\text{Mn}_{1.5}\text{O}_4$. J. C. Arrebola et al. obtained excellent rate properties by

homogeneously mixing nano and micro size $\text{LiNi}_{0.5}\text{Mn}_{1.5}\text{O}_4$ powders[21], or by adding polyethyleneglycol(PEG) to increase the crystallinity and decrease the strain[21]. The rate capability was also affected by the atomistic structure of the spinel material, as proposed by M. Kunduraci et al[21]. It is found that nonstoichiometric $\text{LiNi}_{0.5}\text{Mn}_{1.5}\text{O}_{4-x}$ ($Fd\bar{3}m$) exhibited better structural reversibility at high rate compared with stoichiometric $\text{LiNi}_{0.5}\text{Mn}_{1.5}\text{O}_4$ ($P4_332$). The oxygen deficiency leads to the presence of a small amount of Mn^{3+} in the pristine materials, which leads to better electronic conductivities in the material. The Cu doped spinel materials were investigated by a few research groups[21]. Although the Cu-rich spinel electrodes provide lower discharge capacity than Ni-rich spinel electrodes, it is more stable during electrochemical cycling. Moreover, $\text{LiCu}_x\text{Mn}_{2-x}\text{O}_4$ has a higher electronic conductivity than other spinel $\text{LiM}_x\text{Mn}_{2-x}\text{O}_4$ materials (Cr, Fe, Co, Ni) [21], because Cu can participate in the charge transport process. All the previous work focused mainly on the electronic conductivity in the doped spinel $\text{LiM}_x\text{Mn}_{2-x}\text{O}_4$ materials. Little has been explored to enhance the lithium ionic diffusivity in this family of materials. Using *ab initio* computational modeling, it is possible to rapidly screen the effect of different doping elements on the lithium diffusion activation barrier, as well as the redox potentials in the spinel structure. *Ab initio* computational method was firstly used by Van der Ven et al. to determine the energy barrier of Li diffusion in layered transition metal oxides[79]. Kang et al. also used this method to identify the factors that limits Li^+ -ion hopping in layered oxide and successfully synthesize an optimized layered material with superior rate capability [79].

Many researchers have already shown that the cycling performance of $\text{LiNi}_{0.5}\text{Mn}_{1.5}\text{O}_4$ can be improved by doped with different transition metal ions[79].

However, a systematic understanding on the effects of co-doped elements is still lacking. In this work, first principles computation, based on density functional theory (DFT), is used to examine the voltage profile and electronic structures of the $\text{LiM}_x\text{Mn}_{2-x}\text{O}_4$ ($M = \text{Ti}, \text{V}, \text{Cr}, \text{Fe}, \text{Co}, \text{Ni}, \text{Cu}$). The Li diffusion activation barriers in each material are calculated and compared. Based on the computational pre-screening, our experimental research focuses on $\text{LiNi}_x\text{Cu}_y\text{Mn}_{2-x-y}\text{O}_4$ ($0 < x < 0.5, 0 < y < 0.5$) which have the potential to achieve high voltage, high rate and good cycling performance, while keeping relatively high capacity.

4.2 Computational Methodology

The conventional spinel supercell composed of eight formula units of $\text{LiM}_{0.5}\text{Mn}_{1.5}\text{O}_4$ is used. The input structure of $\text{LiM}_{0.5}\text{Mn}_{1.5}\text{O}_4$ belongs to space group $P4_332$. Ordered cation arrangements are adopted, that doped M ions occupy the $4b$ octahedral sites and Mn $12d$ octahedral sites. The details of the computation parameters are described in Chapter 3. The effective U values are either taken from previous references[38] or obtained from fitting to lattice parameters of corresponding oxides. In some cases, one element can have different valence states in the same material, therefore small adjustments are made to the reference U values, so that each transition metal ion has a unique effective U value applied in the rotationally invariant LSDA+U approach[70]. The effective U values are listed below in Table 4.1:

Table 4.1 Effective U values used for the first row transition metal ions in $\text{LiM}_{0.5}\text{Mn}_{1.5}\text{O}_4$

Ti	V	Cr	Mn	Fe	Co	Ni	Cu
0	3	2	5	4.6	5	5.96	7

4.3 Results and discussion

4.3.1 The redox mechanism of $\text{LiM}_{0.5}\text{Mn}_{1.5}\text{O}_4$

The two-step voltages of $\text{LiM}_{0.5}\text{Mn}_{1.5}\text{O}_4$ are calculated. The results are compared with experimental values in. Electronic structure calculations are also performed to investigate the oxidation states of doped M ions as well as their valence change during cycling. Table 4.2 shows the calculated 3d electron configurations of M ions, their valence states in $\text{LiM}_{0.5}\text{Mn}_{1.4}\text{O}_4$, and the percentage of amount of Mn^{3+} ions over all Mn ions.

Table 4.2 Calculated 3d electron configurations, valence states and of M ions, and the percentage of amount of Mn^{3+} ions in $\text{LiM}_{0.5}\text{Mn}_{1.4}\text{O}_4$

Dopant	3d electron configurations	valence states	Mn^{3+} Percentage
Ti	$t_{2g}^0 e_g^0$	+4	67%
V	$t_{2g}^1 e_g^0$	+4	67%
Cr	$t_{2g}^3 e_g^0$	+3	33%
Fe	$t_{2g}^3 e_g^2$ (high spin)	+3	33%
Co	$t_{2g}^5 e_g^2$ (low spin)	+2	0%
Ni	$t_{2g}^6 e_g^2$	+2	0%
Cu	$t_{2g}^6 e_g^3$	+2	0%

The M ion 3d electron configurations are obtained qualitatively from the calculated electronic density of states (DOS), shown in Figure 4.2. There is a clear trend that the valences of doped M ions decrease while the M ion atomic number increases. Table 4.3 shows the lattice parameters of $\text{LiM}_{0.5}\text{Mn}_{1.5}\text{O}_4$. For sake of clearance, c is defined as the longest lattice constant. The percentage of Mn^{3+} amount is also included for comparison.

Table 4.3 Lattice parameters and corresponding c/a , c/b ratio of $\text{LiM}_{0.5}\text{Mn}_{1.5}\text{O}_4$

Dopant	a (Å)	b (Å)	c (Å)	c/a ratio	c/b ratio	Mn ³⁺ Percentage
Ti	8.28	8.28	8.83	1.07	1.07	67%
V	8.40	8.14	8.82	1.05	1.08	67%
Cr	8.29	8.29	8.52	1.03	1.03	33%
Fe	8.31	8.31	8.53	1.03	1.03	33%
Co	8.34	8.33	8.34	1.00	1.00	0%
Ni	8.29	8.29	8.29	1.00	1.00	0%
Cu	8.22	8.22	8.46	1.00	1.00	0%

Co and Ni doped materials exhibit no collective J-T distortion which exists in all the other ones. It is clear that the collective J-T distortion is proportional to the amount of Mn³⁺ ions. The calculated voltages agree with the experimental values in general. The exception of Co dopant may be originated from the non-perfected Co potentials as a well-known artifactual problem.

For Ti, V, Cr, and Fe doped spinel, because the dopants are either 3+ or 4+ ions, Mn³⁺ ions cannot be fully suppressed. The collective J-T distortion still exists in these materials. While charging, Mn³⁺ ions are oxidized to Mn⁴⁺ first, followed by the oxidization of M³⁺ to M⁴⁺ (if exist). However, V is the only exception. In V doped spinel, V⁴⁺ will be oxidized to V⁵⁺ first. The calculated V⁴⁺/V⁵⁺ redox potential is 4.11V, which however is very close to the calculated Mn³⁺/Mn⁴⁺ redox potential (4.19V).

For Co and Ni doped spinel, all Mn are pushed to 4+ and none of the cations are J-T ions. Therefore a cubic structure is maintained in these materials. The M ions behave as the only redox couples and are oxidized from 2+ to 4+. For Cu doped spinel, although

all Mn ions are also Mn^{4+} ions, Cu^{2+} is a weak J-T ion, therefore a weak collective J-T distortion can still be observed. Cu^{2+} can only be oxidized to Cu^{3+} and the redox mechanism of this specific material will be discussed in details in section 4.3.3.

4.3.2 Li diffusion barriers in $Li_xM_{1/2}Mn_{3/2}O_4$ (M= Ti, V, Cr, Fe, Co, Ni and Cu)

As shown in Chapter 3, when Li ions diffuse in the un-doped $LiMn_2O_4$ spinel structure, the diffusion activation barriers are reached when Li ions occupy the intermediate 16c sites which are surrounded by six Mn ions forming a Mn ring [80]. A similar situation occurs in the doped spinel $Li_xM_{1/2}Mn_{3/2}O_4$ (M= Ti, V, Cr, Fe, Co, Ni and Cu); however, the rings are now composed of two types of metal ions - Mn and the doped transition metal ion M. In the supercell used for this work, for each dopant, two distinct local environments of transition metal ion rings can be found. One is composed of three doped M ions and three Mn ions alternatively arranged (Figure 4.3(a)). The other one is composed of one doped M ions and five Mn ions (Figure 4.3(b)). The corresponding Li diffusion barriers with different dopants (M= Ti, V, Cr, Fe, Co, Ni and Cu) are calculated using GGA method (Figure 4.4). The Li diffusion barrier in un-doped Mn spinel[80] is also provided as the reference. Comparing to the un-doped Mn spinel material, the average Li diffusion barrier remains largely unchanged when Ni and Fe ions are present. The average diffusion barrier increases with Ti, V, Cr doping and decreases with Co and Cu doping. Specifically when only one Cu or three Co ions appears in the ring, the Li diffusion barrier can be reduced to as low as 256 meV, respectively. The results of calculated Li diffusion barriers therefore suggest that by doping Co and Cu ions, the

material Li mobility may be able to be enhanced. On the other hand, doping Cu ions will also reduce the material reversible capacity as described in the next section.

4.3.3 The redox mechanism of $\text{LiCu}_{0.5}\text{Mn}_{1.5}\text{O}_4$

As shown in previous chapters, the introduction of the Hubbard U correction accurately captures the charge/discharge voltages of the Li-intercalation spinel materials. More importantly different valence states of the same transition metal ions can be distinguished. Calculations using GGA+U method are performed on $\text{LiCu}_{1/2}\text{Mn}_{3/2}\text{O}_4$ spinel with different Li concentrations. In the first model, where Cu ions occupy $4b$ octahedral sites and Li ions occupy $8c$ tetrahedral sites, the calculated average voltage of $\text{Li}_x\text{Cu}_{1/2}\text{Mn}_{3/2}\text{O}_4$ ($0.5 < x < 1$) is 4.44V, which is 7% higher than the experimental low voltage plateau. In addition, the calculated average voltage of $\text{Li}_x\text{Cu}_{1/2}\text{Mn}_{3/2}\text{O}_4$ ($0 < x < 0.5$) is 5.36V, which is 9% higher than the experimental high voltage plateau. The projected electronic density of states (DOS) of Cu 3d orbitals in $\text{Li}_x\text{Cu}_{1/2}\text{Mn}_{3/2}\text{O}_4$ ($x=1, 1/2, 0$) are calculated and presented in Figure 4.5(a), Figure 4.5(b) and Figure 4.5(c), respectively. In the proposed spinel model, the octahedral crystal field splits the Cu 3d orbitals into two parts. d_{xy} , d_{yz} , and d_{zx} orbitals belong to the t_{2g} orbitals with lower energy levels while d_z^2 and $d_{x^2-y^2}$ belong to the e_g orbitals with a higher energy level[74]. Figure 4.5(a) shows the projected DOS of Cu ions in the fully-lithiated phase $\text{LiCu}_{1/2}\text{Mn}_{3/2}\text{O}_4$. Both spin-up and spin-down states of the three t_{2g} orbitals are below the Fermi energy, which means the t_{2g} orbitals are completely occupied. For e_g orbitals, the d_z^2 orbital is occupied, but the spin-up state of the $d_{x^2-y^2}$ orbital is above the Fermi energy indicating that the $d_{x^2-y^2}$ orbital is half empty. The DOS plot is consistent with the $t_{2g}^6 e_g^3$ electron

configuration of Cu^{2+} ions. The projected DOS of Cu ions in the half-delithiated phase $\text{Li}_{1/2}\text{Cu}_{1/2}\text{Mn}_{3/2}\text{O}_4$ (Figure 4.5(b)) and in the fully-delithiated phase $\text{Cu}_{1/2}\text{Mn}_{3/2}\text{O}_4$ (Figure 4.5(c)) are generally the same minus trivial differences in shape. It suggests that Cu ions are in the same valence state in the two compositions. The spin-up states of the e_g orbitals are completely empty while all of the other electronic states are occupied. The DOS plots indicate the electron configuration of $t_{2g}^6 e_g^2$ consistent with Cu^{3+} ions. Based on these results from first-principles calculation, the Cu valence in doped spinel $\text{LiCu}_{1/2}\text{Mn}_{3/2}\text{O}_4$, is Cu^{2+} at fully lithiated state. The Cu^{2+} ions can be oxidized to Cu^{3+} ions when half of the Li ions are extracted. Valence higher than 3+ cannot be obtained and the calculated voltage of the $\text{Cu}^{2+}/\text{Cu}^{3+}$ redox couple is 4.44V. When more than half of the Li ions are extracted, the charge densities of oxygen ions change significantly, suggesting that the extra electrons may be provided by oxygen ions.

If one exchanges the sites of Cu ions with half of the Li ions, a defect spinel model can be created with tetrahedral Cu and octahedral Li included. For the defect spinel system, its total energy is 493 meV per formula higher than the perfect spinel system and therefore the structure should be thermodynamically less stable. However, the experimental synthesis is often conducted at relatively high temperatures ($>700^\circ\text{C}$) and a certain amount of transition metal and lithium ion site mixing occurs. The change of Cu valence versus Li concentration is investigated using a similar method as described above. Tetrahedral Cu^{2+} can also be oxidized to Cu^{3+} but no higher valence can be obtained. In the defect spinel model, Li ions in octahedral sites are preferred to be extracted first and the calculated voltage is 4.58V. The calculated voltage step for removing the remaining tetrahedral Li is 4.99V, a surprisingly high value.

Compared to the NiMn spinel $\text{LiNi}_{1/2}\text{Mn}_{3/2}\text{O}_4$, in which Ni^{2+} can be oxidized to Ni^{4+} providing two electrons per ion, the reversible capacity of Cu doped spinel may be reduced as Cu ions can only provide one electron per ion. However, when doped with a small amount of Cu, it is possible to lower the Li diffusion activation barriers so that better rate capability can be obtained. To further understand the crystal structure, electronic structure and electrochemical properties in a new series of bi-dopant spinel materials, collaborators in University of Florida synthesized and studied the $\text{LiNi}_x\text{Cu}_y\text{Mn}_{2-x-y}\text{O}_4$ with different amount of dopants ($x=0, 0.05, 0.10, 0.25$ and 0.5). Among this series, $\text{LiNi}_{0.25}\text{Cu}_{0.25}\text{Mn}_{1.5}\text{O}_4$ shows the best electrochemical performances which are shown in Figure 4.6. Although the capacity of the doped spinel materials decreases with the increasing doped Cu amount, $\text{LiCu}_{0.25}\text{Ni}_{0.25}\text{Mn}_{1.5}\text{O}_4$ spinel oxide exhibits higher capacity than undoped $\text{LiNi}_{0.5}\text{Mn}_{1.5}\text{O}_4$ spinel at high rates.

4.4 Conclusion

When first row transition metal ions are doped, the valences of doped ions range from $4+$ to $2+$ with increasing atomic numbers. Only late transition metal ions such as Ni and Co may completely suppress the formation of Mn^{3+} ions. However, some of the doped M ions (such as Cu) are also J-T ions, therefore low temperature phase transition similar to LiMn_2O_4 may also be observed in these materials. Li diffusion activation barriers of $\text{LiM}_{1/2}\text{Mn}_{3/2}\text{O}_4$ ($M= \text{Ti, V, Cr, Fe, Co, Ni}$ and Cu) are calculated. Specific dopant such as Co and Cu can significantly reduce the Li diffusion barriers. Although Cu^{2+} can only be oxidized to Cu^{3+} instead of Cu^{4+} therefore doping Cu could reduce the material reversible capacity, bi-doped spinel $\text{LiNi}_x\text{Cu}_y\text{Mn}_{2-x-y}\text{O}_4$ ($0 < x < 0.5, 0 < y < 0.5$) can

be designed within small amount of Cu doped in to $\text{LiNi}_{0.5}\text{Mn}_{1.5}\text{O}_4$. Experimental results suggest that the high rate electrochemical performance of this new type of high voltage spinel materials are significantly improved.

Chapter 4, in part, is a reprint of the material "Electronic, Structural and Electrochemical Properties of $\text{LiNi}_x\text{Cu}_y\text{Mn}_{2-x-y}\text{O}_4$ ($0 < x < 0.5$, $0 < y < 0.5$) High-Voltage Spinel Materials", as it appears in Chemistry of Materials, 23 (11), 2011. Ming-Che Yang, B. Xu, J. Cheng, C. Pan, B. Hwang and Ying S. Meng, 2011. The dissertation author was the primary investigator and author of this paper.

Figures:

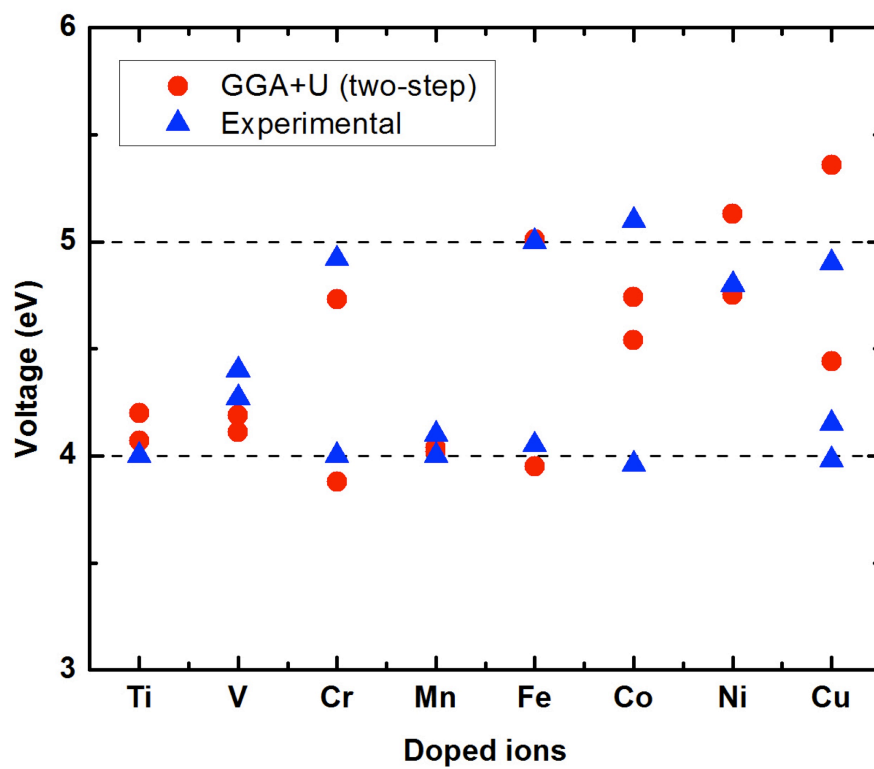


Figure 4.1 Calculated and experimental two-step voltages of $\text{LiM}_{0.5}\text{Mn}_{1.5}\text{O}_4$

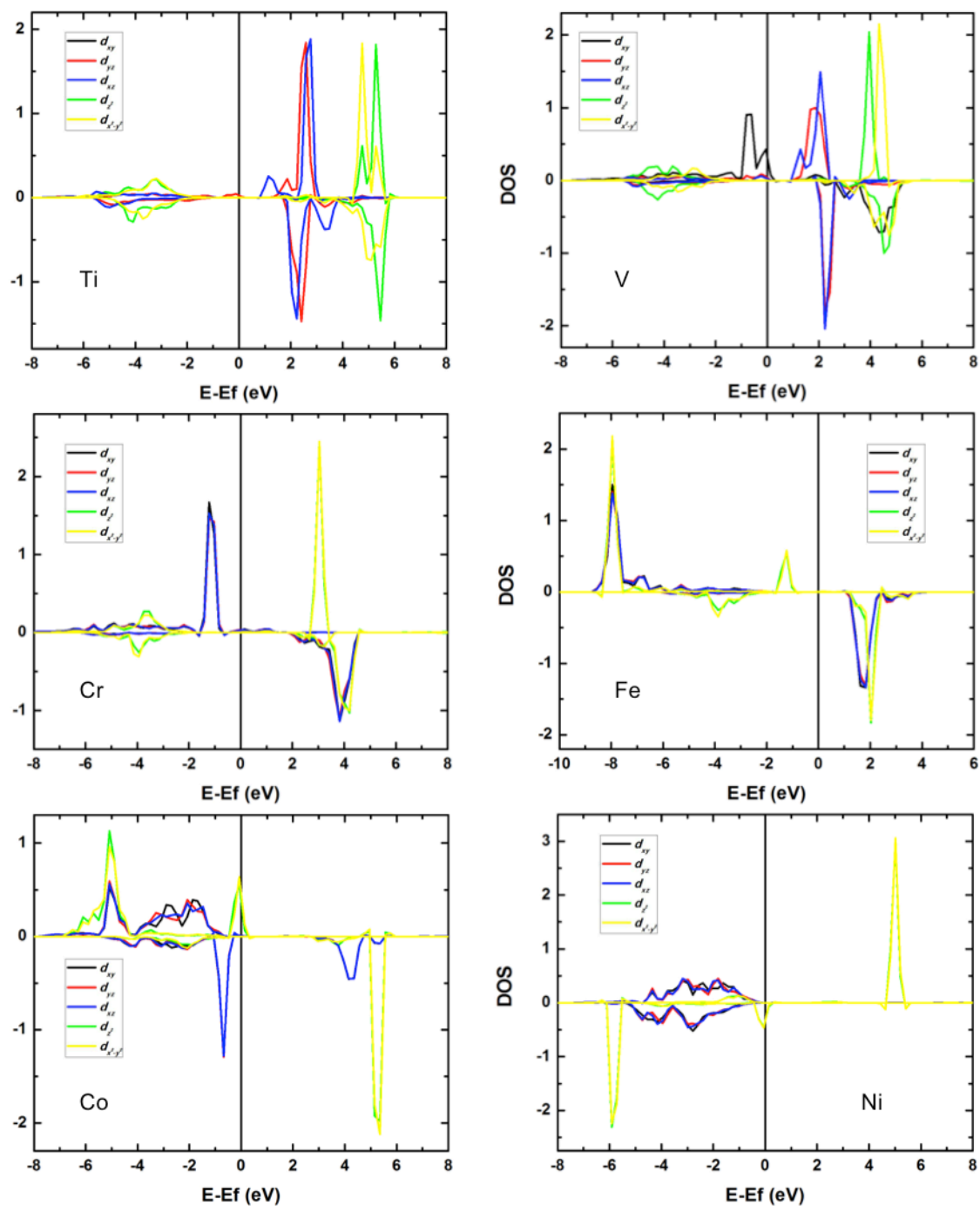


Figure 4.2 Calculated electronic density of states (DOS) of M ions in $\text{LiM}_{0.5}\text{Mn}_{1.5}\text{O}_4$ (M=Ti, V, Cr, Fe, Co, Ni)

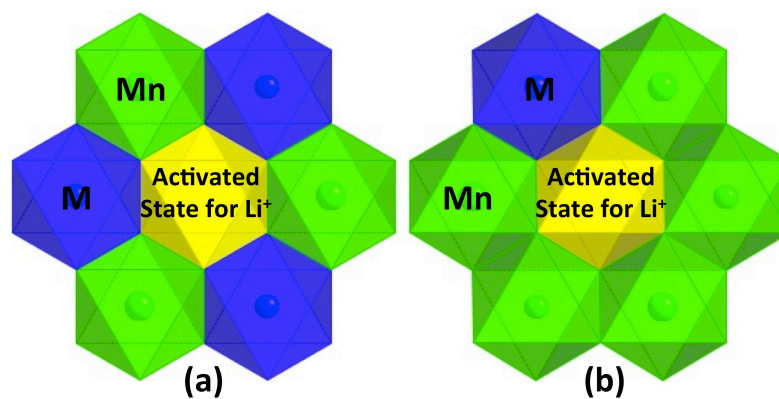


Figure 4.3 Local environments of transition metal ion rings (a) Three M ions in the ring
(b) One M ion in the ring

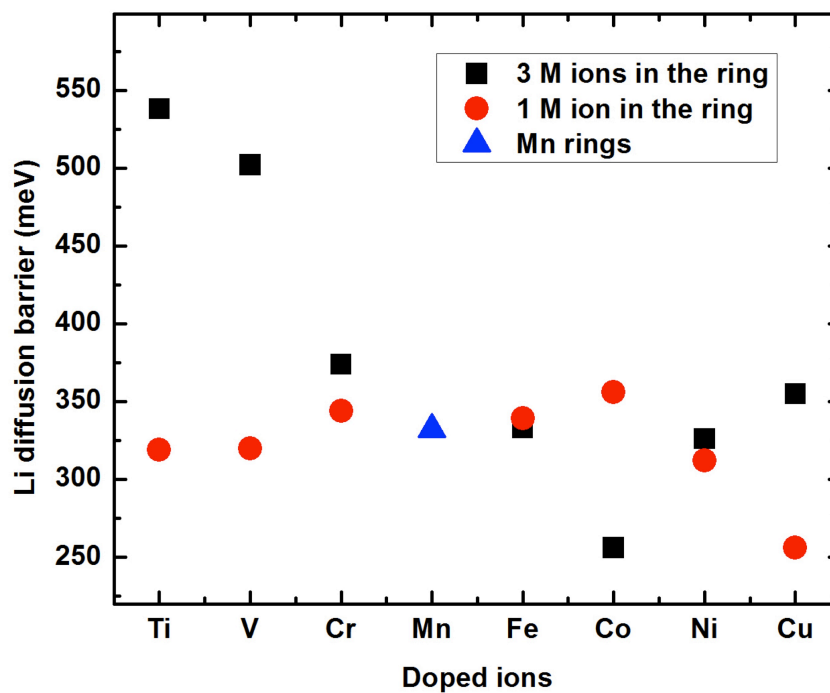


Figure 4.4 Li diffusion barriers in $\text{LiM}_{0.5}\text{Mn}_{1.5}\text{O}_4$ ($M = \text{Cr}, \text{Fe}, \text{Co}, \text{Ni}, \text{Cu}, \text{Mn}$) calculated

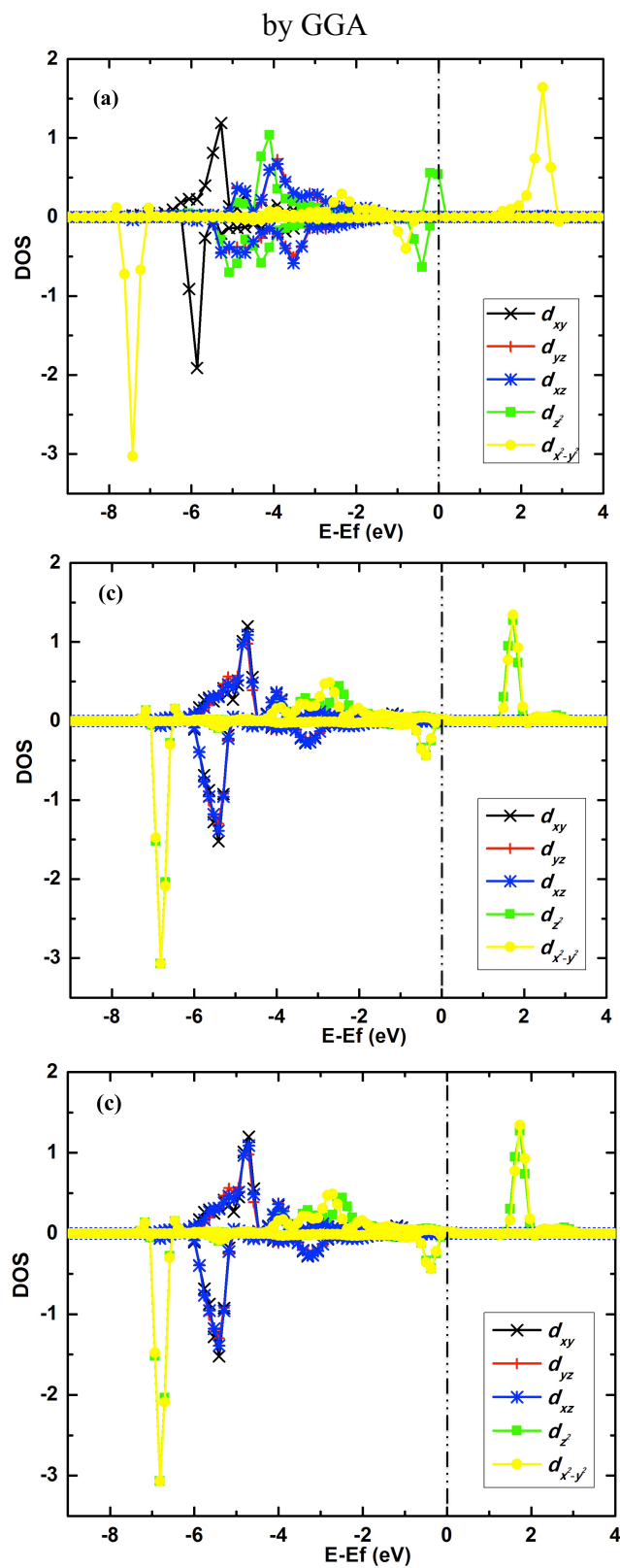


Figure 4.5 Calculated DOS of Cu in $\text{Li}_x\text{Cu}_{1/2}\text{Mn}_{3/2}\text{O}_4$ ((a) $x=1$ (b) $x=1/2$ (c) $x=0$)

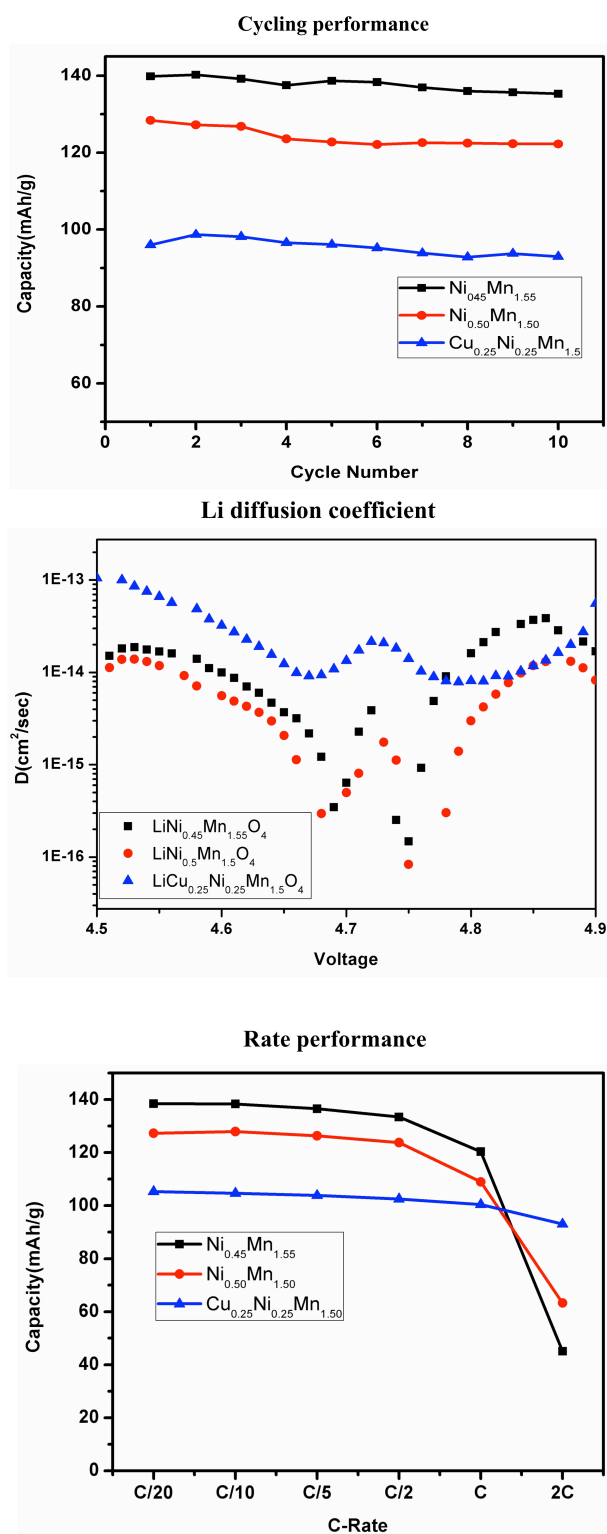


Figure 4.6 Electrochemical performances of $\text{LiNi}_{0.25}\text{Cu}_{0.25}\text{Mn}_{1.5}\text{O}_4$

5 IDENTIFYING SURFACE STRUCTURAL CHANGES IN LAYERED LI-EXCESS LAYERED NICKEL MANGANESE OXIDES IN HIGH VOLTAGE LITHIUM ION BATTERIES

While the design of the new types spinel materials will improve the rate capability of the cathode materials, improvement of layered materials will increase the material capacity. From this section, the research focuses will be switched from the spinel compounds to the layered compounds. First principles method will be used as a powerful tool to identify the sophisticated problems that are difficult to approach by conventional experimental technology.

The series of Li-excess layered oxide compounds $\text{Li}[\text{Ni}_x\text{Li}_{1/3-2x/3}\text{Mn}_{2/3-x/3}]\text{O}_2$ ($0 < x < 1/2$) are investigated in a joint study combining both computational and experimental methods. The bulk and surface structures of pristine and cycled samples of $\text{Li}[\text{Ni}_{1/5}\text{Li}_{1/5}\text{Mn}_{3/5}]\text{O}_2$ are characterized by synchrotron X-Ray diffraction together with aberration corrected Scanning Transmission Electron Microscopy (*a*-S/TEM). Electron Energy Loss Spectroscopy (EELS) is carried out to investigate the surface changes of the samples before/after electrochemical cycling. Combining first principles computational investigation with our experimental observations, a detailed lithium de-intercalation mechanism is proposed for this family of Li-excess layered oxides. The first cycle charging stage of the material can be divided into two representative regions. In the first region (voltage < 4.45V), formation mechanism of tetrahedral lithium ions is proposed. In the second region (voltage > 4.45V), we explain how the transition metal (TM) ions migrate into the Li layer causing the phase transformation of the materials, predominantly on the surface of the materials. We show clear evidence of a new spinel-like solid phase

formed on the surface of the electrode materials after high-voltage cycling. It is proposed that such surface phase transformation may be part of the sources contributing to the first cycle irreversible capacity and the main reason for the intrinsic poor rate capability of these materials.

5.1 Introduction

Rechargeable Lithium Ion Battery (LIB) is one of the most important energy storage technologies today. Layered transition metal oxides, based on either LiCoO_2 or LiNiO_2 are currently used in portable electronic devices due to their high operating voltage and high specific capacity 140-160mAh/g. To enable LIB as the main on-board storage technology in plug-in hybrid electric vehicles (PHEVs) or electric vehicles (EVs), higher energy density materials such as the “Li-excess” layered oxides, formed as the composites between $\text{Li}[\text{Li}_{1/3}\text{Mn}_{2/3}]\text{O}_2$ and LiMO_2 ($\text{M} = \text{Ni}, \text{Mn}, \text{Co}$), are promising candidates as they offer much higher capacity (>250mAh/g) and better safety with much reduced cost[9, 81, 82]. It is now well known that in the bulk of the pristine materials, the excess Li^+ ions form an ordered pattern with Mn^{4+} ions in the transition metal (TM) layer, with most of the Li surrounded by 5 or 6 Mn ions[83-85]. During the initial charging region, the capacity originates from the oxidation of Ni^{2+} to Ni^{4+} up to 4.4 V. A high voltage plateau region up to 4.8V appears after that and the anomalous high capacities have been attributed either to an irreversible loss of oxygen from the lattice during the first charge accompanied by Li removal[82, 86, 87] or to the surface reaction through electrode/electrolyte reduction and/or hydrogen exchange[84, 88]. Although a clear explanation of the source of the additional capacity is still under debate, previous work

consistently showed that the Li/Mn ordering disappeared upon electrochemical cycling to 4.8V, indicating significant cation re-arrangement in the bulk of the materials. Armstrong et. al has proposed a general mechanism involving the migration of transition metal ions from surface to bulk during cycling[86], while Jiang et. al provided evidence suggesting that a second phase may be generated in the high voltage region[84]. It is also shown that the lithium chemical diffusion coefficient was lowered significantly at the plateau region, as the result of this dynamic cation re-arrangement[89]. The structural changes in the bulk are believed to happen mainly during the first charge since the plateau does not re-appear in the subsequent cycles. Nevertheless, the large first cycle irreversible capacity and the inferior rate capability of these materials are hindering the commercial application of these materials.

Much research efforts have been devoted to address these two issues. The most promising approaches for reducing the irreversible capacity loss involve surface coating of the cathode surface with other oxides or fluorides like Al_2O_3 , AlPO_4 and AlF_3 [33, 34]. The exact mechanisms for the surface coating are still not well understood. Wu and Manthiram proposed that the reduction in irreversible capacity loss by surface coating was attributed to the retention of part of the oxygen ion vacancies in the lattice upon first charge[33]. Our recent investigation on uncoated pristine $\text{LiLi}_{1/3-2x/3}\text{Ni}_x\text{Mn}_{2/3-x/3}\text{O}_2$ revealed that the reversible discharge capacity was affected by the surface characteristics of as-synthesized material[89]. Even without any coating, the first cycle irreversible capacity could be significantly reduced by controlling the precursor chemistry: If the surface adsorbed $-\text{OH}$ group can be eliminated, the irreversible capacity is less than 40mAh/g without any surface coating [89]. The low rate capability of the pristine

material was proposed to be a possible result from the formation of a thick amorphous solid-electrolyte interface (SEI) on the surface of the material during oxygen loss on charging to 4.8V.[84] Though the composition of the amorphous surface layer is undetermined. Recently Kang and Thackeray reported a new surface coating of Li-Ni-PO₄, which leads to reversible capacity of 200mAh/g at C/1 rate[90]. They speculated that one of the component Li₃PO₄ acts as an excellent lithium ion conductor as well as an efficient protective layer stabilizing the electrode surface, though it is not clear how would Li₃PO₄ stabilizes the electrode surface.

Despite much work on this family of materials, a detailed understanding regarding the stability of the surface of the material is still lacking. In depth investigations are necessary to indentify surface structural changes associated with the cation migrations in the *pristine* layered lithium-excess oxides. In this work, we carried out Synchrotron X-Ray Diffraction (XRD), aberration corrected Scanning Transmission Electron Microscopy (*a*-S/TEM) and Electron Energy Loss Spectroscopy (EELS) combined with electrochemical testing on Li[Ni_xLi_{1/3-2x/3}Mn_{2/3-x/3}]O₂ (x=1/5) compounds to identify how the surface and bulk changed after the first charge/discharge cycle. First principles computation was performed on the model compound Li[Ni_xLi_{1/3-2x/3}Mn_{2/3-x/3}]O₂ (x=1/4) to help guide the experimental investigations and better rationalize the highly complicated experimental observations.

5.2 Methodologies

5.2.1 Synthesis

A novel coprecipitation technique was used for the synthesis of the materials which was previously described[89]. Transition metal nitrates, $\text{Ni}(\text{NO}_3)_2 \cdot 6\text{H}_2\text{O}$ (Fisher) and $\text{Mn}(\text{NO}_3)_2 \cdot 4\text{H}_2\text{O}$ (Fisher), were titrated into a stoichiometric $\text{LiOH} \cdot \text{H}_2\text{O}$ solution for a duration of two hours. The co-precipitated transition metal hydroxides were then filtered using a vacuum filter and washed three times with deionized water. The collected transition metal hydroxides were dried in an oven at 180°C for 10 hours in air. The dried transition metal precursors were mixed with a stoichiometric amount of $\text{LiOH} \cdot \text{H}_2\text{O}$ corresponding to the amount of $\text{M}(\text{OH})_2$ from the coprecipitation step. This mixture was ground for 30 minutes to ensure adequate mixing and then placed into a furnace at 480°C for 12 hours. The precalcinated powders were prepared as a pellet for high temperature sintering. These samples were then calcinated at 1000°C for 12 hours in air. Samples were brought back to room temperature by furnace cooling.

5.2.2 Electrochemistry

For the electrochemical charge/discharge at different C-rate and cycling experiments, cathodes were prepared by mixing the $\text{Li}[\text{Ni}_{1/5}\text{Li}_{1/5}\text{Mn}_{3/5}]\text{O}_2$ with 10 wt% Super P carbon (TIMCAL) and 10 wt % poly-vinylidene fluoride (PVDF) in N-methyl pyrrolidone (NMP) solution. The slurry was cast onto an Al foil using a doctor blade and dried in a vacuum oven at 80°C . The electrode discs were punched and dried again at 80°C for 6 hrs before storing them in an argon filled glove box (H_2O level $< 2\text{ppm}$). 2016 type coin cells were used to study the electrochemical behavior of the compounds and

cycled samples for XRD and TEM. Lithium metal ribbon and 1M LiPF₆ in a 1:1 ethylene carbonate: dimethyl carbonate (EC:DMC) solution (Novolyte) were used as the counter electrode and electrolyte, respectively. Celgard model C480 separator (Celgard Inc, USA) was used as the separator. The coin-cells were assembled in an argon filled glove box and tested on an Arbin battery cycler in the galvanostatic mode. The tests were conducted between 2.0 and 4.8V at a constant current rate of C/50 unless otherwise mentioned. Electrochemical impedance spectroscopy (EIS) measurements were carried out using a Solartron 1287 & Solartron 1260 frequency response analyzer system at room temperature with metallic lithium as the counter and reference electrodes in the frequency range of 10kHz to 10mHz at an AC voltage of 10mV. The cell voltage was potentiostatically stepped at 20mV increments and held. The EIS measurement began at each held voltage when the measured current fell below a current of 10 μ A corresponding to a C/200 rate.

The samples for XRD and TEM were recovered by disassembling cycled batteries in an argon-filled glovebox. The cathode was washed by Acetonitrile (H₂O<10ppm) 3 times. The cathode was allowed to dry in Argon atmosphere overnight. The powder was scraped and mounted in a hermitically sealed capillary for ex-situ x-ray diffraction. For ex-situ TEM sample preparation, the powders were suspended on a copper grid with lacey carbon. The approximate time of sample exposed to air (from a sealed environment to the microscope column) is less than 10 seconds.

5.2.3 X-ray diffraction

Powder diffractions of all samples were taken using synchrotron x-ray diffraction at the Advanced Photon Source (APS) at Argonne National Laboratory (ANL) on beamline 11-BM ($\lambda = 0.4122\text{\AA}$). Cycled samples were hermetically sealed in 1.0 mm kapton capillaries to minimize air-exposure. The beamline uses a sagittally focused x-ray beam with a high precision diffractometer circle and perfect Si(111) crystal analyzer detection for high sensitivity and resolution. Instrumental resolution at high Q is better than $\Delta Q/Q \approx 2 \times 10^{-4}$, with a typical 2θ resolution of $< 0.01^\circ$ at 30 keV XRD data analysis was carried out by Rietveld refinement method using FullProf and GSAS/EXPGUI software [91-93].

5.2.4 *a*-STEM/EELS

Electron Microscopy work was carried out on a Cs-corrected FEI Titan 80/300-kV TEM/STEM microscope equipped with a Gatan Image Filter Quantum-865. All STEM images and EELS spectra were acquired at 300KV and with a beam size of $\sim 0.7\text{\AA}$. EELS spectra shown in this work were acquired from a square area of $\sim 0.5 \times 0.5\text{nm}$ with an acquisition time of 3secs and a collection angle of 35mrad. HAADF images are obtained with a convergence angle of 30mrad and a large inner collection angle of 65mrad. To minimize possible electron beam irradiation effects, EELS and HAADF figures here are acquired from areas without pre-beam irradiation.

Computation methods

The first principles calculations were performed in the spin-polarized GGA+U approximations to the Density Functional Theory (DFT). Core electron states were

represented by the projector augmented-wave method[64] as implemented in the Vienna ab initio simulation package (VASP)[65-67]. The Perdew-Burke-Ernzerhof exchange correlation[68] and a plane wave representation for the wavefunction with a cutoff energy of 450eV were used. The Brillouin zone was sampled with a dense k-points mesh by Gamma packing. The supercell is composed of twelve-formula units of $\text{Li}[\text{Ni}_{1/4}\text{Li}_{1/6}\text{Mn}_{7/12}]\text{O}_2$. The lattice shows a layered structure. The atomic positions and cell parameters are fully relaxed to obtain total energy and optimized cell structure. To obtain the accurate electronic structures, a static self-consistent calculation is run, followed by a non-self-consistent calculation using the calculated charge densities from the first step. The cell volume is fixed with internal relaxation of the ions in the second step calculation. The Hubbard U correction was introduced to describe the effect of localized *d* electrons of transition metal ions. Each transition metal ion has a unique effective U value applied in the rotationally invariant LSDA+U approach[70]. The applied effective U value given to Mn ions is 5eV and to Ni ions is 5.96eV, consistent with early work on $\text{LiNi}_{1/2}\text{Mn}_{1/2}\text{O}_2$ [94].

5.3 Results

5.3.1 Electrochemical properties

Electrochemical measurements of $\text{Li}[\text{Li}_{1/5}\text{Ni}_{1/5}\text{Mn}_{3/5}]\text{O}_2$ electrodes were performed in lithium half-cells cycled between 2.0 to 4.8V. Figure 5.1a displays the voltage (V) versus capacity (mAh/g) electrochemical curves for $\text{LiLi}_{1/5}\text{Ni}_{1/5}\text{Mn}_{3/5}\text{O}_2$ in galvanostatic mode at C/50 for the first charge/discharge cycle. During the first charge step, the voltage in the cell increases monotonically until 4.4V, and reaches a plateau

region between 4.4 and 4.6V. The discharge capacity of first cycle is 255mAh/g, around 50mAh/g less than the first cycle charge capacity. Figure 5.1b shows the capacity versus cycle number of $\text{Li}[\text{Ni}_{1/5}\text{Li}_{1/5}\text{Mn}_{3/5}]\text{O}_2$ electrodes. The material shows steady reversible cycling reaching capacities exceeding 200mAh/g at C/50 and C/20 rates. Electrochemical impedance spectroscopy (EIS) was performed to study the change of impedance in the $\text{Li}[\text{Li}_{1/5}\text{Ni}_{1/5}\text{Mn}_{3/5}]\text{O}_2/\text{Li}$ half cell as a function of the state of charge (SOC). Figure 5.2 compares the EIS spectra of the cell at 3.8, 4.0, 4.2, 4.4, 4.5 and 4.6V. The impedance spectra were analyzed using physical processes that could be represented as a combination of resistive/capacitive elements. Due to the nonhomogeneity of the composite electrode system reflected as depressed semicircles in the impedance response, constant phase elements are used in place of capacitors to model the data. The equivalent circuit in the insert of Figure 5.2 was used for fitting of the data. The cross points are experimentally measured data and the line is from the equivalent circuit fitting. Table 5.1 shows the values obtained from the equivalent circuit fitting of the electrolyte resistance, R_e , surface resistance, R_s and charge transfer resistance, R_{ct} . At low voltages, the figure exhibits two depressed semicircles at the high frequency regimes and a sloped line at low frequencies. The impedance spectra changes shape as the voltage increases. The size of the second lower frequency semicircle increases in diameter and the sloped line disappears as the voltage increases from 4.40 V to 4.60 V. The distinct regions on the figure represent separate time constants in the delithiation process. The first semicircle in the high frequency region is potential independent and represents the lithium ion diffusion across the electrode/electrolyte (solid/liquid) interface. The intercept of the first semicircle at the highest frequency with the real axis (Z_{re}) corresponds to the ohmic

resistance originating from the electrolyte (R_e). The second semicircle in the middle frequency region is related to the charge transfer region between the surface film and the $\text{Li}[\text{Li}_{1/5}\text{Ni}_{1/5}\text{Mn}_{3/5}]\text{O}_2$ particle interface. The diameter of this second semicircle represents the charge transfer resistance (R_{ct}). At lower voltages (up to 4.4V) and lower frequencies, a narrow Warburg region followed by a sloped line. This region is attributed to solid-state diffusion of Li ions into the bulk cathode material.[95] Before the plateau region at 3.80, 4.00, 4.20 and 4.40 V, the capacities correspond to 15, 50, 75 and 100 mAh/g, respectively. During this region, the surface resistance R_s reduces slightly, while the solid diffusion represented by the linear Warburg region and the charge transfer resistance remain relatively constant. Once the voltages reach the plateau region between 4.50 and 4.60 V, the surface resistances remain relatively constant, while the major changes in the spectra is dominated by a significant increase in the charge transfer resistance (R_{ct}). This trend is in contrast with other conventional layered transition metal oxide cathode materials (e.g. LiCoO_2) where R_{ct} was observed to decrease with the states of charge.[95, 96]

5.3.2 XRD

X-ray diffraction pattern of pristine $\text{Li}[\text{Li}_{1/5}\text{Ni}_{1/5}\text{Mn}_{3/5}]\text{O}_2$ shows the pristine phase is a typical well layered phase with < 3% Li/Ni mixing. X-ray diffraction pattern of the material following 10 electrochemical cycles are shown in Figure 5.3 and refined using a single phase (Fig 3a) as listed in the inset table. The superlattice peaks between 20-30° observed in pristine materials disappeared in the cycled materials. Based on the capacities observed, the cycled material has 0.8 Li remaining in the structure. Compared

to the pristine materials, a significant c lattice expansion is observed accompanied by an increased amount of Li/Ni interlayer mixing. The Rietveld refinement using a single layered phase provides reasonably good fitting based on the R_{wp} and R_b fitting factors; however, large mismatch of the (003) peak can be observed clearly as shown in the inset in Figure 5.3a. To correct this mismatch, a two-phase refinement including a second phase was performed. The fitting pattern is shown in Figure 5.3b and the refinement results are listed in Table 5.2. Both of the layered phases show an expanded lattice, however one phase shows little Li/Ni interlayer mixing and the other layered phase shows increased Li/Ni mixing compared to the pristine material. The inset in Figure 5.3b shows significant improvement in fitting of the (003) peak based on two phases. Rietveld refinement included tetrahedral Li ions in one of the two layered phase was also performed and the results are listed in Table 5.3. R_{wp} and R_B fitting factors can be further reduced when $\sim 13\%$ tetrahedral Li ions are included. More details on the formation of tetrahedral Li will be discussed in later sessions.

5.3.3 STEM

Figure 5.4 and 5 depict electron microscopy data from the pristine sample and cycled sample (at the discharge state after 10 cycles between 2 to 4.8V). The particles show a high degree of crystallinity and well faceted surfaces. Multiple grains were selected for study and the results are consistent, therefore only representative data are shown here. Images acquired by an HAADF detector with a small convergence angle and a relative large inner collection angle are also called “Z-contrast” images, where the contrast is proportional to $Z^{1.7}$. [97, 98] In atomic resolution Z-contrast images, the

contrast of the atomic columns thus can be used to differentiate different elements and provide atomic-structural information.

Figure 5.4a is a typical Z-contrast image recorded along the [1 0 0] zone axis and Figure 5.4b shows a high magnification image from a selected area in Figure 5.4a. The arrays of atomic columns are clearly revealed. The atomic columns in the horizontal direction are separated by a distance of 4.3\AA , corresponding to the (100) projection of $\sqrt{3}a$ superlattice in layered structure; and 4.8\AA in the vertical direction, corresponding to $1/3$ of typical c lattice in layered structure. The zoomed-in image in Figure 5.4b clearly shows a pattern of two brighter columns followed by a darker column; such pattern is a direct result of the cation ordering in the TM plane: Two TM-rich columns (higher Z) and one Li-rich column (lower Z). An atomistic model is placed next to the HAADF image for clarity. The well layered properties in the bulk of the pristine material extend to the surface. Moreover, the stacking sequence of the ordered TM layers along the (001) c -direction is random. Our observations are consistent with previous report on uncoated pristine $\text{LiLi}_{1/5}\text{Ni}_{1/5}\text{Mn}_{3/5}\text{O}_2$ material by Lei et.al.

Figure 5.5a shows traditional bright field images of the surface and bulk of the material following 10 electrochemical cycles recorded along the [1 0 0] zone axis. A 2-5 nm amorphous layer was observed on the surface of the material, which might be related to the side reaction of electrolyte at high voltage ($>4.5\text{V}$). Detailed analysis of this layer will be discussed in a separated paper. The HAADF image in Figure 5.5b shows that the bulk of the grains still maintains the well layered structure as in seen in Figure 5.4. The surface structure of the cycled grains, however, is obviously changed based on the contrast change of the atomic columns. Along the (001) direction, the dark columns of

bulk (Li atomic columns) become much brighter on the surface. In fact, their contrast is almost comparable to their neighboring TM columns. This suggests that a significant amount of transition metal ions migrate into the Li sites resulting in a loss of the layered characteristics at the surface of the materials.

5.3.4 EELS

Figure 5.6a compares the EELS spectra of the oxygen K-edge and the manganese L_3 and L_2 edges from the surface and bulk of the pristine and cycled samples respectively. The fine structure and energy position of O-K and Mn-L edges imprints the electronic structure of the sample and thus can be used to study the structural evolution on the cycled surface. The energy position and fine structures of Mn-L edges are almost identical on the spectra from the pristine surface and bulk, and the cycled bulk. However, those from cycled surface area slightly shift to a lower energy loss, which indicates a decreased oxidation state of Mn. This is also proved by its relatively higher L_3/L_2 ratio, which is a well-known indicator of oxidation state variations in transition metals.[99, 100] Fine-structure modifications of O-K edges are noticeable on the spectrum from the cycled surface compared to the other spectra. The first peak, at energy loss of $\sim 532\text{eV}$ almost vanished on the spectrum from the cycled surface. This O-prepeak can be attribute to the transition of 1s core state to the unoccupied O-2p states hybridized with TM-3d states. The decreased intensity of this peak on the cycled surface likely indicates the modification of unoccupied states of TM-3d and bonding lengths of TM-TM. These electronic structure change correlates well with the atomic structure modification revealed by Z-contrast imaging. EELS quantification shows that O/Mn ratio variation

among the cycled surface and bulk is less than 5%, which imply that no significant oxygen loss in the cycled sample. In contrast, obvious Li loss (more than 50%) was found on the cycled surface, see Figure 5.7. This is consistent with the fact that significant TM atoms occupy Li site on the cycled surface, which is revealed by Z-contrast imaging (Figure 5.5).

5.3.5 First-principles calculations

The compound $\text{Li}[\text{Ni}_{1/4}\text{Li}_{1/6}\text{Mn}_{7/12}]\text{O}_2$ is modeled as a solid solution of Li_2MnO_3 and $\text{LiNi}_{0.5}\text{Mn}_{0.5}\text{O}_2$. For the convenience to interpret computation results, the formula of this compound will also be referred as $\text{Li}_{14/12}\text{Ni}_{1/4}\text{Mn}_{7/12}\text{O}_2$. There are four layers in each supercell, two oxygen layers, one transition metal (TM) layer and one Li layer. Each layer is composed of twelve ions, forming a $\sqrt{3}\times\sqrt{3}$ in-plane supercell. Oxygen ions are close-packed and stacked in ABC (O3) stacking, serving as the frame, while TM slab and Li slab stack alternatively. Several models of fully-lithiated $\text{Li}_n/12\text{Ni}_{3/12}\text{Mn}_{7/12}\text{O}_2$ ($n=14$) are created and the calculated total energies are compared. In the model with the lowest energy, Li layer supercell is composed of 12 Li ions (Figure 5.8b) and the in-plane cation ordering of the TM layer is shown in Figure 5.8a. There are two “excess” Li ions located in the TM layer, one Li ion is surrounded by 6 Mn ions and the other Li ion is surrounded by 5 Mn ions plus 1 Ni ion. The Ni ions are arranged in the “broken zigzag” shape. In this model the cation arrangements are most consistent with experimental observations including NMR, electron diffraction and x-ray diffraction and is used as the basis to investigate the lithium de-intercalation mechanism of the materials. Although the models we propose here are all solid-solutions of Li_2MnO_3 and

$\text{LiNi}_{0.5}\text{Mn}_{0.5}\text{O}_2$, phase separations may happen. The mixing energy calculated by following equation is around +40 meV per formula. Note that in the synthesis of this series of materials, 900-1000 °C heating temperature is used, that very likely overcomes a small positive mixing energies.

The formation enthalpy of $\text{Li}_{n/12}\text{Ni}_{1/4}\text{Mn}_{7/12}\text{O}_2$ ($8 < n < 14$) versus lithium concentration is calculated with two reference states set as $n=8$ and $n=14$ (Figure 5.8c). When $n=8$, all Ni ions are oxidized to the highest valence state. Further removal of Li ions beyond this critical lithium concentration will result in the additional capacities related to non-redox centers. The calculated voltages listed in the inset of Figure 5.8c, range from 3.86V to 4.48V, well matched with the experimental measurements. At each concentration, various Li-vacancy configurations are calculated and those with lowest energies are depicted by red crosses in Figure 5.8c. These configurations usually involve tetrahedral Li ions (Li_{tet}) formed in the Li layer. Structures of Li_{oct} -vacancy configurations are also investigated and the most stable ones among calculated configurations are depicted by the green dots. Below certain lithium concentrations ($n < 11$), however, these configurations usually have higher energies. The blues stars in Figure 5.8c depict the structures based on a defect spinel model as illustrated in Figure 5.9. In the defect-spinel model, the Li layer supercell is composed of 11 Li ions with 1 Ni ion, and the TM layer in-plane cation ordering is shown in Figure 5.9a. When $n=14$, the TM ions in the TM layer are arranged following the Mn lattice in [111] plane of spinel LiMn_2O_4 illustrated in Figure 5.9b. Therefore, when $n=8$, the formula of the compound $\text{Li}_{2/3}\text{Ni}_{1/4}\text{Mn}_{7/12}\text{O}_2$ can be re-written as $\text{Li}[\text{Li}_{1/3}\text{Ni}_{1/2}\text{Mn}_{7/6}]\text{O}_4$, forming a Li-excess defect-spinel phase where part of the $16d$ octahedral sites are occupied by Li ions (Figure 5.9c).

In a perfect spinel phase, only transition metal ions reside on $16d$ sites. At fully lithiated state ($n=14$), the formation enthalpy of this defect-spinel phase is +105 meV and at $x=8$ the formation enthalpy of this phase is -101 meV with respect to the corresponding layered form.

Calculations of electronic structures are performed on $\text{Li}_{n/12}\text{Ni}_{1/4}\text{Mn}_{7/12}\text{O}_2$ at ($0 < n < 14$). For $n < 8$, structures are modeled without introduction of oxygen vacancies. The valences of TM ions are estimated from the calculated TM magnetizations. In Figure 5.10, the average of Ni and Mn magnetizations are plotted versus lithium concentration. For Mn ions, the average magnetization retained is $3.1 \mu_B$ per ion when $n > 8$, consistent with a high spin Mn^{4+} . It increases slightly to $3.4 \mu_B$ per ion when $n < 8$, mainly due to the significant change of electron density around oxygen ions. Careful inspection of the projected density of the state (see supporting information S5) of Mn ions confirm that the valence state of Mn is unchanged as $4+$. For Ni ions, the average magnetization almost linearly reduces from $1.7 \mu_B$ per ion to $0.4 \mu_B$ per ion when $n > 8$. This is expected as all high spin Ni^{2+} ions are oxidized to low spin Ni^{4+} , which has been seen experimentally.[101] When $n < 8$, the average Ni magnetizations fluctuates around $0.5 \mu_B$. The charges of oxygen ions are also investigated from the change of charge density (difference between spin-up electrons and spin-down electrons) distribution over oxygen layer. Three different states of charge are shown in Figure 5.11. For clarity, in Figure 5.11a part of the oxygen layers of $\text{Li}_{n/12}\text{Ni}_{1/4}\text{Mn}_{7/12}\text{O}_2$ supercell is presented by the pink balls together with the adjacent TM slab. The corresponding spin density of this region at $n=14$, 8, and 0, are presented respectively in Figure 5.11b, c, and d. At full lithium

concentration ($n=14$), Mn ions are $4+$ and the electron configuration is t_{2g}^3 ; Ni ions are $2+$ and the electron configuration is $t_{2g}^6 e_g^2$. For both ions, the difference between spin-up electrons and spin-down electrons are positive. At $n=14$, well bonded oxygen $2p$ electrons can be clearly observed in Figure 5.11b. The charges density of Ni are mostly screened by oxygen charge densities, but the charges of Mn ions can still be partially observed. At $n=8$, the charge density distribution is similar to that at $n=14$, but the shape of oxygen $2p$ electron clouds begins to distort, suggesting a potential change of oxygen charge density. At $n=0$, oxygen charge density changes significantly. Note that no oxygen vacancies are allowed in the current work. It indicates that the extra electrons that cannot be provided by the Ni redox couples are coming from oxygen ions. The charge densities of Mn ions increase slightly, possibly due to weakening of Mn-O bonding, which is consistent with the results of Mn magnetization calculations as described above.

5.4 General discussion

The choice of composition for first principles computation is primarily limited by the size of supercell that is reasonable with modern computation resources. So far we have presented all experimental characterization on $\text{Li}[\text{Ni}_{1/5}\text{Li}_{1/5}\text{Mn}_{3/5}]\text{O}_2$, previous reports and our study on other compositions have proven that the lithium excess layered oxide, $\text{Li}[\text{Ni}_x\text{Li}_{1/3-2x/3}\text{Mn}_{2/3-x/3}]\text{O}_2$ ($0 < x < 1/2$) series show similar behavior before, during and following electrochemical cycling[84, 89, 102]. Therefore the results from both computations and experimental characterizations could be combined to understand the structural and electrochemical properties of this material series from various aspects. The

combined results allow us to present an alternative Li de-intercalation mechanism in the Li-excess layered oxides.

There are two distinct regions in the delithiation process. The initial charging region is before the plateau region when the voltage is less than 4.45 V or the amount of Li is greater than 0.8 per formula. The second step is when the voltage is in the plateau region greater than 4.50V and the concentration of Li^+ ions is less than 0.8 per formula. For the convenience of general discussion, $\text{Li}_\delta\text{Ni}_{1/5}\text{Mn}_{3/5}\text{O}_2$ is taken as the example and discussed in following sections.

Initial Stage of Lithium Deintercalation (pre-plateau up to 4.45 V; $0.8 < \delta < 1.2$)

First principles calculations suggest that a solid solution behavior exists in this region of the delithiation process consistent with previous experimental work[89]. The Li is continuously extracted from the material, which is depicted by the electrochemical curve as a sloping region from the open circuit voltage to 4.45V. This region provides 120mAh/g capacity (0.4 Li per formula unit) and the charge compensation originates from the Ni ions which is consistent with previous x-ray absorption spectroscopy results showing that the Ni^{2+} ions are oxidized to Ni^{4+} . [101] Both the Mn^{4+} and O^{2-} valences are not changed during this region. The computation results predict that lithium will migrate into tetrahedral sites. This process is illustrated in Figure 5.12. Initially the Li^+ ions are removed from the Li layer first seen in Figure 5.12a. The energy of removing one Li per cell from Li layer is more than 300meV lower than that from TM layer. The Li ion in the transition metal layer (Li_{TM}) is edge-sharing with three octahedral Li ions (Li_{oct}) in the adjacent Li layer. When these edge-sharing Li_{oct} ions are extracted, a Li^+ ion will migrate from the octahedral site into the tetrahedral site, as shown in Figure 5.12b, face-sharing

with Li in the TM layer. During this process, the Li in the TM layer will migrate to the shared tetrahedral site in the opposite site forming a Li-Li dumbbell (Figure 5.12c) and the total energy of the structure is further reduced. On the other hand, TM ions in the structure may be able to diffuse following similar ways as Li diffusion. Preliminary calculations give the hints that under certain circumstances, Ni^{2+} ($t_{2g}^6 e_g^2$) may migrate from one octahedral site to another adjacent octahedral site through an empty tetrahedral site, with relatively low energy barriers at the beginning of the charge state. Ni ions therefore may diffuse out of the TM layer, diminishing the ordering contrast in the TM layer, and diffuse into the Li layer, increasing the Li/Ni interlayer mixing.

Second Stage of Lithium Deintercalation (plateau up to 4.8V; $0.2 < \delta < 0.8$)

In the electrochemical voltage profile, a plateau region exists between 4.4V and 4.6V indicating a two-phase reaction. As suggested by first principles calculations, during this region, the remaining Li^+ ions in the octahedral sites are extracted from the Li layer, while the tetrahedral Li-Li dumbbells are very stable and need voltages exceeding 5.0V to be removed. Therefore these Li-Li dumbbells may never be removed during the first cycling up to 4.8V, blocking the empty sites in the TM layer, therefore may partially cause the irreversible capacity during the first cycling. EELS spectra of Li edge (Figure 5.7) indicates that the surface has only about half of the Li concentration as the bulk even at the fully discharged state. The tetrahedral Li that remained in the structure combined with the TM ions migrating into the Li layer can facilitate the formation of the proposed spinel-like phase which has an extremely low energy at low lithium concentration region (high voltage region). Such a second phase may be generated near the surface of the material. As the electrochemical impedance data (Figure 5.2) showing that, resistance at

the interface between the surface layer and the pristine particles dramatically increases especially at high voltages. Such resistance increase may partly be due to the generation of the two phase boundary between the bulk materials and the surface phase. As certain amount of TM ions are now in the Li layers near the surface, as shown by *a*-STEM Z-contrast images (Figures 5.4 and 5.5) as well as Rietveld refinement of XRD (Figure 5.3), the original Li diffusion planes are populated with high density of TM ions, and the general Li mobility of the material at high voltage (low lithium concentration) is negatively affected. With this specific surface phase structural change, the materials therefore exhibit inferior rate capabilities. Our first principles data, as well as the synchrotron XRD data suggest the formation of tetrahedral Li; however x-ray diffraction is insensitive to Li ions; therefore, the absolute amount of Li present in the tetrahedral layer is still uncertain. Further evidence using neutron diffraction is necessary and will be discussed in a future publication.

The charge compensation mechanism may originate from the oxygen ions as previously explored with the activation of the Li_2MnO_3 region.[9, 86] Mn-O bonding is weakening due to the change of the oxygen charge densities, resulting Mn-O distortions. Typically Mn^{4+} has t_{2g}^3 electron configuration and MnO_6 octahedrons are highly stable. Such distortion will lead to significant change in the bonding characteristics of Mn-O. EELS observations clearly show that the valence of Mn ions near the surface (about 2-5nm thick) has been reduced from 4+ and oxygen pre-peak diminished. More careful study on the impact of Mn-O distortions and the possibility of oxygen vacancy formations will be helpful.

Based on the combined experimental and computational results presented, we can conclude that permanent changes occur at the surface of the Li excess layered materials during the initial charging cycle. A new defect-spinel solid phase is formed on the surface of the electrode materials after high-voltage cycling. An atomistic model for such a spinel-like phase is proposed for the first time. We believe that such a surface phase transformation may be part of the sources contributing to the first cycle irreversible capacity and the main reason for the intrinsically poor rate capability of these materials. The surface phase developed in this series of materials following electrochemical cycling is 2-5nm thick on the surface making it difficult to identify. Characterization of the surface is equally difficult because the oxygen framework remains the same but changes in the transition metal layers and lithium layers appear. The results from this work required the use of sophisticated techniques such as atomic resolution STEM and EELS with high spatial resolution. The atomic contrast STEM images can be used to identify changes in the stacking and ordering within the material while the EELS analysis complements the STEM results with quantifiable changes. The combination of the two techniques provides strong evidence for the growth of a surface layer on the lithium excess series of materials. Our research findings provide significantly new insights to reasons why the surface coatings of these materials improves the electrochemical properties such as rate capabilities and irreversible capacity losses. The study of the role of surface coatings is underway and the present results reinforce the view that this is an important area for expanded research.

5.5 Conclusion

The series of Li-excess layered oxide compounds $\text{Li}[\text{Ni}_x\text{Li}_{1/3-2x/3}\text{Mn}_{2/3-x/3}]\text{O}_2$ ($0 < x < 1/2$) are investigated in a joint study combining both computational and experimental methods. From first principles calculation, a new lithium de-intercalation mechanism is proposed where stable tetrahedral lithium ions are formed during the early charging stage and may not be able to be extracted before 5V. The Rietveld refinement results from XRD of pristine and cycled samples further confirm that the tetrahedral lithium ions are involved in the cycled samples accompanied by an increase in Li-Ni interlayer mixing. The Z-contrast high-resolution TEM also provide the evidence of surface transition metal ions migrating into the lithium layer, which may affect the transition metal – oxygen bonding characteristics as indicated in the EELS results. Such surface structural change may lead to a phase transformation from layered structure to defect-spinel structure at the surface of the materials. The large irreversible capacity after cycling and the low rate capability of the materials are therefore partially attributed to this surface phase transformation.

Chapter 5, in full, is a reprint of the material "Identifying Surface Structural Changes in Layered Li-excess Nickel Manganese Oxides in High Voltage Lithium Ion Batteries: A Joint Experimental and Theoretical Study", as it appears in *Energy & Environmental Science*, 4(6), 2011. Bo Xu, C. R. Fell, M. Chi, Ying S. Meng, 2011. The dissertation author was the primary investigator and author of this paper.

Figures:

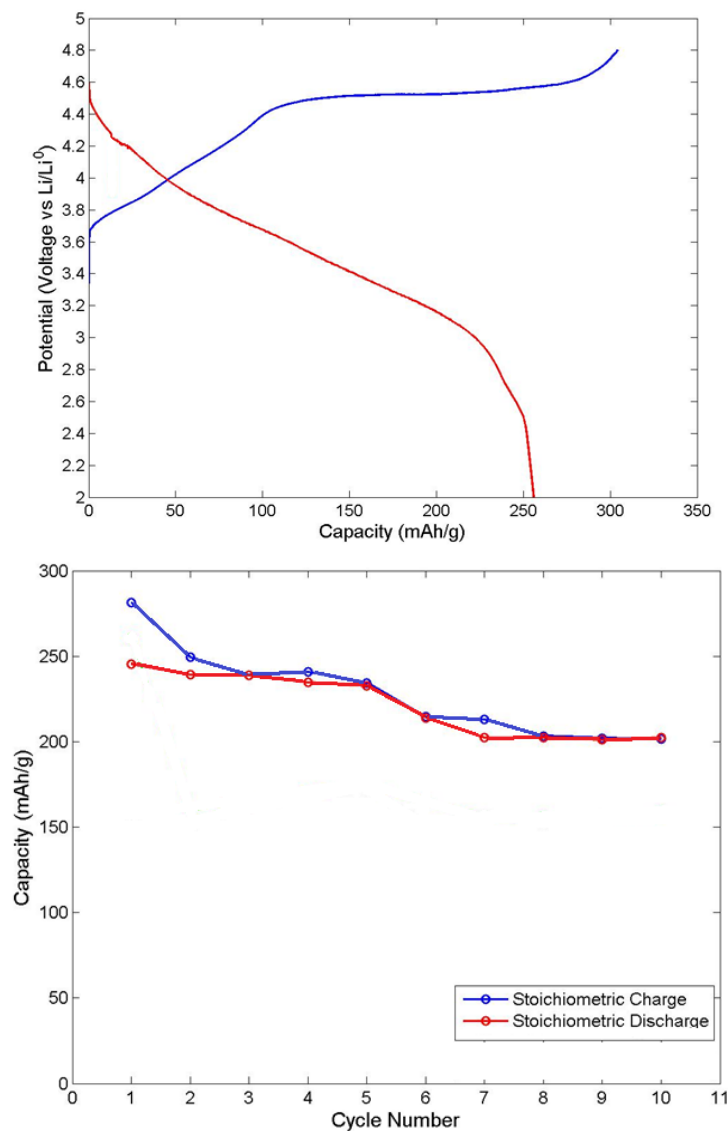


Figure 5.1 (a) Electrochemical profile of $\text{Li}[\text{Ni}_x\text{Li}_{1/3-2x/3}\text{Mn}_{2/3-x/3}]\text{O}_2$ ($x=1/5$) with a C/50 rate. A voltage window of 4.8 – 2.0 V was used (b) Capacity versus electrochemical cycle of $\text{Li}[\text{Ni}_{1/5}\text{Li}_{1/5}\text{Mn}_{3/5}]\text{O}_2$. The first 5 cycles correspond to a C/50 rate and cycles 6-10 correspond to a C/20 rate

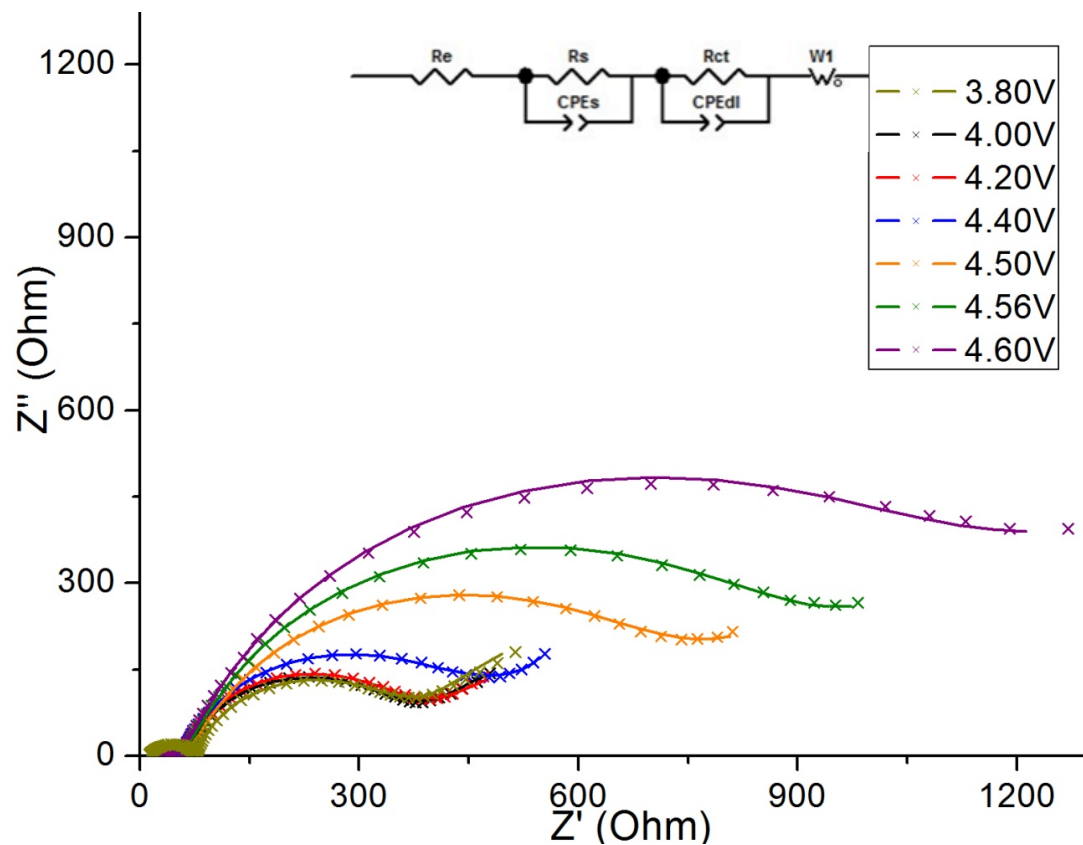


Figure 5.2 Experimental observations (marked by X) of electrochemical impedance spectroscopy (EIS) of $\text{Li}[\text{Ni}_{1/5}\text{Li}_{1/5}\text{Mn}_{3/5}]\text{O}_2$ during the first electrochemical charging cycle at different states of charge (SOC). The equivalent circuit model in the inset was used to fit the experimental model and plotted as a line at different SOC.

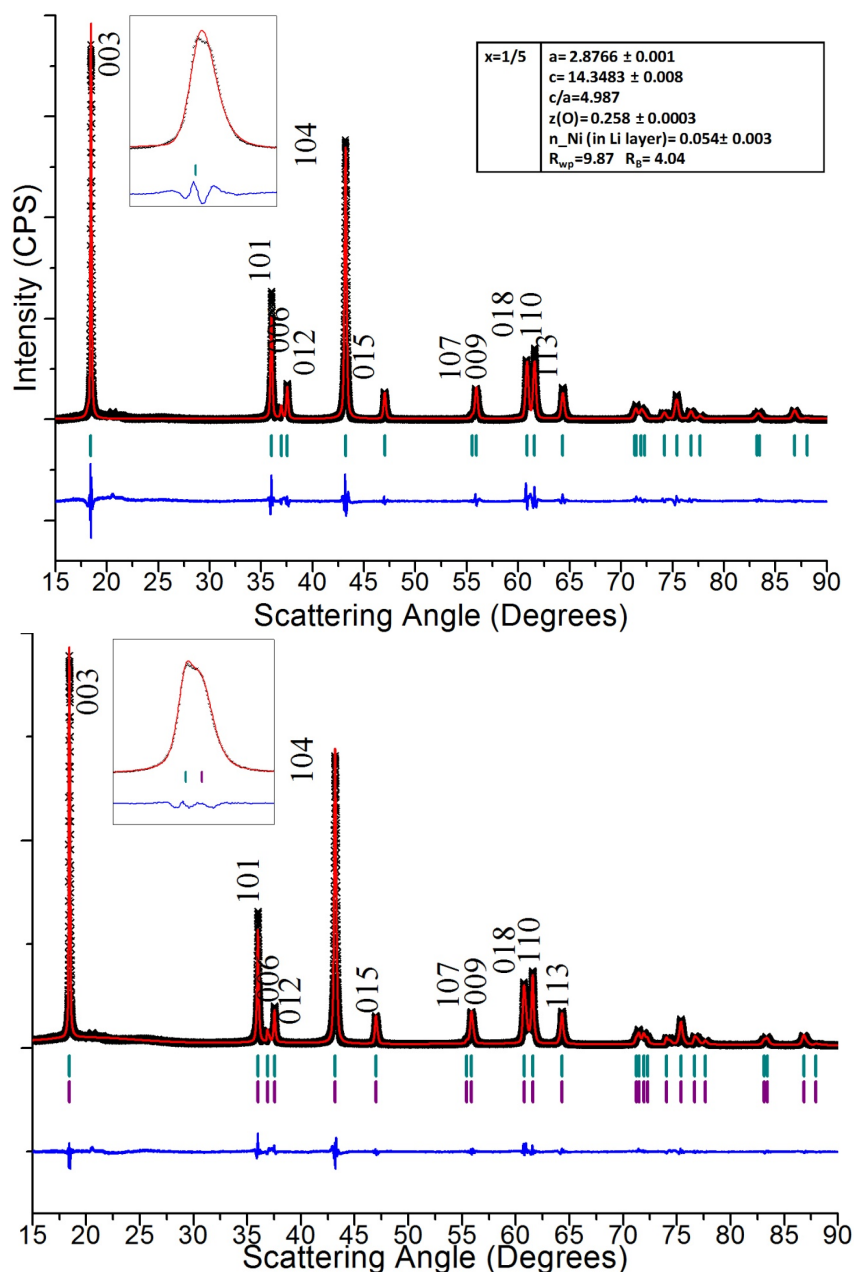


Figure 5.3 High resolution synchrotron X-ray diffraction pattern of discharged $\text{Li}[\text{Ni}_{1/5}\text{Li}_{1/5}\text{Mn}_{3/5}]\text{O}_2$ following 10 electrochemical cycles. Rietveld Refinement of 3a) one $R\bar{3}m$ phase and 3b) two $R\bar{3}m$ phases. The black crosses represent the observed pattern, the red line corresponds to the calculated diffraction pattern and the blue is the difference pattern. The teal lines correspond to peak positions from the $R\bar{3}m$ space group. In this and subsequent figures, the 2θ values are converted to those corresponding to a Cu $K\alpha$ wavelength ($\lambda=1.54 \text{ \AA}$)

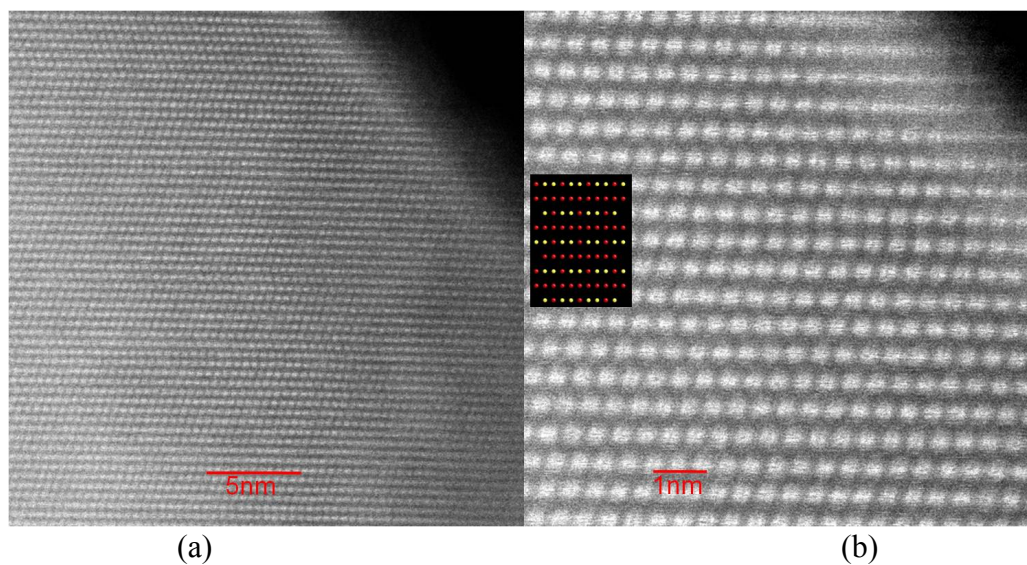


Figure 5.4 High resolution S/TEM images of the bulk and surface of pristine $\text{Li}[\text{Ni}_{1/5}\text{Li}_{1/5}\text{Mn}_{3/5}]\text{O}_2$ at low magnification (a) and high magnification (b) taken along $[100]$. The insert in (b) is a schematic representation of the Li ions (red) and transition metal ions (yellow) showing the cation ordering and stacking along the c_{hex} axis.

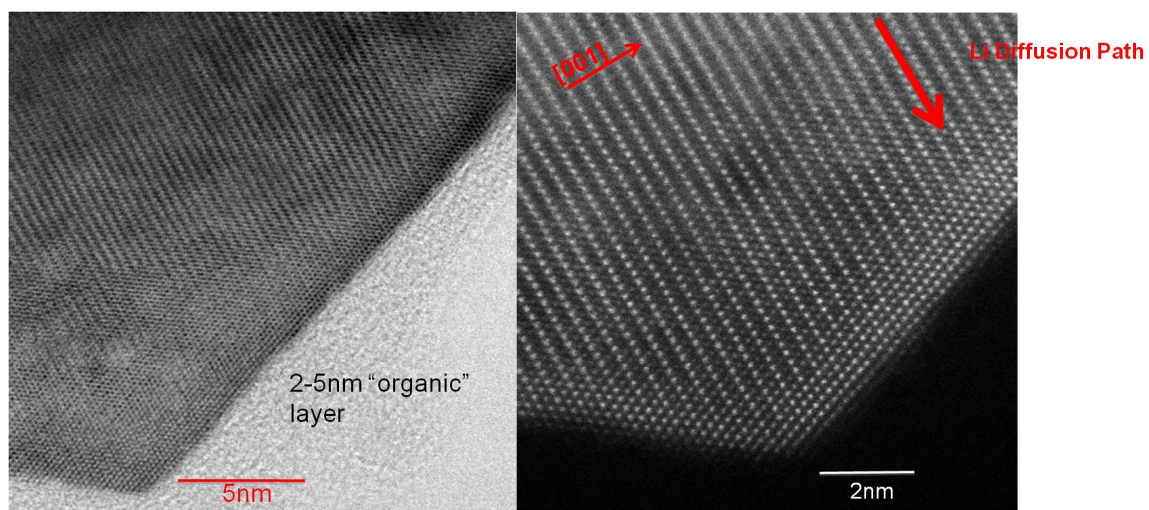


Figure 5.5 High resolution S/TEM image (a) and corresponding HAADF image (b) of the bulk and surface regions of electrochemically cycled $\text{Li}[\text{Ni}_{1/5}\text{Li}_{1/5}\text{Mn}_{3/5}]\text{O}_2$ taken along the $[110]$ $[10\bar{1}0]$ zone axis.

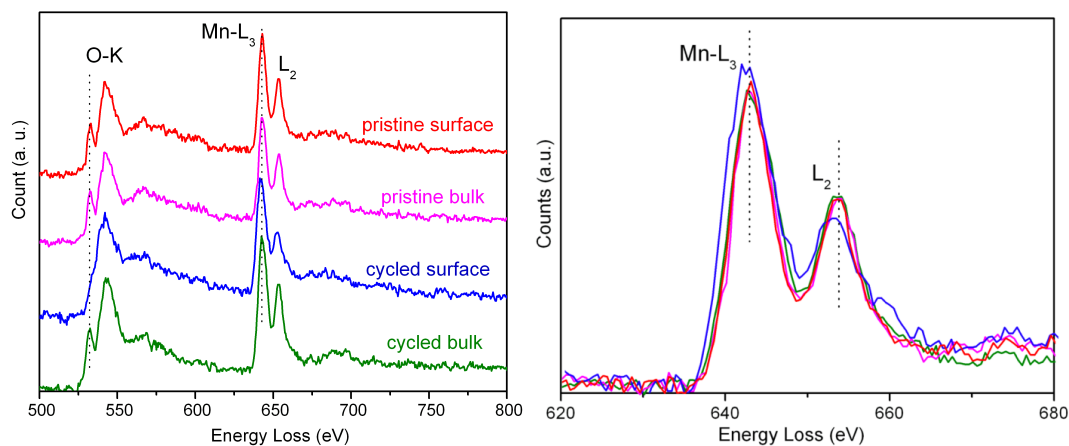


Figure 5.6 Representative EELS spectra of the (a) O K-edge and (a & b) Mn L-edge from the surface and bulk of the pristine and electrochemically cycled $\text{Li}[\text{Ni}_{1/5}\text{Li}_{1/5}\text{Mn}_{3/5}]\text{O}_2$ material.

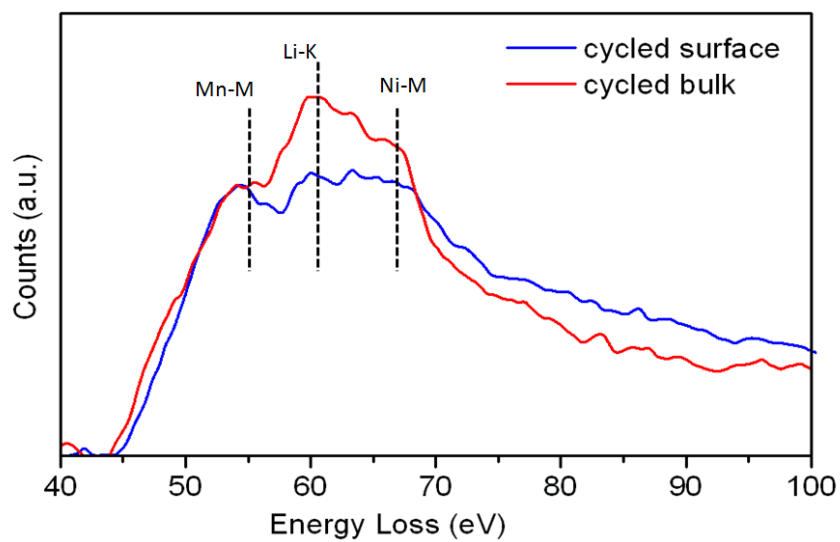


Figure 5.7 Comparison of Li-K edges from the surface and bulk in the cycled material. Obvious Li signal drop was observed on the spectrum from the surface area compared to that from bulk, although Li-K edge overlaps TM-M edges. Dotted lines mark the main peak position of Li-K and TM-M edges.

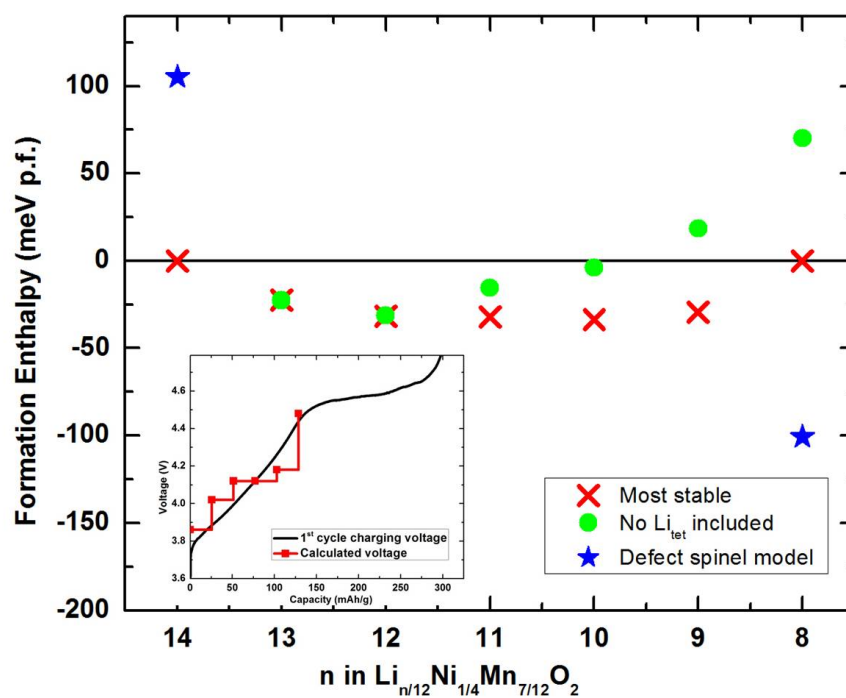
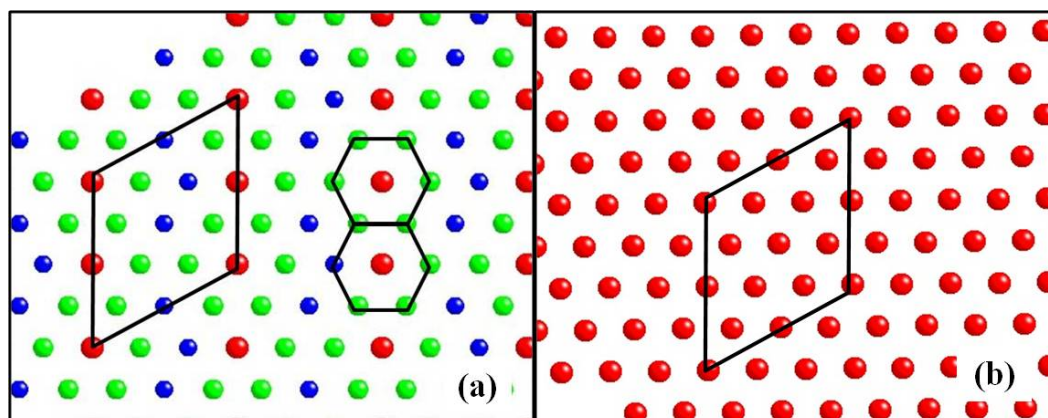


Figure 5.8 a and b The cation in-plane ordering of different models of $\text{Li}[\text{Ni}_{1/4}\text{Li}_{1/6}\text{Mn}_{7/12}]\text{O}_2$ (Red: Li; Green: Mn; Blue: Ni) Figure 5.8c Calculated voltage and formation enthalpy of $\text{Li}_{x/14}\text{Ni}_{1/4}\text{Mn}_{7/12}\text{O}_2$ ($8 < x < 14$) versus lithium concentration

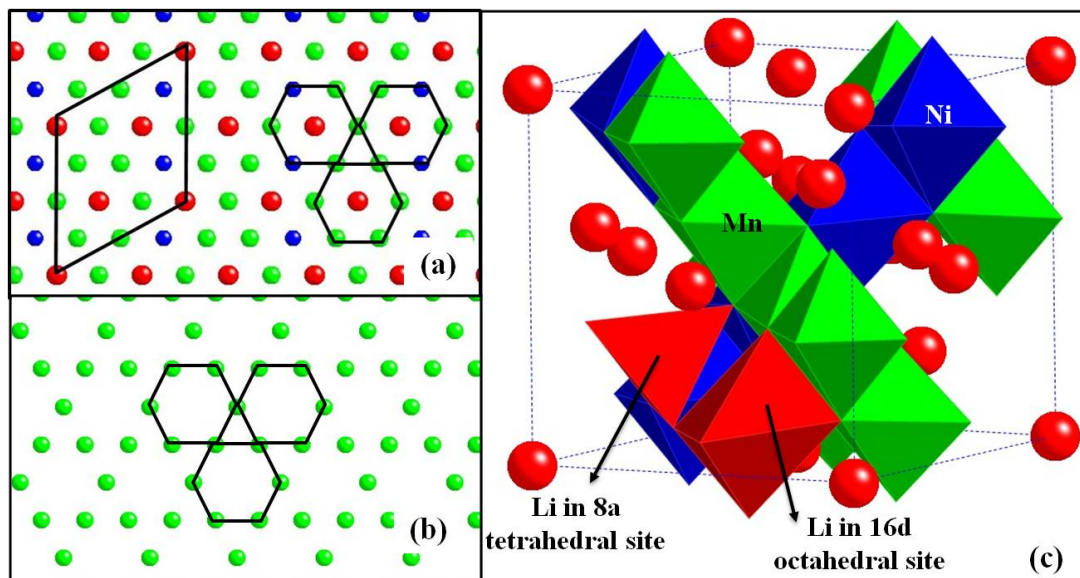


Figure 5.9 The defect-spinel model of $\text{Li}[\text{Ni}_{1/4}\text{Li}_{1/6}\text{Mn}_{7/12}]\text{O}_2$ and $\text{Li}[\text{Li}_{1/3}\text{Ni}_{1/2}\text{Mn}_{7/6}]\text{O}_4$

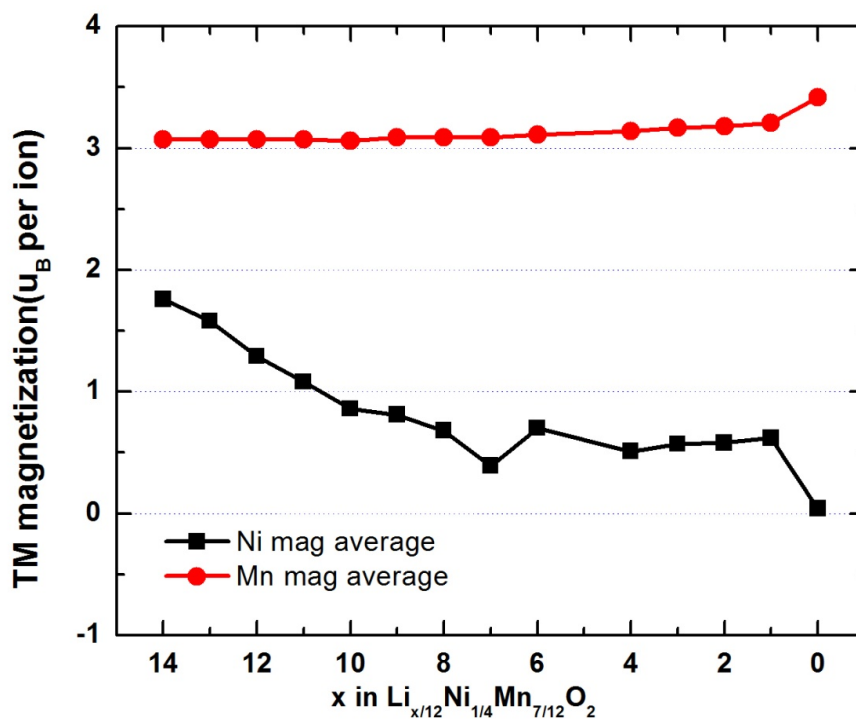


Figure 5.10 Calculated magnetization of Ni and Mn ions versus lithium concentration

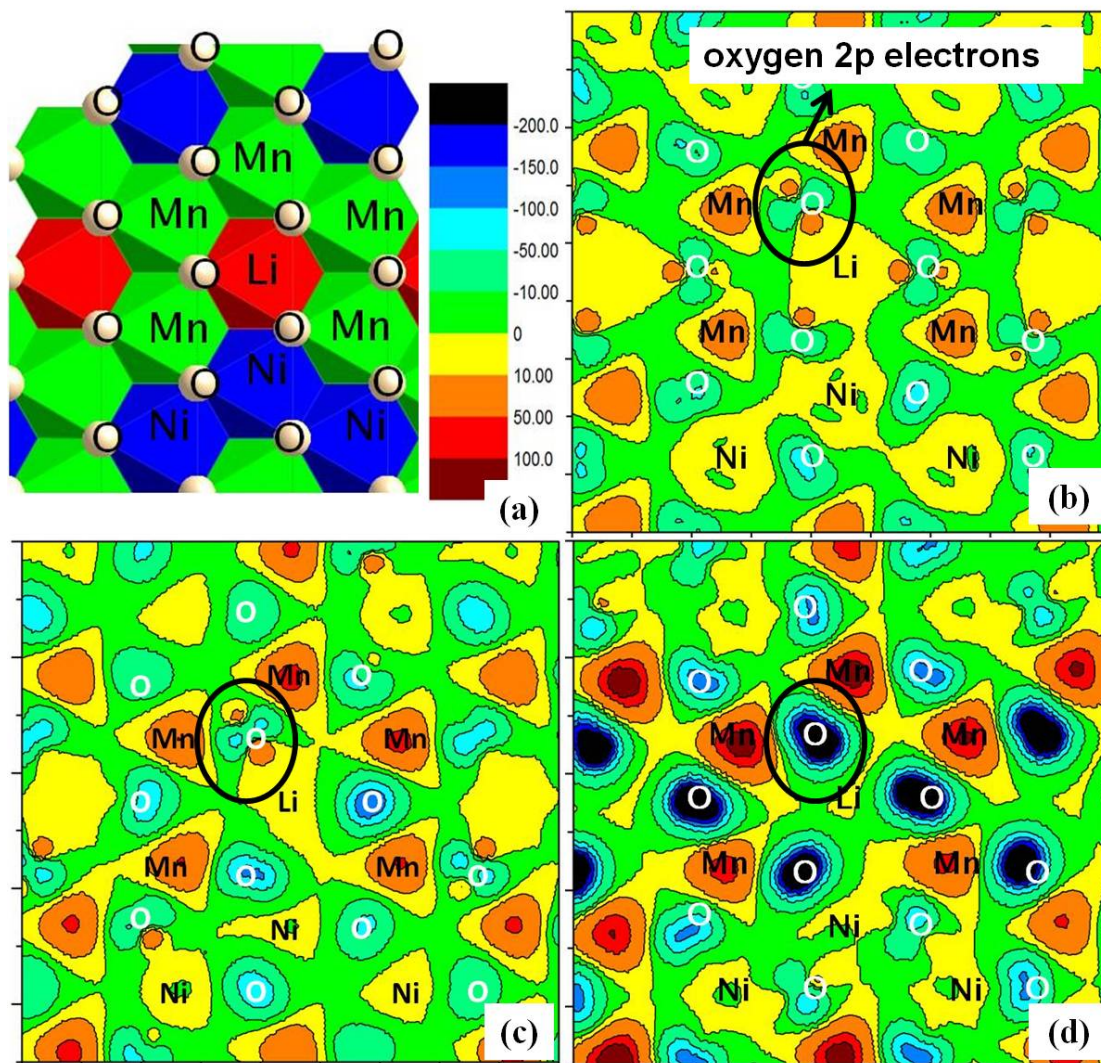


Figure 5.11 The calculated spin density (difference between spin-up and spin-down) of part of the TM layer at $\text{Li}_{x/14}\text{Ni}_{1/4}\text{Mn}_{7/12}\text{O}_2$ (b) $x=14$ (c) $x=8$ (d) $x=0$.

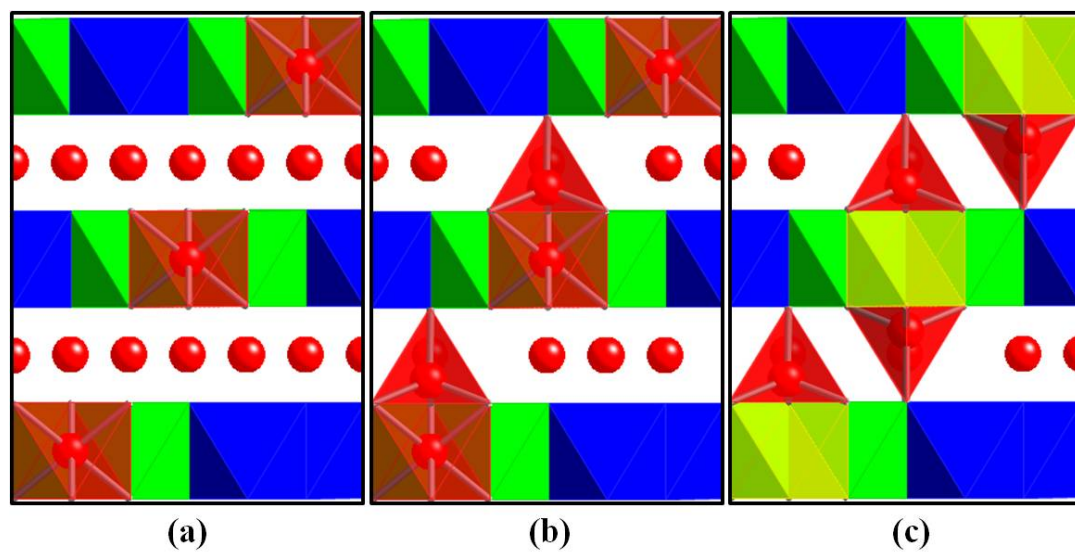


Figure 5.12 Sketch of Li-Li dumbbell formation (Red:Li; Green:Mn; Blue:Ni; Yellow: Vacancy)

Tables:

Table 5.1 Fitting parameters for the equivalent circuit model represented in Fig. 2 applied to the electrochemical impedance (EIS) curves recorded between 3.80 V and 4.60 V

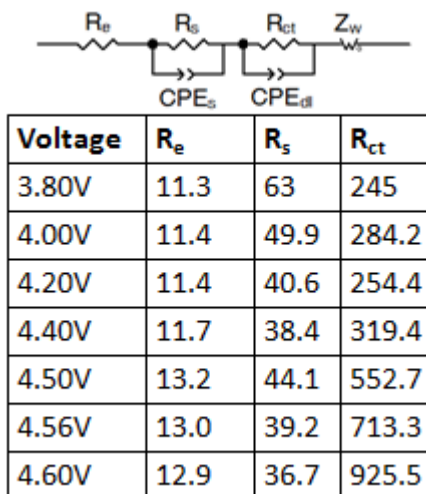


Table 5.2 Two phase Rietveld refinement results for discharged $\text{Li}[\text{Ni}_{1/5}\text{Li}_{1/5}\text{Mn}_{3/5}]\text{O}_2$ following 10 electrochemical cycles using two $R\bar{3}m$ $R\bar{3}m$ phases

$a_{\text{hex}}: 2.8758\text{\AA}$ $c_{\text{hex}}: 14.3750$ $c/a: 4.999$ $R\bar{3}m$						$a_{\text{hex}}: 2.8763\text{\AA}$ $c_{\text{hex}}: 14.3225$ $c/a: 4.979$ $R\bar{3}m$					
Atom	Site	Wyckoff Positions			Occupancy	Atom	Site	Wyckoff Positions			Occupancy
Ni1	3a	0	0	0	0.104	Ni1	3a	0	0	0	0.178
Ni2	3b	0	0	0.5	0.096	Ni2	3b	0	0	0.5	0.022
Mn1	3a	0	0	0	0.600	Mn1	3a	0	0	0	0.600
Li2	3b	0	0	0.5	0.696	Li2	3b	0	0	0.5	0.771
Li1	3a	0	0	0	0.104	Li1	3a	0	0	0	0.029
O	6c	0	0	0.258(3)	2	O	6c	0	0	0.258(3)	2

Conventional Rietveld Reliability Factors: R_{wp} : 7.33 R_b : 4.04

Table 5.3 Two phase Rietveld refinement results for discharged $\text{Li}[\text{Ni}_{1/5}\text{Li}_{1/5}\text{Mn}_{3/5}]\text{O}_2$ following 10 electrochemical cycles including one phase with Li on the $(1/3, 2/3, z)$ tetrahedral site

$a_{\text{hex}}: 2.8760\text{\AA}$ $c_{\text{hex}}: 14.3757$ $c/a: 4.999$						$a_{\text{hex}}: 2.8766\text{\AA}$ $c_{\text{hex}}: 14.3234\text{\AA}$ $c/a: 4.979$					
Atom	Site	Wyckoff Positions			Occupancy	Atom	Site	Wyckoff Positions			Occupancy
Ni1	3a	0	0	0	0.121	Ni1	3a	0	0	0	0.151
Ni2	3b	0	0	0.5	0.079	Ni2	3b	0	0	0.5	0.047
Mn1	3a	0	0	0	0.600	Mn1	3a	0	0	0	0.600
Li2	3b	0	0	0.5	0.721	Li2	3b	0	0	0	0.618
Li1	3a	0	0	0	0.079	Li1	3a	0	0	0.5	0.047
O	6c	0	0	0.257(3)	2	Li _{Tet}	4i	1/3	2/3	0.7986	0.135
						O	6c	0	0	0.2582	2

Conventional Rietveld Reliability Factors: $R_{\text{wp}}: 7.12$ $R_b: 3.68$

6 FIRST PRINCIPLES STUDY OF THE ROLES OF OXYGEN VACANCY ON CATION MIGRATION IN LITHIUM EXCESS NICKEL MANGANESE OXIDES

As a following step for previous work on $\text{Li}_x\text{Ni}_{1/4}\text{Mn}_{7/12}\text{O}_2$ bulk, the mechanism of oxygen vacancy formation is investigated in this chapter using first principles calculations. The oxygen vacancy formation energy trend versus Li concentration is obtained, as well as the Ni diffusion barriers with oxygen vacancies appear at different positions. The oxygen vacancy assisted Ni migration mechanism is proposed and explained in this chapter as well. The details of the computational parameters are similar to that in chapter 5. NEB method is used to calculate the Ni diffusion barriers.

6.1 Formation energy of oxygen vacancy in $\text{Li}_x\text{Ni}_{1/4}\text{Mn}_{7/12}\text{O}_2$ bulk

In this work, two types of supercells were used for investigations and only one vacancy is created in each cell. This is equivalent to oxygen vacancy concentration of 2% to 4% which is very close to the experimentally estimated valued. Therefore the following two equations were used to calculate the formation energy of oxygen vacancies in $\text{Li}_x\text{Ni}_{1/4}\text{Mn}_{7/12}\text{O}_2$:

$$E_{fov} = E(\text{Li}_n\text{Ni}_3\text{Mn}_7\text{O}_{23}) + 1/2 E(\text{O}_2) - E(\text{Li}_n\text{Ni}_3\text{Mn}_7\text{O}_{24}) \quad 6-1$$

and

$$E_{fov} = E(\text{Li}_m\text{Ni}_6\text{Mn}_{14}\text{O}_{47}) + 1/2 E(\text{O}_2) - E(\text{Li}_m\text{Ni}_6\text{Mn}_{14}\text{O}_{48}) \quad 6-2$$

where $E(\text{O}_2)$ is the calculated energy of the oxygen gas plus a 1.36 eV correction according to previous reports (ref). The oxygen vacancies were created using previous reported ground states configurations of $\text{Li}_x\text{Ni}_{1/4}\text{Mn}_{7/12}\text{O}_2$ (ref.). The atom arrangements

of the transition metal layer and the adjacent oxygen layer in $\text{Li}[\text{Li}_{1/6}\text{Ni}_{1/4}\text{Mn}_{7/12}]\text{O}_2$ ground state are shown in Figure 6.1. As depicted in the inset of Figure 6.1, each oxygen ion is bonded with 6 nearest cations. Three of them are Li ions in lithium layer and the other three in transition metal (TM) layer can be Li, Ni or Mn. There are four different combinations of the three cations in TM layer. These configurations are indicated by black circles in Figure 6.1 and noted by *a*, *b*, *c* and *d*. Oxygen vacancies can be located in these different local atomic configurations with different lithium concentrations. More than 70 different configurations were performed over the lithium concentration between 28/28 and 14/28, which is the range of the sloppy region of the first cycle charging voltage. The calculated oxygen vacancy formation energies versus lithium concentrations are shown in Figure 6.2. It shows a general trend that oxygen vacancy formation energy (E_{fov}) decreases when lithium concentration increases. E_{fov} decreases sharply from Li concentration 14/14 to 10/14, after which, E_{fov} drops to less than 1eV and becomes relatively stable. Note that at Li concentration 10/14, the tetrahedral Li-Li dumbbells begin to form. Low E_{fov} are usually reached in configuration *d* while the high E_{fov} are usually reached in configuration *a*. The E_{fov} of configuration *c* have a large range in value over all lithium concentrations. Note that all calculations are performed in the bulk of the materials, therefore no oxygen diffusion is considered at this step. The results suggest that even in the bulk of material, oxygen vacancies may be generated at room temperature at lower lithium concentrations. Referring to the local atomic environments, oxygen vacancies are less likely to form near the configuration with Ni and Mn ions only, and more likely to form near the configuration of Li, Ni and Mn ions. Since at lower Li concentrations, the Li ions in the TM layers will migrate to the adjacent tetrahedral sites,

the formed oxygen vacancies therefore are also near the generated Li-Li dumbbells. This observation can be partially explained by electrostatic effect. As in the metal oxides, the oxygen vacancies exhibit positive charges therefore may more likely to be stable near the cations with less positive charges to balance the overall charge distribution. Comparing to the vacancy-free materials with same atomic configurations, the transition metal ions nearest to the oxygen vacancy will be reduced in valence. If Ni ions are included in the nearest cations, they prefer to be reduced first. Therefore with oxygen vacancies exist, Ni^{2+} and Ni^{3+} ions may still present even in lower Li concentration such as 7/14. Comparing to Ni^{4+} ions which are very stable within octahedral coordination, these Ni^{2+} and Ni^{3+} can be more mobile. As a subsequent step, Ni diffusion barriers of Ni^{2+} ions in different lithium concentrations and oxygen vacancy configurations are investigated and reported in the next section.

6.2 Ni diffusion in $\text{Li}_x\text{Ni}_{1/4}\text{Mn}_{7/12}\text{O}_2$ bulk

It has been reported that in the layered materials, the transition state theory can be adopted to describe the diffusion of cations in the materials. This theory is also adopted in this work to describe the Ni migration mechanism as demonstrated in Figure 6.3. In $\text{Li}_x\text{Ni}_{1/4}\text{Mn}_{7/12}\text{O}_2$, Ni is located originally in the octahedral site in TM layer. An empty tetrahedral site in Li layer is face-sharing with the Ni octahedron. The shared-face is composed of three oxygen ions forming a triangular oxygen plane. When the three Li ions near the empty tetrahedral site are extracted, the Ni ion may be able to migrate from the octahedral site to the empty tetrahedral site through the shared oxygen plane and then migrate to another octahedral site. However, different from Li ion diffusion, the electron

density of Ni ions is much denser therefore the columbic interactions between Ni electrons and O electrons are much stronger when Ni ions move through the oxygen plane. Results from NEB calculations showed that the Ni diffusion barrier should be considered as the energy difference between Ni in the centered of the oxygen plane and Ni in the initial octahedral state.

As the first step, Ni diffusion from initial octahedral site in TM layer to the nearest tetrahedral site in Li layer at three different Li concentrations were investigated in this work: 1) At $\text{Li}_{25/28}\text{Ni}_{1/4}\text{Mn}_{7/12}\text{O}_2$ where there are no tetrahedral Li ions present in the structure; 2) At $\text{Li}_{20/28}\text{Ni}_{1/4}\text{Mn}_{7/12}\text{O}_2$ where there is only one Li-Li tetrahedral dumbbell present in the cell and 3) At $\text{Li}_{15/28}\text{Ni}_{1/4}\text{Mn}_{7/12}\text{O}_2$ where there are two Li-Li tetrahedral dumbbells present in the cell. In each concentration, the migrating Ni ions are Ni^{2+} ions that are expected to have higher mobilities than Ni^{3+} and Ni^{4+} ions. Oxygen vacancies are located at three different positions in the Ni polyhedral site (shown in the footnote of Figure 6.5-6.7): in the shared oxygen plane between octahedral site and tetrahedral site; in the octahedral vertex but not in the shared oxygen plane; and in the tetrahedral vertex but not in the shared oxygen plane. The oxygen vacancy formation energies of initial states (Ni in octahedral sites) are shown in Figure 6.4 by black crosses. Values of E_{fov} of different initial configurations lie in a wide range at each Li concentration. In Figure 6.5, 6 and 7, the calculated energy tracks along Ni diffusion paths in each lithium concentration are summarized respectively. Although the exact values of Ni diffusion barriers are different for different configurations, the trend is consistent over all Li concentrations and it is clear that the positions of oxygen vacancies have significant impact on the Ni diffusion barriers. When the vacancy appears in the shared oxygen

plane, Ni ions are slightly more stable in the octahedral sites than in tetrahedral sites. Although with one vacancy in the shared oxygen plane the oxygen electron charge density may be less dense, the Ni diffusion barriers are around 1eV over all three Li concentrations, which are still similar to the barriers without oxygen vacancies. When the vacancy appears at one of the octahedral vertexes but not in the shared oxygen plane, Ni in the five-coordinated octahedral site will be much more unstable than in the regular tetrahedral site. Ni diffusion barriers are reduced to as low as 0.2 eV to 0.5 eV. The results suggest that in these situations, Ni²⁺ ions may easily diffuse to the nearby tetrahedral site at room temperature. On the other hand, when the vacancy appears at the tetrahedral vertex which is not in the shared oxygen plane, the three-coordinated tetrahedral site becomes unstable and the Ni diffusion barriers increase to around 2 eV. The inset of each figure shows the relations of Ni diffusion barriers with the corresponding oxygen vacancy formation energy when Ni is at the initial octahedral sites. There may be a trend that Ni diffusion barrier decreases when oxygen vacancy formation energy increases, but a few exceptions exist.

As a summary of the above, a possible mechanism of the oxygen vacancies assisting Ni diffusion in the bulk materials can be proposed as following: while an oxygen vacancy is generated in the a Ni octahedron, Ni becomes much unstable in this five-coordinated octahedral site and could migrate to the face-shared regular tetrahedral site with low diffusion barriers. In fact, this mechanism could be further applied to the diffusion of Ni ions at the particle surfaces, as these Ni ions may be naturally five (or even less) coordinated due to the broken bonds on the particle surfaces. These surface Ni ions therefore may easily migrate from TM layer to Li layer surface toward the bulk (I

don't think it is appropriate to say anything about surface vs. bulk – I will polish this part later) of the materials as the experimental observations in our previous reports.

6.3 Conclusion

In this work, a preliminary work has been performed to investigate the possibility of oxygen vacancy formation in the lithium excess nickel manganese layered material bulk. Formation of oxygen vacancies in the materials is possible during the charging process in room temperature. These vacancies are more likely to be generated near the Li-Li tetrahedral dumbbells, in another word the defect spinel regions, and will affect the site stability of transition metal ions such as Ni. Ni diffusion barriers may be highly reduced due to these vacancies. This mechanism may also explain the migration of surface transition metal ions of this material during the first electrochemical cycling as reported in previous work.

Chapter 6, in full, is currently being prepared for submission for publication of the material. Bo Xu, Ying S. Meng, 2012. The dissertation author was the primary investigator and author of this paper.

Figures:

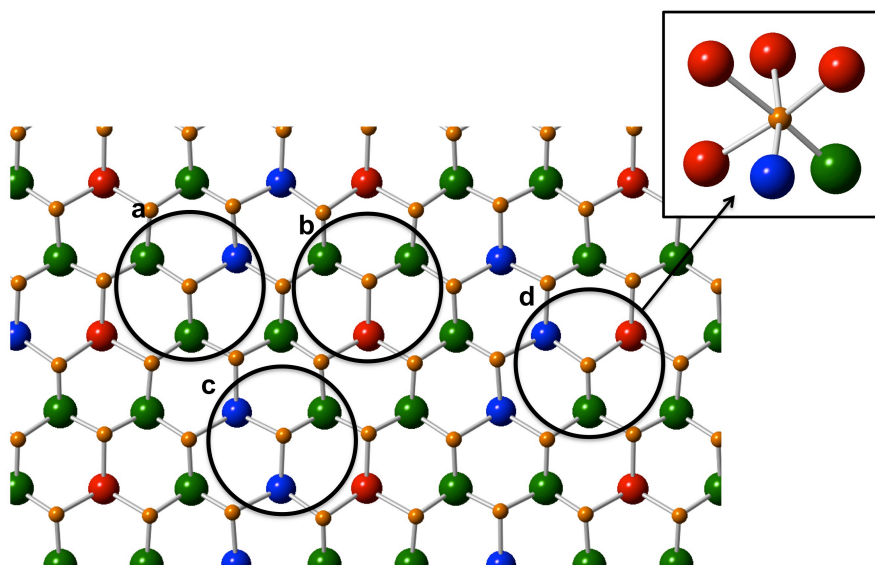


Figure 6.1 Atom configurations of $\text{Li}[\text{Li}_{1/6}\text{Ni}_{1/4}\text{Mn}_{7/12}]\text{O}_2$ (Red: Li; Green: Mn; Blue: Ni; Orange: O)

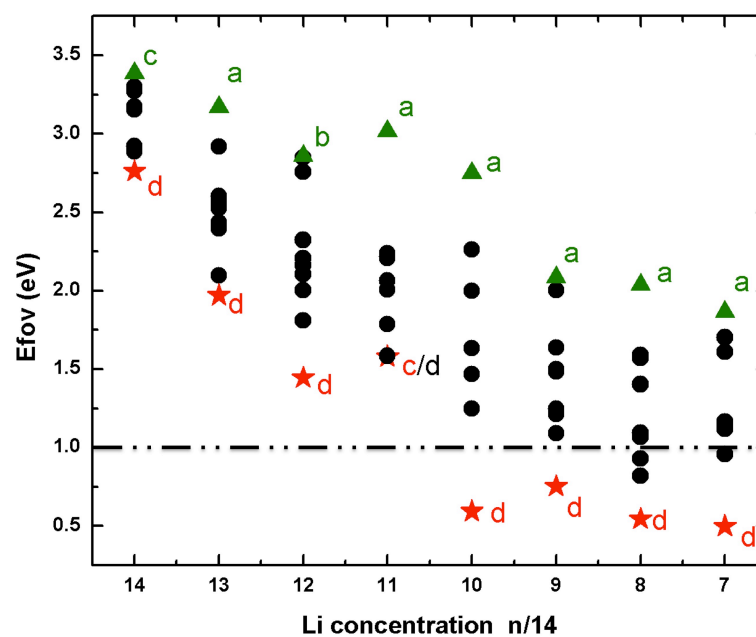


Figure 6.2 Oxygen vacancy formation energy vs. Li concentration

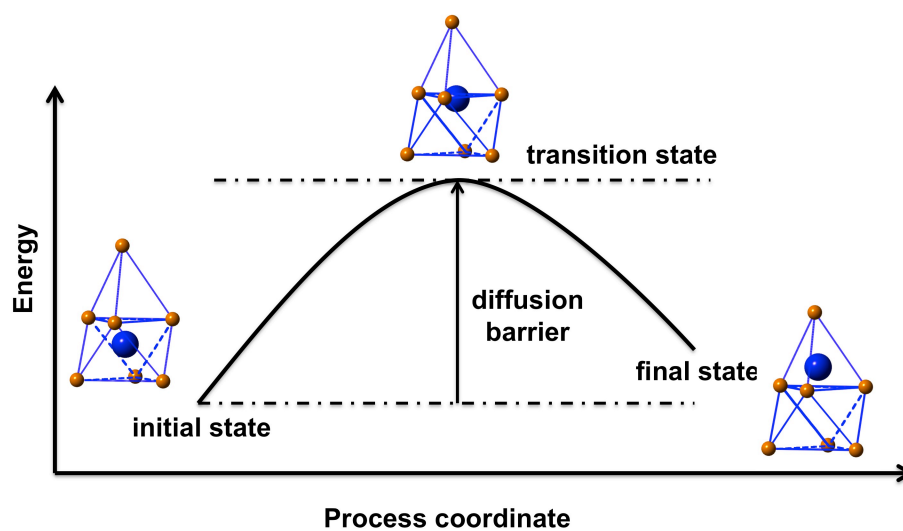


Figure 6.3 Demonstration of transition state theory and Ni diffusion mechanism

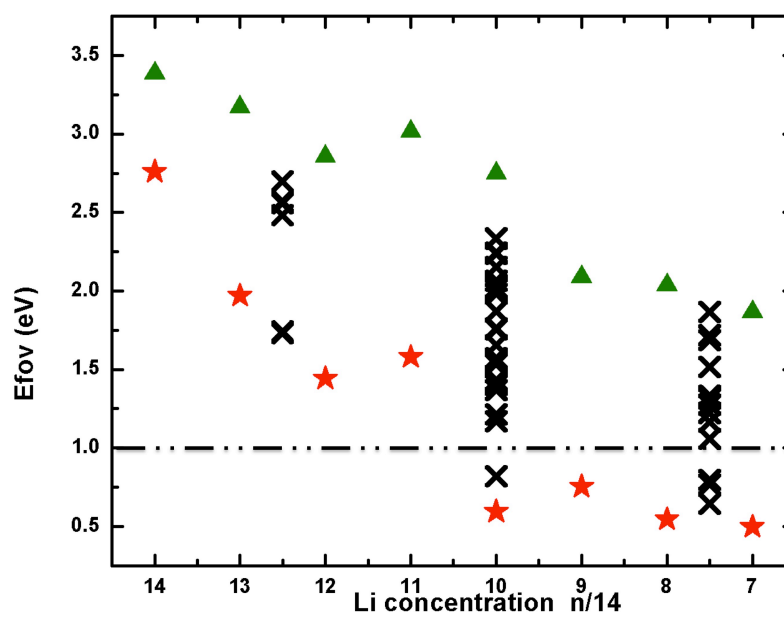


Figure 6.4 Oxygen vacancy formation energy of initial states for Ni migration

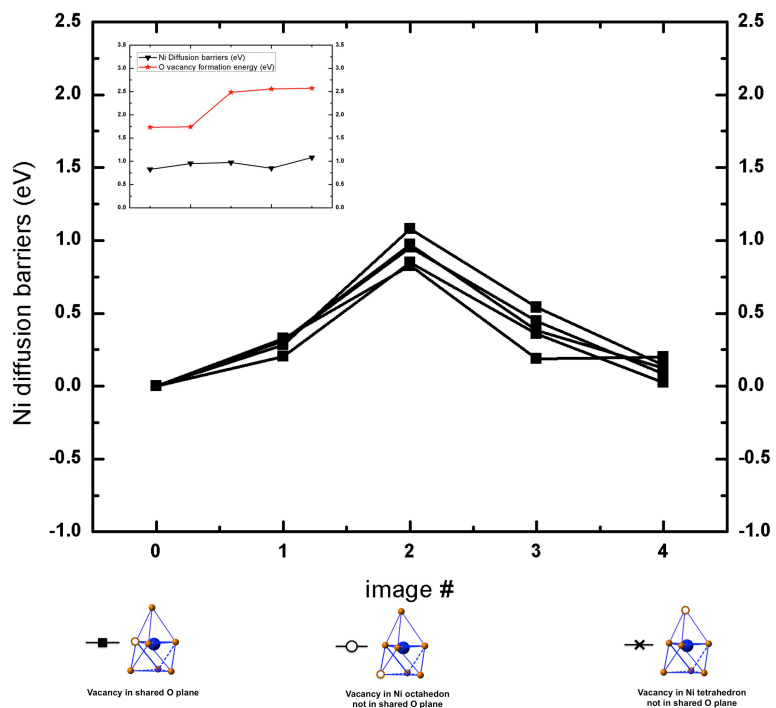


Figure 6.5 Ni diffusion barriers at Li concentration 25/28

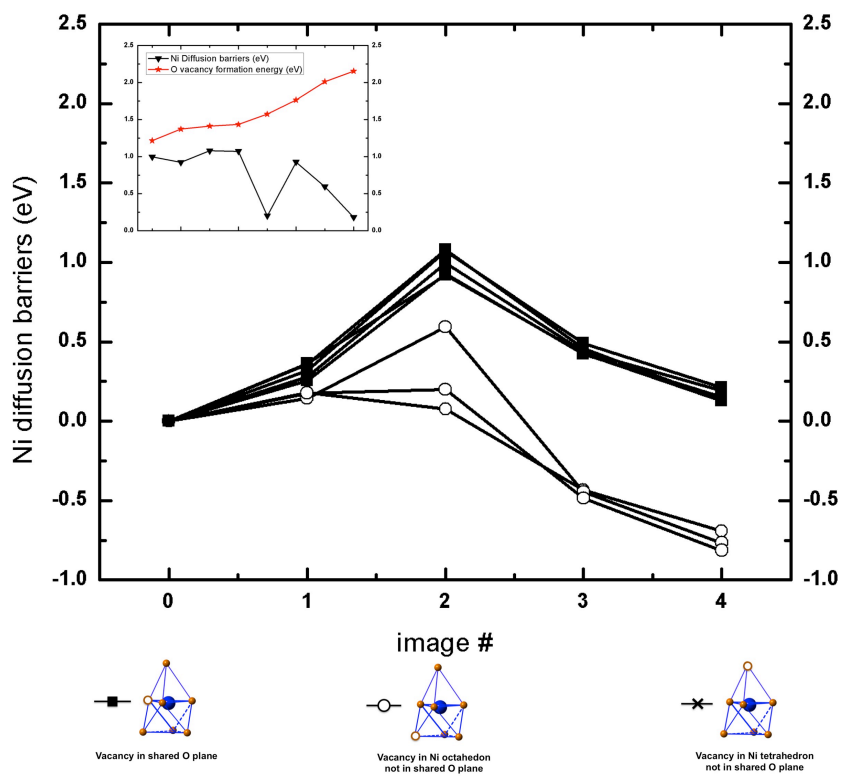


Figure 6.6 Ni diffusion barriers at Li concentration 20/28

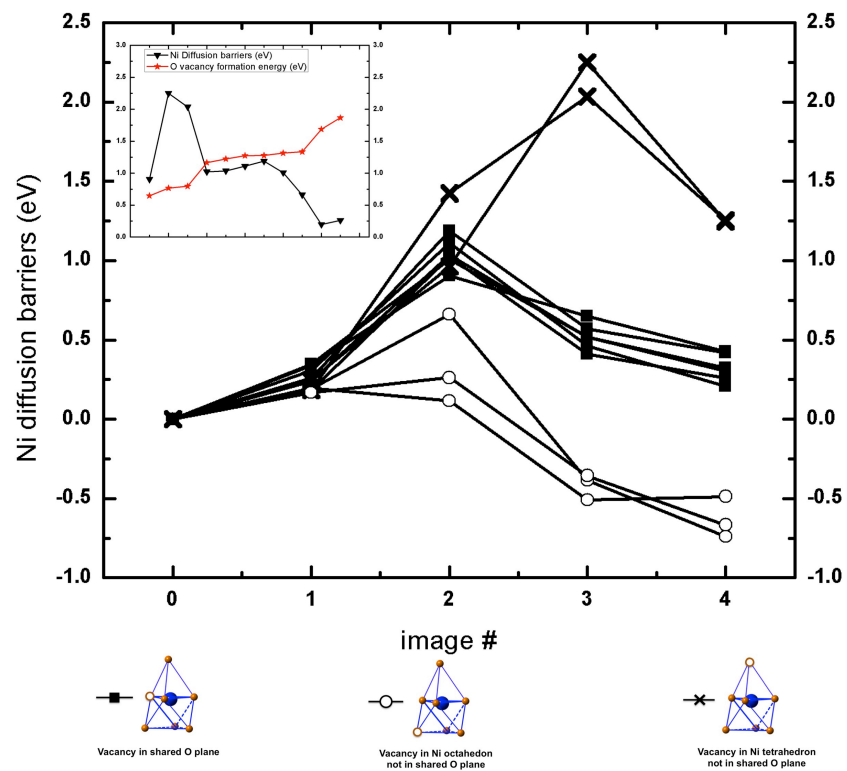


Figure 6.7 Ni diffusion barriers at Li concentration 15/28

7 SUMMARY AND FUTURE WORK

7.1 Summary

In this research, first principles computation is used as the guiding method to improve and develop the high energy high power cathode materials for LIB system. In the first part, the methodology of using first principles computational method to simulate the thermodynamic properties of Li intercalation materials is described in Chapter 3. Using LiMn_2O_4 as the sample material, simulated properties are compared with related experimental properties. Trends of properties including voltages and lattice parameters are very consistent between computational and experimental results. The established computational methodology therefore is confirmed and used to investigate the effect of local Mn charge orderings on Li diffusion barriers. In Chapter 4, the above methodology is adopted to pre-screen the candidate doping elements for the series of doped spinel materials. For doped spinel $\text{LiM}_{0.5}\text{Mn}_{1.5}\text{O}_4$, the voltages and Li diffusion barriers are calculated with different dopant M where M is chosen from the first-row transition metal ions. Based on the calculated results, Cu dopant will maintain the high voltage ($>4.7\text{V}$) while significantly reduce the Li diffusion barriers and improve the material rate performance. Although it is also shown by computation that Cu^{3+} can not be oxidized to Cu^{4+} therefore will reduce the material reversible capacity. This problem, however, can be solved by doping small amount of Cu into $\text{LiNi}_{0.5}\text{Mn}_{1.5}\text{O}_4$ so that the high reversible capacity of spinel materials can still be retained while the rate performance can be improved as well. A new type of bi-doped spinel $\text{LiNi}_x\text{Cu}_y\text{Mn}_{2-x-y}\text{O}_4$ ($0 < x < 0.5$, $0 < y < 0.5$) is proposed as the potential high capacity high rate cathode candidate. This series of

materials are synthesized and characterized by collaborators in University of Florida and the improvements of their rate performances are confirmed.

In the second part, a thorough study of the Li de-intercalation mechanism of Li-excess transition metal oxide $\text{Li}[\text{Ni}_x\text{Li}_{1/3-2x/3}\text{Mn}_{2/3-x/3}]\text{O}_2$ is performed to explore the sources of the anonymous high voltage plateau and the reasons of the material surface structural change after cycling as observed but cannot be explained in experiments. $\text{Li}[\text{Li}_{1/6}\text{Ni}_{1/4}\text{Mn}_{7/12}]\text{O}_2$ is chosen as the sample, and an atomic model is proposed and verified in Chapter 5. In the next step, phase stabilities of $\text{Li}_x\text{Ni}_{1/4}\text{Mn}_{7/12}\text{O}_2$ with different Li concentrations are calculated, and the results suggest that a layer to spinel phase transformation, in which transition metal ion migrations are involved, is possible to happen when Li concentration drops below certain level. It also suggests possible formation of oxygen vacancies at lower Li concentrations in which region the high voltage plateau appears in first cycle charging. Mechanism of oxygen vacancy formation is then investigated in Chapter 6. The trend of oxygen vacancy formation energies versus Li concentration suggests that oxygen vacancies could be generated at room temperature at lower Li concentrations (Li concentration $< 5/7$). The polyhedral sites with oxygen vacancies become highly unstable and the Ni^{2+} ions occupying these sites might be extruded to the adjacent polyhedral sites where no oxygen vacancies exist. This oxygen vacancy assisted Ni migration mechanism therefore successfully explained the migration of surface transition metal ions and related phase/structural change nears the material surface.

In conclusion, finds in this research prove that first principles computational method can play a guiding role in material designing and optimization. As the problems

appear nowadays are much complicated, sophisticated experimental tools are required and the theoretical/simulation guidance is usually needed. First principles computational method can provide straight and reliable solutions to problems ambiguous for conventional experimental methods, therefore will indeed lead the experimental research towards the right direction in a highly efficient way.

7.2 Future work

7.2.1 Computational designing of Li-rich doped spinel $\text{Li}_2\text{M}_2\text{O}_4$

Although the theoretical capacity of spinel materials is two Li per formula, the conventional spinel materials can only contribute one Li per formula due to the strong collective Jahn-Teller distortion at high Li concentration (more than one Li per formula). Since the collective Jahn-Teller distortions are caused by the large amount of Mn^{3+} ions in Li-rich spinel materials, doping proper types and amount of metal ions may solve the problem. Findings in the first part of this research have demonstrated that first principles computations can effectively pre-screening candidate dopants. A systematic computational study of the series of $\text{Li}_2\text{M}_2\text{O}_4$ with M being various combinations of metals ions therefore will be very helpful in designing new types of doped spinel cathode with high capacities.

7.2.2 Surface coating of Li-excess layered compound $\text{Li}[\text{Ni}_x\text{Li}_{1/3-2x/3}\text{Mn}_{2/3-x/3}]\text{O}_2$

Findings in the second part of this research have provided convincing evidences that a layer to spinel phase transformation can happened in the Li-excess layered compounds $\text{Li}[\text{Ni}_x\text{Li}_{1/3-2x/3}\text{Mn}_{2/3-x/3}]\text{O}_2$ with assistance of oxygen vacancies. For transition metal ions exposed on the particle surface, these “oxygen vacancies” are naturally

generated and cause the specific material structural change near the surface. This structural change could cause transition metal ions stacked in the Li sites blocking Li diffusion channel and impede Li diffusion, therefore reduce the rate performance of this materials. Coating the material surfaces with highly conductive and thermally stable materials could help to prevent this surface structural change. Computational method will be helpful to simulate properties such as lattice parameters, thermal stabilities, as well as electronic and ionic conductivities, therefore could pre-select candidate coating materials in an efficient way.

REFERENCE

1. K. Mizushima, P.C. Jones, P.J. Wiseman, and J.B. Goodenough, *Lixcoo₂ "(Oless-Thanxless-Than-or-Equal-To1) - a New Cathode Material for Batteries of High-Energy Density*. Materials Research Bulletin, 1980. **15**(6): p. 783-789.
2. T. Ohzuku, A. Ueda, M. Nagayama, Y. Iwakoshi, and H. Komori, *COMPARATIVE-STUDY OF LICOO₂, LINI_{1/2}CO_{1/2}O₂ AND LINIO₂ FOR 4-VOLT SECONDARY LITHIUM CELLS*. Electrochimica Acta, 1993. **38**(9): p. 1159-1167.
3. J.M. Tarascon and D. Guyomard, *THE LI₁+XMN₂O₄/C ROCKING-CHAIR SYSTEM - A REVIEW*. Electrochimica Acta, 1993. **38**(9): p. 1221-1231.
4. Y.Y. Xia and M. Yoshio, *An investigation of lithium ion insertion into spinel structure Li-Mn-O compounds*. Journal of The Electrochemical Society, 1996. **143**(3): p. 825-833.
5. G. Ceder, Y.M. Chiang, D.R. Sadoway, M.K. Aydinol, Y.I. Jang, and B. Huang, *Identification of cathode materials for lithium batteries guided by first-principles calculations*. Nature, 1998. **392**(6677): p. 694-696.
6. J.M. Tarascon and M. Armand, *Issues and challenges facing rechargeable lithium batteries*. Nature, 2001. **414**(6861): p. 359-367.
7. F. Croce, A.D. Epifanio, J. Hassoun, A. Deptula, T. Olczac, and B. Scrosati, *A novel concept for the synthesis of an improved LiFePO₄ lithium battery cathode*. Electrochemical and Solid State Letters, 2002. **5**(3): p. A47-A50.
8. M.S. Whittingham, *Lithium batteries and cathode materials*. Chemical Reviews, 2004. **104**(10): p. 4271-4301.
9. Z. Lu, D.D. MacNeil, and J.R. Dahn, *Layered Cathode Materials Li[NixLi^{1/3-2x/3}Mn^{2/3-x/3}]O₂ for Lithium-Ion Batteries*. Electrochemical and Solid-State Letters, 2001. **4**(11): p. A191-A194.
10. C.R. Fell, K.J. Carroll, M. Chi, and Y.S. Meng, *Synthesis--Structure--Property Relations in Layered, "Li-excess" Oxides Electrode Materials Li[Li_{sub 1/3} -*

- $2x/3\text{Ni}_{x/3}\text{Mn}_{2/3-x/3}\text{O}_2$ ($x = 1/3, 1/4, \text{ and } 1/5$). Journal of The Electrochemical Society. **157**(11): p. A1202-A1211.
11. M.M. Thackeray, W.I.F. David, P.G. Bruce, and J.B. Goodenough, *LITHIUM INSERTION INTO MANGANESE SPINELS*. Materials Research Bulletin, 1983. **18**(4): p. 461-472.
 12. J.B. Goodenough, M.M. Thackeray, W.I.F. David, and P.G. Bruce, *Lithium Insertion Extraction Reactions with Manganese Oxides*. Revue de Chimie Minerale, 1984. **21**(4): p. 435-455.
 13. W.I.F. David, M.M. Thackeray, P.G. Bruce, and J.B. Goodenough, *Lithium Insertion into Beta-MnO₂ and the Rutile-Spinel Transformation*. Materials Research Bulletin, 1984. **19**(1): p. 99-106.
 14. R.J. Gummow, A. Dekock, and M.M. Thackeray, *IMPROVED CAPACITY RETENTION IN RECHARGEABLE 4V LITHIUM LITHIUM MANGANESE OXIDE (SPINEL) CELLS*. Solid State Ionics, 1994. **69**(1): p. 59-67.
 15. K.-S. Lee, S.-T. Myung, H.J. Bang, S. Chung, and Y.-K. Sun, *Co-precipitation synthesis of spherical Li_{1.05}M_{0.05}Mn_{1.90}O₄ (M = Ni, Mg, Al) spinel and its application for lithium secondary battery cathode*. Electrochimica Acta, 2007. **52**(16): p. 5201-5206.
 16. Y.J. Lee, S.H. Park, C. Eng, J.B. Parise, and C.P. Grey, *Cation ordering and electrochemical properties of the cathode materials LiZn_xMn_{2-0.5x}O₄, 0 < x ≤ 0.5: A Li-6 magic-angle spinning NMR spectroscopy and diffraction study*. Chemistry of Materials, 2002. **14**(1): p. 194-205.
 17. L. Hernan, J. Morales, L. Sanchez, and J. Santos, *Use of Li-M-Mn-O [M = Co, Cr, Ti] spinels prepared by a sol-gel method as cathodes in high-voltage lithium batteries*. Solid State Ionics, 1999. **118**(3-4): p. 179-185.
 18. J.H. Kim, S.T. Myung, C.S. Yoon, S.G. Kang, and Y.K. Sun, *Comparative study of LiNi_{0.5}Mn_{1.5}O_{4-δ} and LiNi_{0.5}Mn_{1.5}O₄ cathodes having two crystallographic structures: Fd(3)over-bar and P4(3)32*. Chemistry of Materials, 2004. **16**(5): p. 906-914.

19. G.H. Li, H. Ikuta, T. Uchida, and M. Wakihara, *The spinel phases $\text{LiM}(y)\text{Mn}(2-y)\text{O}(4)$ ($M=\text{Co},\text{Cr},\text{Ni}$) as the cathode for rechargeable lithium batteries*. Journal of The Electrochemical Society, 1996. **143**(1): p. 178-182.
20. J. Molenda, J. Marzec, K. Swierczek, W. Ojczyk, M. Ziemnicki, M. Molenda, M. Drozdek, and R. Dziembaj, *The effect of 3d substitutions in the manganese sublattice on the charge transport mechanism and electrochemical properties of manganese spinel*. Solid State Ionics, 2004. **171**(3-4): p. 215-227.
21. T. Ohzuku, S. Takeda, and M. Iwanaga, *Solid-state redox potentials for $\text{Li}[\text{Me}_{1/2}\text{Mn}_{3/2}]\text{O}_4$ (Me : 3d-transition metal) having spinel-framework structures: a series of 5 volt materials for advanced lithium-ion batteries*. Journal of Power Sources, 1999. **81-82**: p. 90-94.
22. R. Singhal, S.R. Das, M.S. Tomar, O. Ovideo, S. Nieto, R.E. Melgarejo, and R.S. Katiyar, *Synthesis and characterization of Nd doped LiMn_2O_4 cathode for Li-ion rechargeable batteries*. Journal of Power Sources, 2007. **164**(2): p. 857-861.
23. J. Tu, X.B. Zhao, D.G. Zhuang, G.S. Cao, T.J. Zhu, and J.P. Tu, *Studies of cycleability of LiMn_2O_4 and $\text{LiLa}_{0.01}\text{Mn}_{1.99}\text{O}_4$ as cathode materials for Li-ion battery*. Physica B-Condensed Matter, 2006. **382**(1-2): p. 129-134.
24. S.T. Yang, J.H. Jia, L. Ding, and M.C. Zhang, *Studies of structure and cycleability of LiMn_2O_4 and $\text{LiNd}_{0.01}\text{Mn}_{1.99}\text{O}_4$ as cathode for Li-ion batteries*. Electrochimica Acta, 2003. **48**(5): p. 569-573.
25. G. Ceder, M.K. Aydinol, and A.F. Kohan, *Application of first-principles calculations to the design of rechargeable Li-batteries*. Computational Materials Science, 1997. **8**(1-2): p. 161-169.
26. K. Kang and G. Ceder, *Factors that affect Li mobility in layered lithium transition metal oxides*. Physical Review B, 2006. **74**(9): p. -.
27. G. Ceder, A. Van der Ven, C. Marianetti, and D. Morgan, *First-principles alloy theory in oxides*. Modelling and Simulation in Materials Science and Engineering, 2000. **8**(3): p. 311-321.

28. A. Van der Ven, C. Marianetti, D. Morgan, and G. Ceder, *Phase transformations and volume changes in spinel $\text{Li}_x\text{Mn}_2\text{O}_4$* . *Solid State Ionics*, 2000. **135**(1-4): p. 21-32.
29. A. Van der Ven, G. Ceder, M. Asta, and P.D. Tepesch, *First-principles theory of ionic diffusion with nondilute carriers*. *Physical Review B*, 2001. **6418**(18): p. -.
30. A.R. Armstrong, M. Holzapfel, P. Novak, C.S. Johnson, S.H. Kang, M.M. Thackeray, and P.G. Bruce, *Demonstrating oxygen loss and associated structural reorganization in the lithium battery cathode $\text{Li}[\text{Ni}_{0.2}\text{Li}_{0.2}\text{Mn}_{0.6}]\text{O}_2$* . *Journal of the American Chemical Society*, 2006. **128**(26): p. 8694-8698.
31. M. Jiang, B. Key, Y.S. Meng, and C.P. Grey, *Electrochemical and Structural Study of the Layered, "Li-Excess" Lithium-Ion Battery Electrode Material $\text{Li}[\text{Li}_{1/9}\text{Ni}_{1/3}\text{Mn}_{5/9}]\text{O}_2$* . *Chemistry of Materials*, 2009. **21**(13): p. 2733-2745.
32. Z.H. Lu and J.R. Dahn, *Understanding the anomalous capacity of $\text{Li}/\text{Li}[\text{Ni}_x\text{Li}_{(1/3-2x/3)}\text{Mn}_{(2/3-x/3)}]\text{O}_2$ cells using in situ X-ray diffraction and electrochemical studies*. *Journal of The Electrochemical Society*, 2002. **149**(7): p. A815-A822.
33. Y. Wu and A. Manthiram, *Effect of surface modifications on the layered solid solution cathodes $(1-z)\text{Li}[\text{Li}_{1/3}\text{Mn}_{2/3}]\text{O}_2 - (z)\text{Li}[\text{Mn}_{0.5-y}\text{Ni}_{0.5-y}\text{Co}_2]\text{O}_2$* . *Solid State Ionics*, 2009. **180**(1): p. 50-56.
34. J.M. Zheng, Z.R. Zhang, X.B. Wu, Z.X. Dong, Z. Zhu, and Y. Yang, *The effects of AlF_3 coating on the performance of $\text{Li}[\text{Li}_{0.2}\text{Mn}_{0.54}\text{Ni}_{0.13}\text{Co}_{0.13}]\text{O}_2$ positive electrode material for lithium-ion battery*. *Journal of The Electrochemical Society*, 2008. **155**(10): p. A775-A782.
35. K. Kang and Massachusetts Institute of Technology. Dept. of Materials Science and Engineering., *Designing new electrode materials for energy devices by integrating ab initio computations with experiments*, 2006. p. 161 p.
36. A. Van der Ven and Massachusetts Institute of Technology. Dept. of Materials Science and Engineering., *First principles investigation of the thermodynamic and kinetic properties of lithium transition metal oxides*, 2000. p. 164 p.

37. M.C. Payne, M.P. Teter, D.C. Allan, T.A. Arias, and J.D. Joannopoulos, *Iterative minimization techniques for ab initio total-energy calculations: molecular dynamics and conjugate gradients*. Reviews of Modern Physics, 1992. **64**(4): p. 1045.
38. F. Zhou, M. Cococcioni, C.A. Marianetti, D. Morgan, and G. Ceder, *First-principles prediction of redox potentials in transition-metal compounds with LDA + U*. Physical Review B, 2004. **70**(23).
39. R.J. Gummow, A. Dekock, and M.M. Thackeray, *Improved capacity retention in rechargeable 4V lithium/lithium manganese oxide (spinel) cells*. Solid State Ionics, 1994. **69**(1): p. 59-67.
40. A. Eftekhari, *Aluminum oxide as a multi-function agent for improving battery performance of LiMn₂O₄ cathode*. Solid State Ionics, 2004. **167**(3-4): p. 237-242.
41. Y.J. Shin and A. Manthiram, *Factors influencing the capacity fade of spinel lithium manganese oxides*. Journal of The Electrochemical Society, 2004. **151**(2): p. A204-A208.
42. Z.H. Chen, W.Q. Lu, J. Liu, and K. Amine, *LiPF₆/LiBOB blend salt electrolyte for high-power lithium-ion batteries*. Electrochimica Acta, 2006. **51**(16): p. 3322-3326.
43. H. Berg and J.O. Thomas, *Neutron diffraction study of electrochemically delithiated LiMn₂O₄ spinel*. Solid State Ionics, 1999. **126**(3-4): p. 227-234.
44. K. Kanamura, H. Naito, T. Yao, and Z. Takehara, *Structural change of the LiMn₂O₄ spinel structure induced by extraction of lithium*. Journal of Materials Chemistry, 1996. **6**(1): p. 33-36.
45. H. Abiko, M. Hibino, and T. Kudo, *Temperature dependence of the potential-composition profiles of Li_xMn₂O₄ spinel*. Electrochemical and Solid State Letters, 1998. **1**(3): p. 114-116.
46. J.S. Kim, J. Prakash, and J.R. Selman, *Thermal characteristics of Li_xMn₂O₄ spinel*. Electrochemical and Solid State Letters, 2001. **4**(9): p. A141-A144.
47. D. Aurbach, M.D. Levi, K. Gamulski, B. Markovsky, G. Salitra, E. Levi, U. Heider, L. Heider, and R. Oesten, *Capacity fading of Li(x)Mn(2)O(4) spinel electrodes*

- studied by XRD and electroanalytical techniques*. Journal of Power Sources, 1999. **81**: p. 472-479.
48. Y.Y. Xia, Y.H. Zhou, and M. Yoshio, *Capacity fading on cycling of 4 V Li/LiMn₂O₄ cells*. Journal of The Electrochemical Society, 1997. **144**(8): p. 2593-2600.
49. A. Yamada and M. Tanaka, *Jahn-Teller structural phase transition around 280K in LiMn₂O₄*. Materials Research Bulletin, 1995. **30**(6): p. 715-721.
50. H. Yamaguchi, A. Yamada, and H. Uwe, *Jahn-Teller transition of LiMn₂O₄ studied by x-ray-absorption spectroscopy*. Physical Review B, 1998. **58**(1): p. 8-11.
51. V. Massarotti, D. Capsoni, M. Bini, P. Scardi, M. Leoni, V. Baron, and H. Berg, *LiMn₂O₄ low-temperature phase: synchrotron and neutron diffraction study*. Journal of Applied Crystallography, 1999. **32**: p. 1186-1189.
52. A.S. Wills, N.P. Raju, and J.E. Greedan, *Low-temperature structure and magnetic properties of the spinel LiMn₂O₄: A frustrated antiferromagnet and cathode material*. Chemistry of Materials, 1999. **11**(6): p. 1510-1518.
53. I. Tomeno, Y. Kasuya, and Y. Tsunoda, *Charge and spin ordering in LiMn₂O₄*. Physical Review B, 2001. **64**(9): p. 8.
54. J. Gaddy, J. Lamsal, M. Petrovic, W. Montfrooij, A. Schmetts, and T. Vojta, *Magnetic ordering in the spinel compound Li Mn_(2-x)Li_x O₍₄₎(x=0,0.04)*. Journal of Applied Physics, 2009. **105**(7).
55. R. Darling and J. Newman, *Dynamic Monte Carlo simulations of diffusion in Li_yMn₂O₄*. Journal of The Electrochemical Society, 1999. **146**(10): p. 3765-3772.
56. I.Y. Gotlib, I.V. Murin, and E.M. Piotrovskaya, *Molecular dynamics simulations of Li_xMn₂O₄ spinel solid solutions with simple potential models*. Inorganic Materials, 2003. **39**(4): p. 404-408.
57. C.Y. Ouyang, S.Q. Shi, Z.X. Wang, X.J. Huang, and L.Q. Chen, *Experimental and theoretical studies on dynamic properties of Li ions in Li_xMn₂O₄*. Solid State Communications, 2004. **130**(7): p. 501-506.

58. S.K. Mishra and G. Ceder, *Structural stability of lithium manganese oxides*. Physical Review B, 1999. **59**(9): p. 6120-6130.
59. V. Massarotti, D. Capsoni, M. Bini, G. Chiodelli, C.B. Azzoni, M.C. Mozzati, and A. Paleari, *Electric and magnetic properties of LiMn₂O₄- and Li₂MnO₃-type oxides*. Journal of Solid State Chemistry, 1997. **131**(1): p. 94-100.
60. H. Xia, Y.S. Meng, L. Lu, and G. Ceder, *Electrochemical properties of nonstoichiometric LiNi_{0.5}Mn_{1.5}O₄-delta thin-film electrodes prepared by pulsed laser deposition*. Journal of The Electrochemical Society, 2007. **154**(8): p. A737-A743.
61. K.M. Shaju and P.G. Bruce, *Nano-LiNi_{0.5}Mn_{1.5}O₄ spinel: a high power electrode for Li-ion batteries*. Dalton Transactions, 2008(40): p. 5471-5475.
62. M. Kunduraci, J.F. Al-Sharab, and G.G. Amatucci, *High-power nanostructured LiMn_{2-x}Ni_xO₄ high-voltage lithium-ion battery electrode materials: Electrochemical impact of electronic conductivity and morphology*. Chemistry of Materials, 2006. **18**(15): p. 3585-3592.
63. C.Y. Ouyang, S.Q. Shi, and M.S. Lei, *Jahn-Teller distortion and electronic structure of LiMn₂O₄*. Journal of Alloys and Compounds, 2009. **474**(1-2): p. 370-374.
64. G. Kresse and D. Joubert, *From ultrasoft pseudopotentials to the projector augmented-wave method*. Physical Review B, 1999. **59**(3): p. 1758-1775.
65. G. Kresse and J. Hafner, *Ab-Initio molecular-dynamics simulation of the liquid-metal amorphous-semiconductor transition in germanium*. Physical Review B, 1994. **49**(20): p. 14251-14269.
66. G. Kresse and J. Furthmuller, *Efficiency of ab-initio total energy calculations for metals and semiconductors using a plane-wave basis set*. Computational Materials Science, 1996. **6**(1): p. 15-50.
67. G. Kresse and J. Furthmuller, *Efficient iterative schemes for ab initio total-energy calculations using a plane-wave basis set*. Physical Review B, 1996. **54**(16): p. 11169-11186.

68. J.P. Perdew, K. Burke, and Y. Wang, *Generalized gradient approximation for the exchange-correlation hole of a many-electron system*. Physical Review B, 1996. **54**(23): p. 16533-16539.
69. M. Cococcioni and S. de Gironcoli, *Linear response approach to the calculation of the effective interaction parameters in the LDA+U method*. Physical Review B, 2005. **71**(3): p. 16.
70. A.I. Liechtenstein, V.I. Anisimov, and J. Zaanen, *Density-Functional Theory and Strong-Interactions-Orbital ordering in Mott-Hubbard insulators*. Physical Review B, 1995. **52**(8): p. R5467-R5470.
71. T. Ohzuku, M. Kitagawa, and T. Hirai, *Electrochemistry of Manganese-Dioxide in Lithium Nonaqueous Cell .3. X-Ray Diffractational Study on the Reduction of Spinel-Related Manganese-Dioxide*. Journal of The Electrochemical Society, 1990. **137**(3): p. 769-775.
72. J.M. Tarascon, E. Wang, F.K. Shokoohi, W.R. Mckinnon, and S. Colson, *The Spinel Phase of LiMn2O4 as a Cathode in Secondary Lithium Cells*. Journal of The Electrochemical Society, 1991. **138**(10): p. 2859-2864.
73. W. Liu, K. Kowal, and G.C. Farrington, *Mechanism of the electrochemical insertion of lithium into LiMn2O4 spinels*. Journal of The Electrochemical Society, 1998. **145**(2): p. 459-465.
74. B.N. Figgis and M.A. Hitchman, *Ligand field theory and its applications* 2000, New York: Wiley-VCH. xviii, 354 p.
75. H.A. Jahn and E. Teller, *Stability of polyatomic molecules in degenerate electronic states. I. Orbital degeneracy*. Proceedings of the Royal Society of London Series a-Mathematical and Physical Sciences, 1937. **161**(A905): p. 220-235.
76. H. Hayakawa, T. Takada, H. Enoki, and E. Akiba, *New findings on the structural phase transitions of spinel LiMn2O4 at low temperature*. Journal of Materials Science Letters, 1998. **17**(10): p. 811-812.

77. Z.X. Wang, H. Ikuta, Y. Uchimoto, and M. Wakihara, *Preparation and electrochemical properties of stoichiometric and nonstoichiometric $\text{LiCo}_x\text{Mn}_{2-x}\text{O}_4$* . Journal of The Electrochemical Society, 2003. **150**(9): p. A1250-A1254.
78. J. Molenda, J. Marzec, K. Swierczek, D. Palubiak, W. Ojczyk, and M. Ziemnicki, *The effect of 3d substitutions in the manganese sublattice on the electrical and electrochemical properties of manganese spinel*. Solid State Ionics, 2004. **175**(1-4): p. 297-304.
79. K. Kang, Y.S. Meng, J. Breger, C.P. Grey, and G. Ceder, *Electrodes with High Power and High Capacity for Rechargeable Lithium Batteries*. Science, 2006. **311**(5763): p. 977-980.
80. B. Xu and S. Meng, *Factors affecting Li mobility in spinel LiMn_2O_4 - A first-principles study by GGA and GGA+U methods*. J. Power Sources, 2010. **195**(15): p. 4971-4976.
81. C.P. Grey, W.S. Yoon, J. Reed, and G. Ceder, *Electrochemical activity of Li in the transition-metal sites of $\text{O}_3\text{Li}[\text{Li}(1-2x)/3\text{Mn}(2-x)/3\text{Ni}]_x\text{O}_2$* . Electrochemical and Solid State Letters, 2004. **7**(9): p. A290-A293.
82. M.M. Thackeray, S.-H. Kang, C.S. Johnson, J.T. Vaughey, R. Benedek, and S.A. Hackney, *Li_2MnO_3 -stabilized LiMO_2 ($M = \text{Mn}, \text{Ni}, \text{Co}$) electrodes for lithium-ion batteries*. Journal of Materials Chemistry, 2007. **17**(30): p. 3112-3125.
83. Y.S. Meng, G. Ceder, C.P. Grey, W.S. Yoon, M. Jiang, J. Breger, and Y. Shao-Horn, *Cation ordering in layered $\text{O}_3 \text{Li}[\text{Ni}_x\text{Li}_{1/3-2x/3}\text{Mn}_{2/3-x/3}]_x\text{O}_2$ ($0 \leq x \leq 1/2$) compounds*. Chem. Mater., 2005. **17**(9): p. 2386-2394.
84. M. Jiang, B. Key, Y.S. Meng, and C.P. Grey, *Electrochemical and Structural Study of the Layered, "Li-Excess" Lithium-Ion Battery Electrode Material $\text{Li}[\text{Li}_{1/9}\text{Ni}_{1/3}\text{Mn}_{5/9}]_x\text{O}_2$* . Chemistry of Materials, 2009. **21**(13): p. 2733-2745.
85. C.H. Lei, J. Baren, J.G. Wen, I. Petrov, S.H. Kang, and D.P. Abraham, *Local structure and composition studies of $\text{Li}_{1.2}\text{Ni}_{0.2}\text{Mn}_{0.6}\text{O}_2$ by analytical electron microscopy*. Journal of Power Sources, 2008. **178**(1): p. 422-433.

86. A.R. Armstrong, M. Holzapfel, P. Novak, C.S. Johnson, S.H. Kang, M.M. Thackeray, and P.G. Bruce, *Demonstrating Oxygen Loss and Associated Structural Reorganization in the Lithium Battery Cathode $\text{Li}[\text{Ni}_{0.2}\text{Li}_{0.2}\text{Mn}_{0.6}]\text{O}_2$* . J. Am. Chem. Soc., 2006. **128**(26): p. 8694-8698.
87. Z. Lu and J.R. Dahn, *Understanding the Anomalous Capacity of $\text{Li}/\text{Li}[\text{Ni}_x\text{Li}_{(1/3 - 2x/3)}\text{Mn}_{(2/3 - x/3)}]\text{O}_2$ Cells Using In Situ X-Ray Diffraction and Electrochemical Studies*. Journal of The Electrochemical Society, 2002. **149**(7): p. A815-A822.
88. A.D. Robertson and P.G. Bruce, *Overcapacity of $\text{Li}[\text{Ni}(x)\text{Li}_{(1/3 - 2x/3)}\text{Mn}_{(2/3 - x/3)}]\text{O}_2$ Electrodes*. Electrochemical and Solid-State Letters, 2004. **7**(9): p. A294-A298.
89. C.R. Fell, K.J. Carroll, M. Chi, and Y.S. Meng, *Synthesis--Structure--Property Relations in Layered, "Li-excess" Oxide Electrode Materials $\text{Li}[\text{Li}_{1/3 - 2x/3}\text{Ni}_x\text{Mn}_{2/3 - x/3}]\text{O}_2$ ($x = 1/3, 1/4, \text{ and } 1/5$)*. Journal of The Electrochemical Society, 2010. **157**(11): p. A1202-A1211.
90. S.H. Kang and M.M. Thackeray, *Enhancing the rate capability of high capacity $x\text{Li}_2\text{MnO}_3 \cdot (1-x)\text{LiMO}_2$ ($M = \text{Mn, Ni, Co}$) electrodes by Li-Ni-PO₄ treatment*. Electrochemistry Communications, 2009. **11**(4): p. 748-751.
91. J. Rodríguez-Carvajal. *FullProf: A Program for Rietveld Refinement and Pattern Matching Analysis*. in *Satellite Meeting on Powder Diffraction of the XV Congress of the IUCr*. 1990. Toulouse, France.
92. B. Toby, *EXPGUI, a graphical user interface for GSAS*. Journal of Applied Crystallography, 2001. **34**(2): p. 210-213.
93. A.C. Larson and R.B.V. Dreele, *General Structure Analysis System (GSAS)*. Los Alamos National Laboratory Report LAUR, 2000. **86**(748).
94. Y. Hinuma, Y.S. Meng, K.S. Kang, and G. Ceder, *Phase transitions in the $\text{LiNi}_{0.5}\text{Mn}_{0.5}\text{O}_2$ system with temperature*. Chemistry of Materials, 2007. **19**(7): p. 1790-1800.

95. M.D. Levi, G. Salitra, B. Markovsky, H. Teller, D. Aurbach, U. Heider, and L. Heider, *Solid-state electrochemical kinetics of Li-ion intercalation into $\text{Li}_{1-x}\text{CoO}_2$: Simultaneous application of electroanalytical techniques SSCV, PITT, and EIS*. Journal of The Electrochemical Society, 1999. **146**(4): p. 1279-1289.
96. D. Aurbach, M.D. Levi, E. Levi, H. Teller, B. Markovsky, G. Salitra, U. Heider, and L. Heider, *Common Electroanalytical Behavior of Li Intercalation Processes into Graphite and Transition Metal Oxides*. Journal of The Electrochemical Society, 1998. **145**(9): p. 3024-3034.
97. S.J. Pennycook, *Z-contrast stem for materials science*. Ultramicroscopy, 1989. **30**(1-2): p. 58-69.
98. E.M. James and N.D. Browning, *Practical aspects of atomic resolution imaging and analysis in STEM*. Ultramicroscopy, 1999. **78**(1-4): p. 125-139.
99. R.F. Egerton, *Electron Energy-Loss Spectroscopy in the Electron Microscope*. 2 ed 1996, New York: Plenum Press.
100. Z.L. Wang, J.S. Yin, and Y.D. Jiang, *EELS analysis of cation valence states and oxygen vacancies in magnetic oxides*. Micron, 2000. **31**(5): p. 571-580.
101. W.S. Yoon, Y. Paik, X.Q. Yang, M. Balasubramanian, J. McBreen, and C.P. Grey, *Investigation of the local structure of the $\text{LiNi}_{0.5}\text{Mn}_{0.5}\text{O}_2$ cathode material during electrochemical cycling by X-ray absorption and NMR spectroscopy*. Electrochemical and Solid State Letters, 2002. **5**(11): p. A263-A266.
102. Z. Lu, L.Y. Beaulieu, R.A. Donaberger, C.L. Thomas, and J.R. Dahn, *Synthesis, Structure, and Electrochemical Behavior of $\text{Li}[\text{Ni}(x)\text{Li}(1/3 - 2x/3)\text{Mn}(2/3 - x/3)]\text{O}_2$* . Journal of The Electrochemical Society, 2002. **149**(6): p. A778-A791.